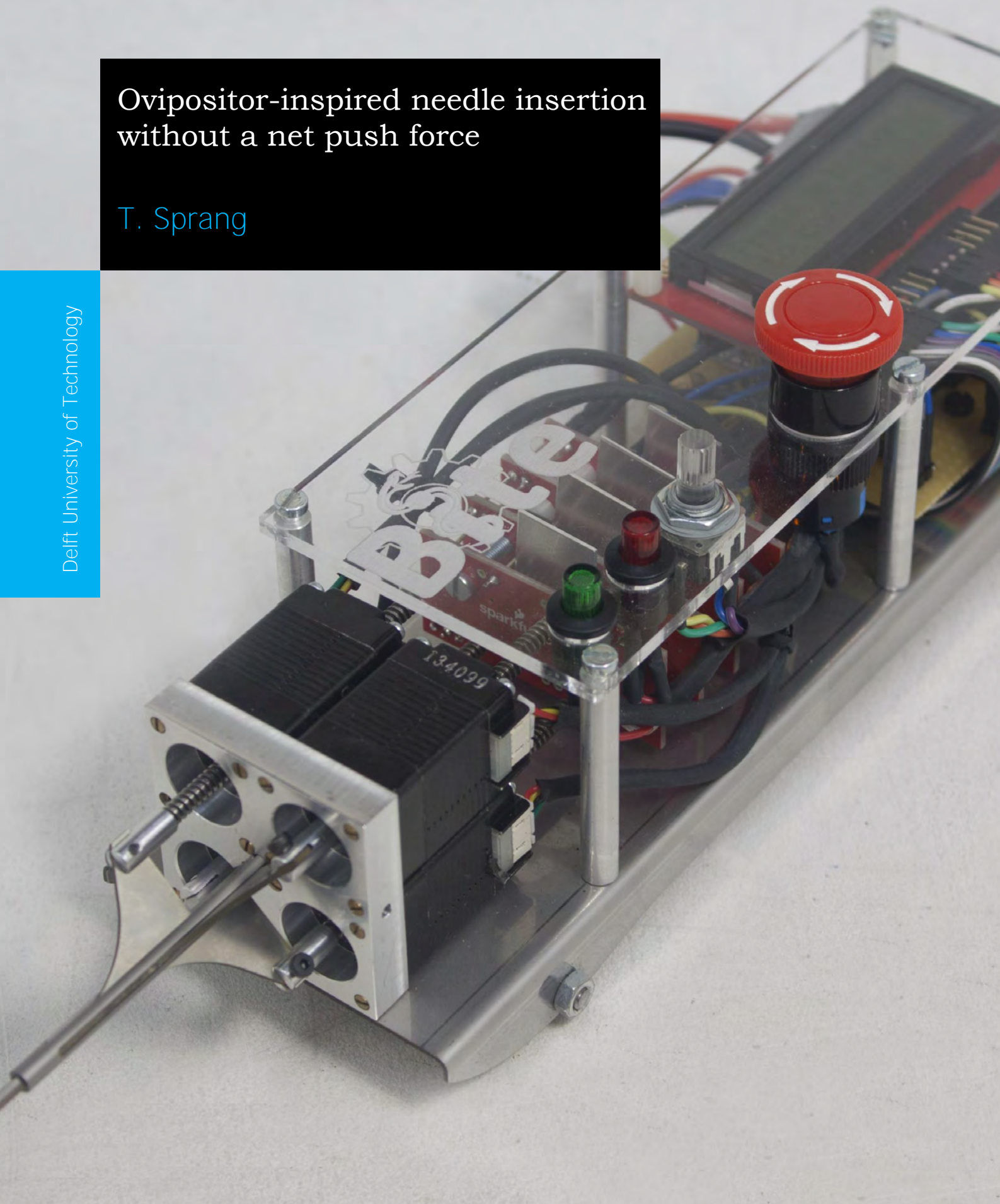


Ovipositor-inspired needle insertion without a net push force

T. Sprang

Delft University of Technology



Ovipositor-inspired needle insertion without a net push force

By

T. Sprang

in partial fulfilment of the requirements for the degree of

Master of Science

in Mechanical Engineering

at the Delft University of Technology,
to be defended publicly on Wednesday December 17, 2014 at 14:30.

Supervisors:

Dr. D. Dodou

Prof. dr. ir. P. Breedveld

Thesis committee:

Prof. dr. ir. P. Breedveld

Dr. D. Dodou

Dr. ir. J.F.L. Goosen

Dr. ir. S. Misra

TU Delft

TU Delft

TU Delft

U Twente

An electronic version of this thesis is available at <http://repository.tudelft.nl/>.



CONTENTS

| | |
|---|-----------|
| I Introduction | 2 |
| I-A Commonly used medical needles | 2 |
| I-B Steerable medical needles: state-of-the-art | 2 |
| I-C The wasp ovipositor | 4 |
| I-D Research question and goal | 5 |
| II Design of a multipart needle | 6 |
| II-A Requirements | 6 |
| II-B Design considerations | 6 |
| II-C Description of the prototype | 7 |
| III Hypotheses | 8 |
| IV Method | 10 |
| IV-A Experimental setup | 10 |
| IV-B Variables | 10 |
| IV-C Experimental procedure | 12 |
| IV-D Data analysis | 12 |
| IV-E Statistical analysis | 13 |
| V Results | 13 |
| V-A Prototype experiment | 13 |
| V-B Force experiment | 14 |
| VI Discussion | 14 |
| VI-A Gelatin concentration | 16 |
| VI-B Offset | 16 |
| VI-C Sequence | 17 |
| VI-D Velocity | 17 |
| VI-E Limitations | 17 |
| VI-F Future work | 18 |
| VII Conclusion | 19 |
| References | 19 |
| Appendix A: Actuator configuration concepts | 21 |
| Appendix B: Images of the experimental setup | 23 |
| B-A Prototype | 23 |
| B-B Prototype experiment | 25 |
| B-C Force experiment | 26 |
| Appendix C: Technical drawings | 27 |
| Appendix D: Prototype embedded software | 33 |
| D-A Software schematic | 33 |
| D-B Embedded code | 34 |
| Appendix E: Measurement details | 39 |
| E-A Prototype experiments | 39 |
| E-B Force measurements | 40 |
| Appendix F: m-files | 41 |
| F-A Prototype experiment | 41 |
| F-B Force experiment | 47 |
| Appendix G: Needle surface roughness | 51 |
| Appendix H: Force measurement calibration | 52 |

Ovipositor-inspired needle insertion without a net push force

Tim Sprang

Abstract—As current rigid needles follow straight line trajectories, limiting the path planning possibilities in minimally invasive surgical approaches, research into steerable needle instruments becomes necessary. This article outlines the development of a four-part needle prototype inspired by the ovipositor of parasitic wasps and designed to penetrate without a net push force. In the wasp ovipositor, three valves move reciprocally to gain depth in the substrate with one valve at a time, while the other two valves anchor against the substrate and provide lateral support. The needle prototype consists of four reciprocally moving needle parts, devoid of any tissue gripping textures, with a combined cross-section of 2 x 2 mm, supported by a platform which is able to move with low friction. The goal of this study is to penetrate tissue phantom material without applying a net push force by using a friction difference induced between protruding needle parts and stationary needle parts, solely based on the difference in the size of surface area subjected to needle-tissue friction. The prototypes validation in gelatin phantom shows needle insertion with limited push force, independent from the penetration depth. The performance of the prototype is measured by the amount of slip between needle and substrate. Slip shows to be proportional with needle-part offset and inversely proportional with gelatin concentration, whereas protrusion sequence and needle-part velocity seem to have little effect on performance. Validation of these relations is found challenging due to the effect of inertia and bearing friction on the measured slip.

Keywords—Needle steering, ovipositor, zero net push force, buckling.

I. INTRODUCTION

A. Commonly used medical needles

Blood sampling (e.g. fetal blood sampling; Furusho et al., 2006), biopsies (Bishoff et al., 1998), regional anesthesia (Zivanovic & Davies, 2000), neurosurgery (Grady et al. 1998, Rizun et al., 2004) and brachytherapy (Wan et al., 2004, McGill et al. 2011), all rely on percutaneous needle insertion (see also Abolhassani et al., 2007). The needles used in these procedures are rigid and follow straight trajectories, limiting the path planning possibilities for a surgeon. Accessibility of targets that are located deep inside the body is restricted, and deviation from the desired needle path due to, for example, obstructing anatomy, organ deformation and tissue inhomogeneity, is common (Misra et al., 2009). These functional limitations inhibit effective medical treatment when designated areas cannot be reached (Misra et al., 2009) and compromise safety during the insertion process when undesired areas are accidentally penetrated. (Frasson et al., 2009).

Needle deviation and accessibility issues in minimally invasive procedures can possibly be overcome by using steerable needles. Many research groups have been studying and developing steerable needles to help surgeons overcome the path planning limitations encountered with conventional straight needles. (e.g. Ebrahimi et al., 2003; Webster et al., 2005, 2006, 2009; Engh et al., 2006; Misra et al., 2009; Walsh et al., 2010; Frasson et al., 2010, 2011).

B. Steerable medical needles: state-of-the-art

Based on the type of forces required to control the curvature of the needle trajectory, steerable needles can be divided into two categories: internally steered needles relying on concentric axial insertion of multiple pre-bend needles, and externally steered needles that rely on reaction forces from the environment for control of curvature. Internally steered needles can be further subdivided into three types. In the first type, curvature is controlled by choosing needles pre-bend with the curve radii desired for each part of the trajectory and by axially protruding these through each other (Figure 1a; Webster et al., 2006). In the second type of internally steered needles, curvature depends on the net bending radius of two concentric pre-bend needles. By controlling the relative rotation angle between the concentric needles, their bending radius can be variably adjusted (Figure 1b; Sears & Dupont, 2006). Okazawa et al. (2005) and Walsh et al. (2010; also Loser, 2002 as reported by Ebrahimi et al., 2003) present a third method of internal steering according to which only the tip of the needle is curved and is axially protruded through a stiffer cannula which follows the trajectory of the tip. The curvature along the trajectory is controlled by the relative protrusion of the cannula with respect to the pre-bend needle (Figure 1c).

Next to the internally steered needles, two types of externally steered needles can be distinguished. The first type of externally steered needles relies on the translation and rotation of the needle base outside the tissue to bend the needle supported by the tissue at the tip. Reaction forces from the tissue close to the surface supports this applied bending moment, allowing for control of curvature (Figure 1d; Glozman, 2007). For this method of needle steering, high tissue reaction forces close to the surface are required, especially when the needle reaches greater depths (Cowan et al., 2011). The second type of externally steered needles relies on asymmetric forces acting from the environment on the beveled tip of a needle which can either have a constant or variable bevel angle. In the case of a needle tip with a constant bevel angle, curvature of the trajectory is controlled by applying a spin-and-stop duty cycle (Figure 1e; Webster et al., 2005; Eng et al., 2006; Misra et al.,

Tim Sprang is with the Department of Mechanical Engineering, Delft University of Technology, The Netherlands, Mekelweg 2, 2628 CD Delft, e-mail: Sprang.T@gmail.com

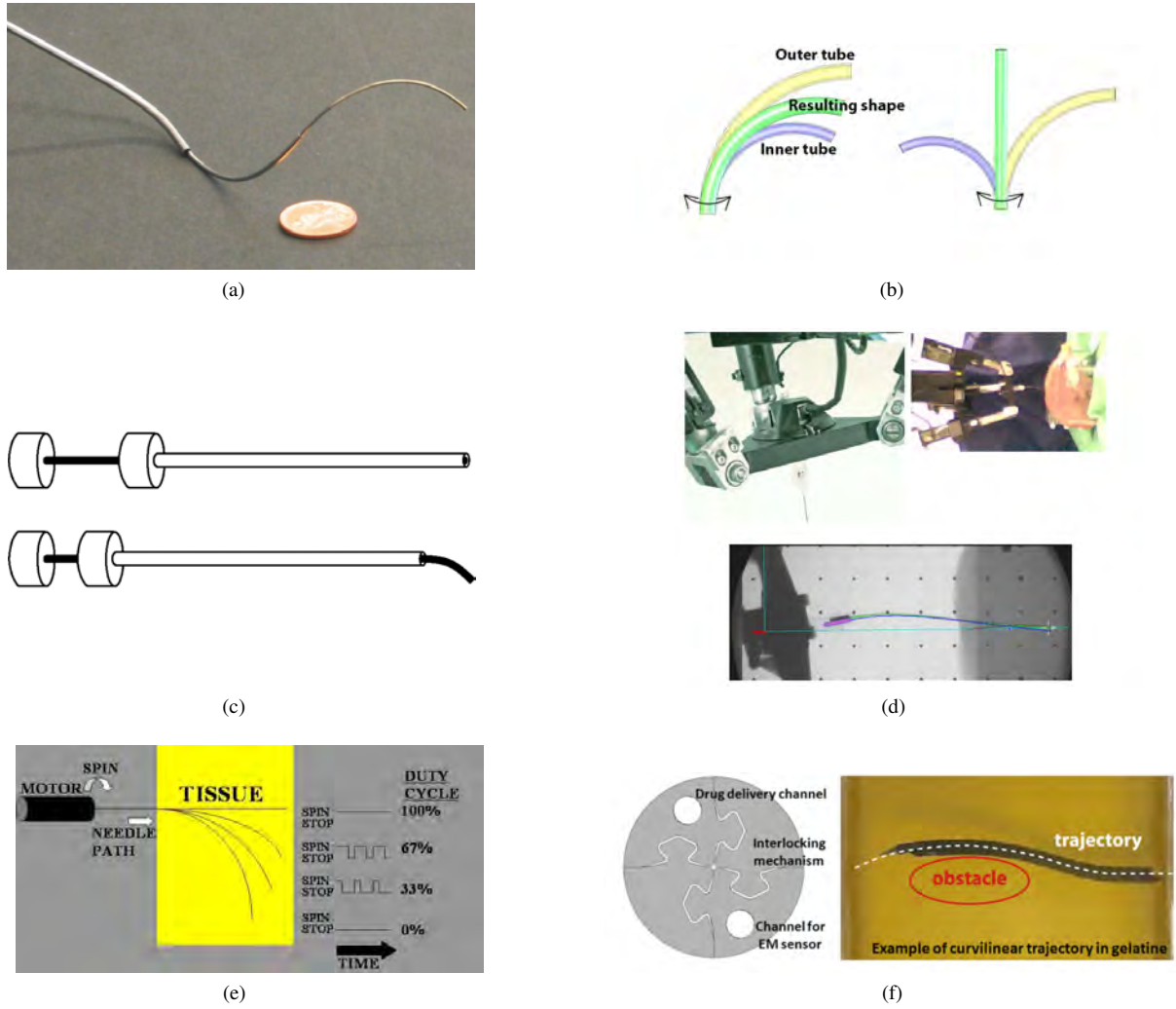


Fig. 1: Steerable needles: state-of-the-art. (a) Pre-bend, axially protruded needles shaped into a curved trajectory. Curvature is controlled by selection of needles pre-bend with the desired curve radii for each part of the trajectory (Webster, 2006). (b) Pre-bend concentric needles shaped into a curved trajectory. Curvature is controlled by the relative rotation of the needles with respect to each other (Sears & Dupont, 2006). (c) A needle with a pre-bend tip axially protruded through a stiffer cannula. The relative protrusion of the pre-bend needle with respect to the cannula determines the curvature of the trajectory. The cannula follows the trajectory of the tip (Okazawa, 2005). (d) Images showing the manipulation of a needle base outside the tissue and the resulting curved trajectory of the needle inside the tissue. The mechanism relies on tissue reaction forces for bending of the needle (Glozman, 2007). (e) The procedure of inserting a constant bevel angle needle by means of a spin-and-stop duty cycle. Small curve radii can be achieved by no spinning of the needle, and large curve radii are achieved by constant spinning of the needle (Eng et al., 2006). (f) Needle consisting of four interlocked parts. Relative protrusion of the needle parts with respect to each other creates a controllable bevel angle (variable bevel). This relative protrusion defines the direction of the asymmetric forces on the needle tip such that curvature can be controlled when pushing the needle further into the substrate (Frasson et al., 2011).

2009). A straight trajectory is cut when the needle rotates with constant speed, and a curved trajectory is cut when the needle is not rotated. The relative amount of rotation with respect to no rotation determines the curvature of the trajectory. Needles with a variable bevel angle consist of multiple interlocked parts, the relative position of which determines the effective

bevel angle of the entire needle. Curvature is controlled by the relative offset between needle parts, resulting in a change of the bevel angle. (Figure 1f; Frasson et al., 2011; Leibinger et al., 2014). This type of steerable needles is inspired by the ovipositor of wasps.

Due to their dependence on tissue reaction forces for control

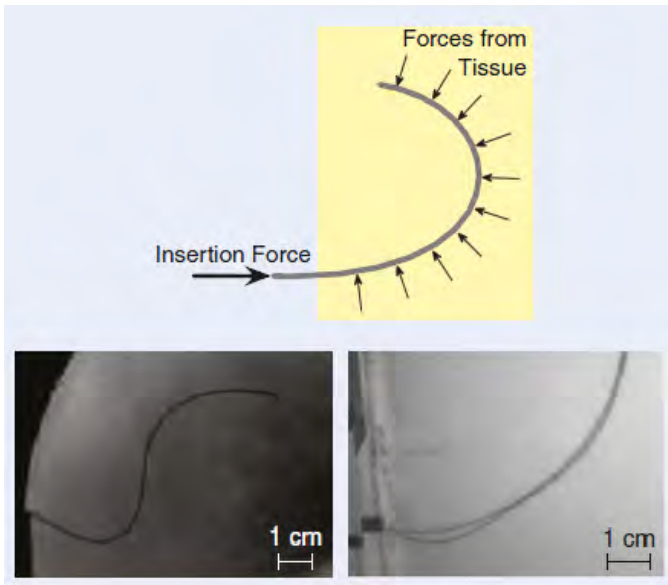


Fig. 2: Example of lateral slicing needles. Reaction forces from the tissue are insufficient to compensate the insertion force causing the needle to slice laterally (Kyle et al., 2011)

of curvature, externally steered needles may cause higher tissue strain and unintentional tissue tearing than internally steered needles (Sears & Dupont, 2006; Cowan et al. 2011). Particularly at greater depths of penetration, limited torsional stiffness can lead to lack of control for beveled needles controlled by rotation (Webster, 2005, 2006, 2009). The problem of tissue tearing due to needle buckling inside the substrate was described by Kyle et al. (2011). The axial load applied on the back of a needle increases with resistive forces on the needle tip and shaft when penetrating deeper into the substrate. The tissue can only support this axial force up to a certain depth in the tissue (Figure 2). Further protruding of the needle causes lateral slicing of the needle, leading to severe tissue damage.

C. The wasp ovipositor

The egg-laying organ (ovipositor) of wasps within the Hymenopteran insect order has been used in the past as a source of inspiration for steerable needle design (Frasson et al., 2008; 2009; 2010; Parittotokkaporn et al., 2009; Oldfield et al., 2013; Burrows et al., 2013; Leibinger et al., 2014). The mechanisms used by wasps to penetrate and steer their ovipositors, sometimes into solid wood with drilling aspect ratios of approximately 1 : 500 (calculated from Le Lanic & Nenon et al., 1999), can possibly provide an excellent paradigm to overcome functional limitations of current steerable needles. This section explains the basic anatomy of the wasps ovipositor and gives a brief overview of how wasps are able to penetrate and steer through solid substrates.

1) *Anatomy*: The wasps ovipositor is a needle-like structure, devoid of any intrinsic musculature, extending from the last

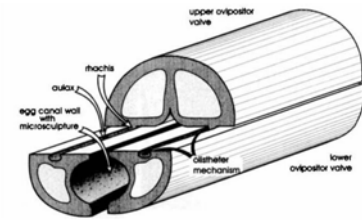


Fig. 3: Schematic representation of the wasps ovipositor, showing the olistheter connection between the dorsal valve and the ventral valves (Rahman et al., 1998)

abdominal segments of the wasp and serving the main purpose of egg deposition. It consists of three longitudinal segments called valves (Figure 3). There are two lower valves (also called ventral valves) and one upper valve (also called dorsal valve). The upper valve is connected to the two lower valves along its length by means of a tongue-and-groove mechanism called an olistheter. The olistheter allows for relative movement of the three valves in the direction of the ovipositor and prevent separation of the valves during insertion into a substrate. The wasp is able to actuate the valves individually and independently of each other with musculature located in the abdomen of the insect (Scudder, 1971; Rahman, 1998).

2) *Penetrating (push/pull mechanism)*: The wasp penetrates the substrate by antagonistically moving the ventral valves of the ovipositor (Figure 4). Serrations at the ovipositor tip allow the valves to anchor against the substrate. If one of the ventral valves anchors, the other ventral valve penetrates the substrate using the dorsal valve as sliding support. It has been hypothesized that, in order to prevent the ovipositor from buckling, the wasp applies a pull force on the anchored valve, allowing it to load the penetrating valve with a push force that is significantly higher than its critical buckling load such that the penetrating valve protrudes further into the substrate. This increase in axial load is estimated at approximately 10 times the critical buckling load of the ovipositor for *M. n. nortoni* (assuming that the ovipositor behaves as a beam element subjected to Euler buckling; Vincent & King, 1995).

3) *Steering*: Three steering mechanisms incorporated in the ovipositor have been identified by Quicke et al. (1995) and Quicke (1991) (Figure 5). The first mechanism is found within the ovipositor of *Zaglyptogastra afenestrata*. The valves of the ovipositor comprise a chain of arched thickened sections. The ovipositor is straight when the arched sections on the dorsal and ventral valves are aligned, whereas the relative protrusion of one of the valves makes the arched sections align with the nodal section of another valve causing the ovipositor to flex (Quicke, 1991).

A second steering mechanism has been found in the ovipositor of the fig penetrating wasp (*Idarnes flavicollis*). The valves are pre-bend with the bend directed inwards, comparable to the steerable needle mechanism applied by Okazawa et al. (2005). Relative protrusion of a valve leaves the valve unsupported by the other two valves, causing its tip to form to its pre-bend shape (personal communication with D.L.J. Quicke). Elias et

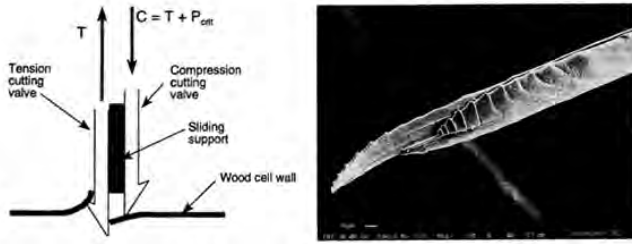


Fig. 4: Schematic representation of the hypothesized working principle of penetration. This push/pull mechanism allows the wasp to apply on the protruding valve a load greater than the critical buckling load. The SEM image (right) shows the tip of the ovipositor of *Megarhyssa nortoni nortoni*, an Ichneumonoid parasitoid wasp (Vincent & King, 1995)

al. (2012) provided visual evidence of the complex curved drilling of *Idarnes flavicollis*, killed in the act of drilling (similar to Compton & Nefdt, 1988, who also reported on observations of complex curved trajectories drilled by wasps ovipositing in figs).

A third mechanism was identified in subfamilies of the Braconidae by Quicke et al. (1995) and Quicke and Fitton (1995). In these subfamilies, movement of the valves with respect to each other is limited by pre-apical barriers. Flexing occurs when one valve is protruded relatively to the other. The barriers prevent relative movement between the valves at the tip, as a result of which the accommodation of the relative extension of one valve results in a curved ovipositor. This bending mechanism can be compared with the zip-lock of resealable plastic bags. A zip-lock with the connection between zips on one side removed, bends when one halve of the zip-lock is protruded.

D. Research question and goal

Past research into the development of a steerable needle based on the wasps ovipositor has been focused on three main subjects: steering with a multipart needle with a variable bevel angle, reduction of tissue damage by means of reciprocal insertion of a multipart needle and zero net push force tissue traversal with anisotropic surface textures.

First, curvature control during penetration is achieved in 8 directions (up, down, left, right and the corresponding diagonals) with an 8-mm diameter four-part needle with a variable bevel angle prototyped by Burrows et al. (2013) (similar to the needle displayed in Figure 1f). Curvature is controlled by the relative offset between the four needle parts resulting in the change of bevel characteristics. Penetration is achieved by means of a push force on the back of the needle.

Second, a successful effort to reduce tissue damage with a variable bevel four-part needle as compared to rigid needle insertion is made by Oldfield et al. (2013). A four-part needle prototype with inward directed beveled tips (similar

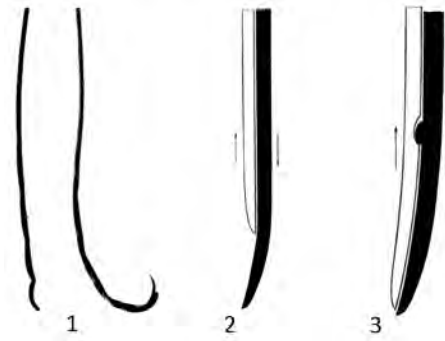


Fig. 5: Schematic representation of three steering mechanisms found within the ovipositor of wasps. 1. The ovipositor valves of *Zaglyptogastra afenestrata*, consist of a chain of arched sections, flexing when the arched sections on one valve align with the nodal sections of another by relative protrusion of the valves (Quicke, 1991). 2. The ovipositor of *Idarnes flavicollis* consists of inward directed pre-bend valves. Relative protrusion of the valves causes flexing of the ovipositor tip (personal communications with D.L.J. Quicke). 3. The ovipositor valves contained by subfamilies of the Braconidae are restricted in their movement by pre-apical barriers. The accommodation of the relative extension of one of the valves results in a curved ovipositor (Quicke et al., 1995).

to Figure 1f) and a total diameter of 6 mm is reciprocally inserted such that during penetration only one of the four needle parts traversed the tissue. The research showed that cyclic actuation of the needle parts can reduce tissue strain (Oldfield et al. 2013). Current effort of this research group goes into miniaturization towards a 4-mm diameter four-part needle (Leibinger et al., 2014).

Third, the successful result of zero net axial force tissue traversal with the help of micro-structures shown by Frasson et al. (2009, 2010) and Parittotokkaporn et al. (2009). Substrate samples supported by a low friction bearing are subjected to reciprocally moving anisotropic surface textures with the goal to traverse the tissue samples without applying a net push force. Research performed by Aoyagi et al. (2012) based on insertion methods of the mosquito proboscis shows that penetration of a substrate with a multipart micro needle comprised of serrated stylets is possible without applying a net push force.

It is believed that serrations on the wasps ovipositor valves are used to create a large difference in friction between the protruding valve versus the two anchored valves such that high cutting forces can be overcome (serrations are applied by Parittotokkaporn et al., 2009). The serrations used by wasps to induce a friction difference between protruding valves and stationary valves would not be preferable in medical steerable needles and possibly not necessary. Combining the principle of zero net push force penetration and the methods applied by Oldfield et al. (2013) for tissue damage control led us to addressing the following research question:

Can a multipart needle penetrate tissue phantom material without applying a net push force by using a friction difference induced between protruding needle parts and stationary needle parts solely based on the difference in surface area subjected to needle-tissue friction?

The goal of this research is to develop a multipart needle prototype to test the principle of zero net push force penetration in gelatin phantom with a needle devoid of any tissue gripping textures by applying a reciprocal movement to the needle parts. The influence of gelatin concentration, needle-part offset (i.e., protrusion of one needle part relative to another during each cycle), needle-part protrusion sequence and needle-part velocity on the performance of the multipart needle is investigated. The first part describes the development of the prototype and the second part presents the experimental evaluation of the prototype.

II. DESIGN OF A MULTIPART NEEDLE

One way to test the principle of substrate penetration by a needle with zero net axial force is to keep the needle stationary and leave the substrate free to move with minimal friction. If the principle holds, the needle will be gaining depth into the substrate by pulling the substrate towards the needle base. Another way to test the same principle is to keep the substrate stationary while the needle is free to move with minimal friction. In this case, the principle of penetration with zero net axial force holds if the needle gains depth into the substrate by pulling itself toward (and deeper into) the substrate. Here we opted for a stationary substrate and a free-to-move needle. The first section describes the requirements that the multipart needle prototype should fulfill. The second section describes the design considerations for the prototype whereas the actual design is described in the third section.

A. Requirements

1) Needle:

- *Needle diameter* ≤ 2 mm. Commonly used hypodermic needles vary in diameter between ± 0.2 mm (gauge 34) and ± 4.3 mm (gauge 7; Syringe Needle Gauge Chart, 2014).
- *Needle length* > 200 mm. A length of at least 200 mm was chosen to explore the effect of penetration depth on the behavior of the needle (Frasson et al. 2011: four-part probe length = 200 mm).
- *Smooth and homogeneous surface finish* < 0.6 Ra. To investigate whether penetration with zero net axial force is possible by relying solely on the difference in surface size (and thereby needle/substrate friction force) between the protruding and retracting needle parts, a smooth and homogeneous surface finish is required. Here we differentiate from the prototype presented by Parittotokkaporn (2009) where saw tooth microstructures are applied to induce direction dependent friction.
- *Sharp needle tip*. Tip geometry must be designed such that the cutting forces are minimized.

2) Actuation mechanism:

- *Low friction movement*. The needle and its actuation mechanism must be able to travel with minimal friction.
- *Low inertia*. The needle and its actuation mechanism must be of low weight such that the components are set to motion with minimal force.
- *Needle-part offset* [0-25 mm]. The actuator must be able to vary the needle-part offset between 0 and 25 mm (in line with the offset of 12-27 mm used in the multipart needle experiment performed by Burrows et al. 2013)
- *Needle-part velocity* [0-15 mm/s]. Needle-part velocity range was chosen such that it is comparable to previous steerable needle validation experiments (Frasson et al. 2012: 1 mm/s forward motion, Webster et al. 2005: 5-25 mm/s, Misra 2009: 2.5 mm/s).
- *Needle protrusion sequence* [-]. The actuation mechanism must be suitable for every possible actuation (thereby protrusion) sequence of needle parts.

B. Design considerations

Complexity of the manufacturing process (e.g., number of parts and manufacturing steps), weight, size and availability of components, complexity of control and the extend of similarity to the wasps ovipositor are important criteria in the weighing of design options. The considerations that mostly affected the design are discussed.

1) *Number of needle parts*: In order to induce a friction difference based on the size of the total surface area of protruding versus stationary needle parts, the number of stationary needle parts must exceed the number of protruding needle parts (i.e., a number of three needle parts is thus required). The design of a square four part needle allows for manufacturing of needle parts in one piece out of a single sheet of stainless steel, whereas a round needle can be manufactured with the minimum number of needle parts required. A round needle shows better resemblance with the ovipositor but leads to more complex manufacturing, therefore a four-part square needle was chosen for this first prototype.

2) *Needle interconnection*: Three possible methods for preventing possible separation of needle parts during substrate penetration were considered. Internal interconnections similar to the olistheter structures in the wasp ovipositor make manufacturing complex due to the small tolerances, dimensions and number of manufacturing steps. External connections at certain intervals along the length of the needle, would ease manufacturing but would also interfere with the needle-substrate interaction. The use of reaction forces from the substrate to keep the needle parts together by means of an inward directed force on a bevel angle, bears good resemblance to the wasp ovipositor and is relatively simple to manufacture in terms of the number of parts and the complexity of the needle parts.

3) *Actuation mechanism*: Several mechanisms can deliver a linear reciprocal movement. A transformation from rotational movement to linear movement can, for example, be achieved with a pinion and rack, screw and nut or a crankshaft mechanism. Direct linear movement can be achieved by pneumatic/hydraulic cylinders but pneumatics and hydraulics are

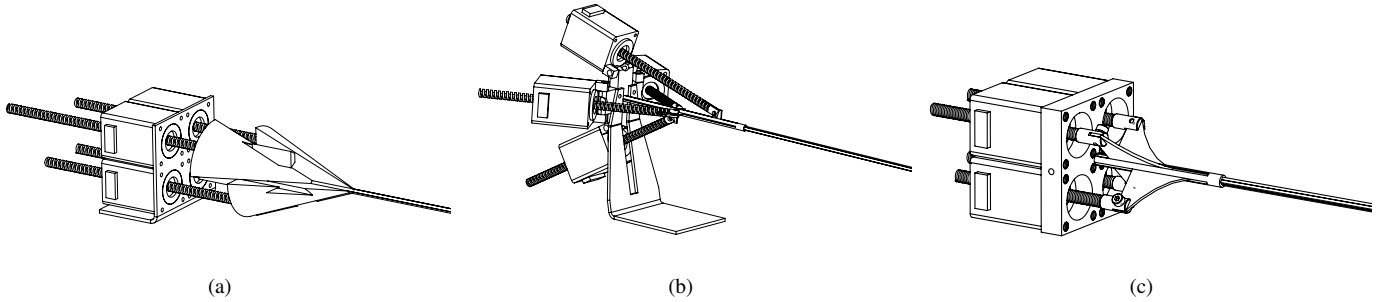


Fig. 6: Needle actuator concepts. (a) Sketch showing a suspension concept with a tongue-and-groove interconnection between needle parts. The needle parts start with a conical part that is sufficiently large for incorporating a tongue and groove interconnection. (b) Sketch showing a suspension concept with pivoting actuators. Pivoting actuators allow for the needle fins to be kept short such that needle-part driving force is applied close to the center line of the needle, preventing the mechanism from flexing at the base. (c) Sketch showing the suspension concept applied in the prototype. The actuator configuration is compact and the needle parts are supported by a guide tube.

heavyweight and require external connections. Control of offset in crankshaft mechanisms is relatively difficult to achieve, making incorporation of a crankshaft mechanism less favorable over the other rotation/translation transition possibilities. For availability reasons and ease of connection to a needle-part, the choice was made for a screw and nut.

4) *Type of motor*: Motors can be feed-forward controllable (e.g., AC and stepper) or feedback controllable (e.g., DC) motors. Feed-forward control is easy to implement, and stepper motor assemblies containing a spindle and internal nut are readily available. Stepper motors are therefore used in this prototype.

5) *Actuator and needle suspension*: The actuator configuration is designed such that the needle parts are prevented from parting and such that any bending moment, applied by the actuators on the protruding needle part, is compensated by either the stationary needle parts or a needle guide structure. A total of three concepts have been considered (full-size sketches are provided in appendix A).

In the first concept, the needle parts end at their base in a conical shape. The needle parts are interconnected by a tongue-and-groove mechanism applied on the base of the needle (Figure 6a). The tongue-and-groove mechanism supports the bending moment generated by the difference between the engaging point of the actuator force (at the circumference of the conical needle base) and the engaging point of the friction forces between needle parts (center planes of the needle). The number of parts in such a configuration is small, partly due to the compact linear actuator configuration, but the complexity of manufacturing is high due to, among others, the large diameter variation throughout the needle length and the tongue-and-groove connection.

A four-part needle concept with the needle parts supported in a guide tube, to keep the needle parts together at their base, and small fins for connection to the actuator spindles is shown in Figure 6b. The guide tube contains slots through which the

needle fins are allowed to move back and forth. The spindle connection is close to the needle center line, thereby limiting the bending moment on the needle parts, but the actuator configuration becomes more complex as compared to the first concept, since there is no space to keep the spindles parallel. The actuators must be able to pivot so that the spindle remains concentrically with respect to the nut inside the actuator, resulting in a significantly higher number of parts.

The third concept incorporates the best features of these two concepts (Figure 6c); the compact actuator configuration with a low part count is easy to manufacture and the guide tube with slots allows for easy manufacturing and sufficient needle support. This concept is applied in the prototype.

C. Description of the prototype

The prototype is designed using Solidworks (Dassault Systems SolidWorks Corporation; Waltham, MA, USA). First, the hardware is described (Figure 7): needle, needle suspension, linear actuator, low friction cart and electronics, followed by the software: user interface and embedded software.

1) *Hardware*: The prototype consists of a cart suspending a four-part needle assembly, a linear actuator assembly containing four linear actuators and driving electronics to reciprocally move the needle parts back and forth. A user-interface at the top of the cart allows to set the needle-part offset, the sequence of needle-part protrusion and the velocity of protrusion and retraction. The propagation of the needle is realized in cycles, each of which consists of a protrusion phase and a retraction phase. During the protrusion phase the needle parts are protruded one-by-one (or two-by-two, depending on the sequence setting) with respect to the cart over a distance equal to a predefined offset. During the retraction phase the needle parts are retracted altogether with respect to the cart over a distance equal to the offset.

The needle assembly consists of four, square needle parts stacked two-by-two and a guide tube to support the needle

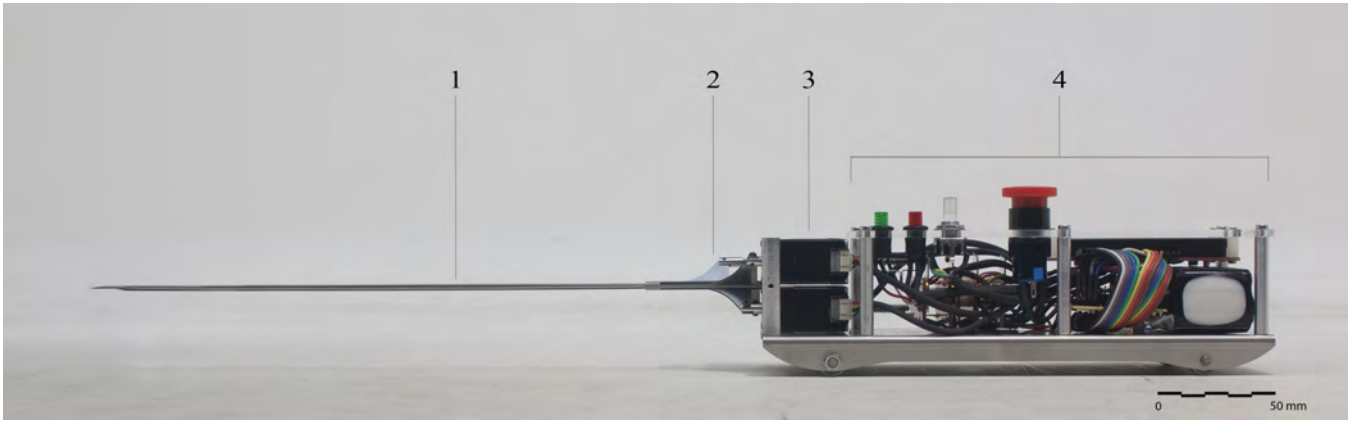


Fig. 7: Image of the prototype. Showing the needle (1), needle assembly (2), linear actuator assembly (3) and the low friction cart including the driving electronics (4).

parts (Figure 8a). The tip of the needle is conical (angle of approximately 20°) and sharp (Figure 8b). Each needle-part ends in a fin at the base of the needle containing a slot through which the needle parts are connected to the linear actuators. The guide tube contains a square hole through which the needle parts can slide freely, and four slots through which the needle part fins are allowed to move up to 25 mm in the longitudinal direction of the needle. An insert fills the open end of the guide tube created by the slots, to prevent the hole of the guide tube from closing when clamping the guide tube. The needle parts are manufactured out of a 1-mm thick rolled stainless steel sheet using wire EDM. The guide tube is made of a stainless steel rod. The square hole is made using wire EDM, after which the slots for the needle parts are milled.

The fin of each of the four needle parts is mounted to a lead screw. The lead screws are translated back and forth by four Nanotec ST2018S0604-A linear stepper motors (with a resolution of 1.8° , corresponding to 0.0061 mm/step of lead screw translation), which are mounted in a 42x42x8-mm aluminum bracket to form the actuator assembly (Figure 8c). The stepper motors rotate a nut suspended by two bearings inside the stepper motor, causing the lead screw to translate through the middle of the stepper motor. The needle-part guide tube fits inside the hole centered in the middle of the bracket and is clamped by a set screw. Two alignment pins, extending from the bottom of the bracket (not visible in Figure 8c), align the needle and actuator assembly with a low friction cart.

A 1-mm thick stainless steel flanged base plate forms the basis of the low-friction cart. The base plate is supported by two axis, each containing two single-row deep-groove ball bearings with metal shields (624-ZZ, 4x13x5 mm). The bearings are lightly press-fitted on two 4-mm diameter axes and held to place with two retaining rings. Axis rotation is prevented by a nut clamping one of the base plate flanges to one of the outer retaining rings. The base plate contains alignment holes to fit the pins extending from the bottom of the bracket (Figure 8d).

The electronic components driving and controlling the linear

steppers are mounted behind the linear actuator assembly. Four stepper drivers (Allegro, 3967SLB) are mounted directly behind the linear actuator module. The drivers are controlled with a micro-controller (Arduino Pro Mini 328, 5V, 16Mhz). A two-row LCD display (Xiamen Amotec Display Co., Ltd ADM1602K1-FS-FBW) displays a timer and cycle counter during actuation and settings when standby. The settings are controlled by two push buttons and a rotary encoder. The system is battery powered (lithium-ion, 1600mAh), with the battery mounted opposite to the linear actuator assembly on the low-friction cart (Figure 8d).

2) *Software*: The embedded code is written in C++ including Arduino libraries. The software consists of two parts: a user interface part containing a rotational encoder with a push button, a green button, a red button and the display driver component, and an embedded part containing the register, stepper sequence controller, stepper controller and the stepper driver (appendix D-A).

III. HYPOTHESES

Zero net push force penetration with a four-part needle solely based on the difference in friction due to the difference between the number of anchoring (i.e., stationary) needle parts and the number of protruding needle parts would require the protrusion of one needle part at a time while the remaining three needle parts act as a sliding support. Measurements performed by Hing (2006) and Simone and Okamura (2002) in porcine liver show that friction force on a 1.27-mm diameter needle increases approximately linearly with penetration depth whereas, needle cutting forces remain approximately constant along the depth of penetration (our pilot tests showed similar behavior in Dr. Oetker gelatin). This leaves us to believe that, when protruding one valve at a time, an equilibrium between the friction force on the stationary needle parts and the resistive forces (i.e., sum of cutting force and friction force) on the protruding needle part is reached at a certain depth of penetration (Equation 1). From this depth and forward, friction forces of the stationary needle parts should be higher than

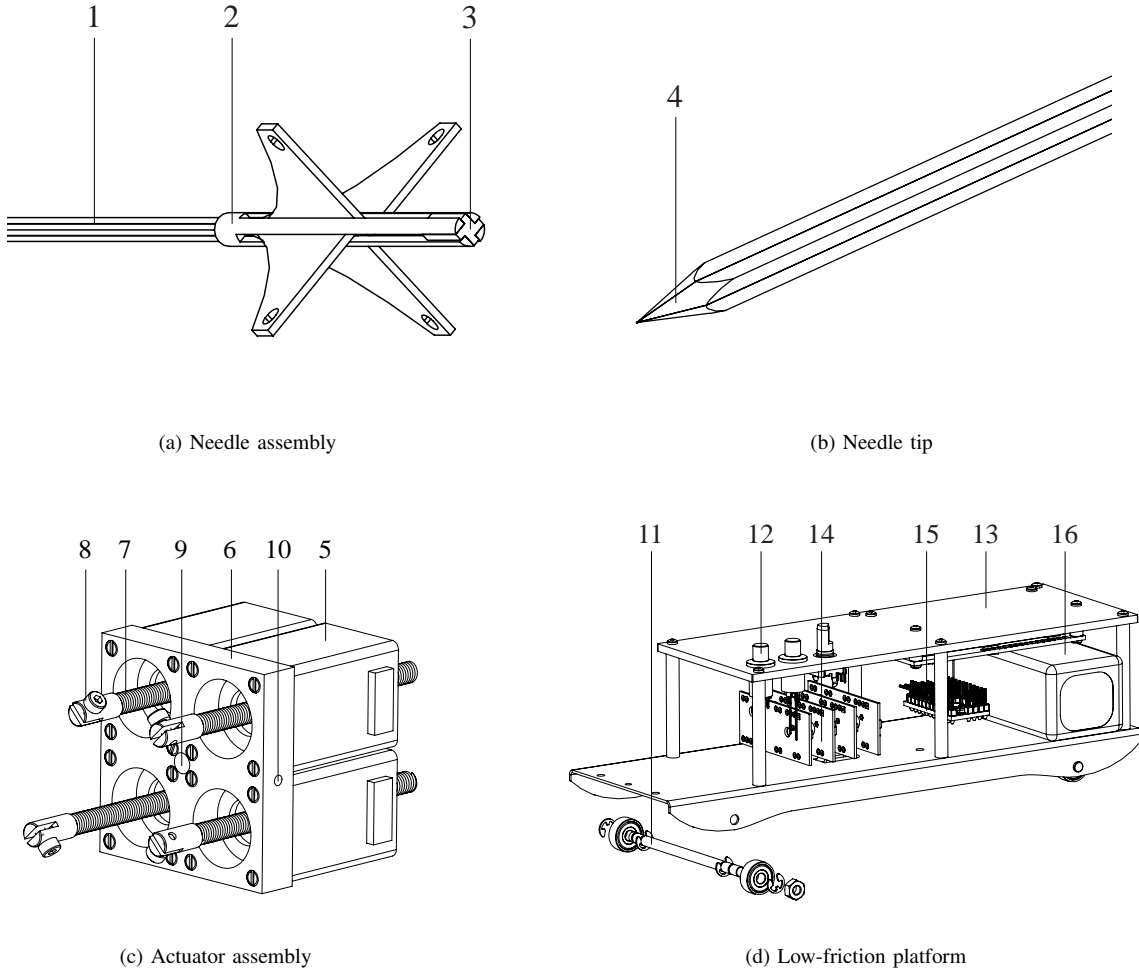


Fig. 8: (a) Sketch of the needle assembly. The needle consists of four square 1x1 mm needles which are stacked in a circular manner, forming the square needle (1). The needle is free to slide through the guide tube (2) and clamping is prevented by an insert (3). (b) Sketch of the needle tip. The tip (4) is conical and sharp. (c) Schematic representation of the actuator assembly. Four linear actuators (5) are mounted to a bracket (6). The lead screws (7) contain a fin clamp (8). The guide tube is mounted in the middle of the bracket (9) and secured with a set screw (10). (d) Sketch of the low friction cart showing the bearing assembly (11), control buttons (12), LCD screen (13), stepper drivers (14), micro-controller (15) and battery (16).

the resistive forces on the protruding needle part due to the proportional relation between needle-substrate friction force and penetration depth, making penetration with zero net push force possible.

$$\frac{1}{4}F_c + \frac{1}{4}F_f = \frac{3}{4}F_f \quad (1)$$

The performance of the prototype will be assessed in terms of the degree of slipping of the needle with respect to the substrate (with less slip implying better performance).

1) *Protrusion sequence*: The size of the surface area subjected to resistive forces during the protrusion phase is the

same, independently from the order in which the needle parts are actuated and protrude the gelatin. It is thus expected that the performance of the needle is not affected by the protrusion sequence. Also, penetration with needle parts actuated in a two-by-two manner is expected to result in no penetration at all, since in that case the frictional force on the stationary needle parts is smaller than the resistive forces on the protruding needle parts.

2) *Needle-part velocity*: According to van Gerwen (2007) needle-substrate friction force increases with insertion velocity more steeply than the corresponding cutting force. Following Equation 1 it is thus expected that the needle performs better

at higher velocities.

3) *Gelatin concentration*: To overcome bearing friction and inertia, the cart requires sufficient needle-substrate friction. In the extreme case of very low gelatin concentrations it is expected that no penetration will occur due to insufficient friction force. On the other hand, the wood-wasp ovipositor is hypothesized to use its serrations to increase the friction force on anchored valves such that the protruding valve is able to overcome the high cutting force in hard substrates. This would suggest that resistive forces on the protruding needle parts are dominant in higher concentrations leading to poor performance. An optimum in gelatin concentration for which performance is best is thus expected.

4) *Offset*: For high offsets it is expected that the friction force on the protruding needle part is higher due to the larger surface subjected to needle-substrate friction as compared to low offsets. This would mean that the prototype performs worse with higher offsets since the protruding needle-part undergoes higher resistive forces.

IV. METHOD

Two experiments are conducted to test if zero net push force penetration with a four-part needle solely based on the difference in friction due to the difference between the number of stationary needle parts and the number of protruding needle parts is possible. In the first experiment, the effect of gelatin concentration, needle-part offset, needle-part velocity and needle-part sequence on the performance of the prototype is measured (called henceforth prototype experiment). In the second experiment, force measurements are conducted during the insertion of the prototype needle assembly into gelatin (called henceforth force experiment). The relation between cutting force and friction force for various needle velocities and gelatin concentrations estimated based on the force experiment, is used to support the findings of the prototype experiment.

A. Experimental setup

1) *Prototype experiment*: A platform is constructed to create a level surface for the cart to travel back and forth between a proximity sensor and a gelatin sample (Figure 9). The platform consists of a frame made from square aluminum tubing and a 500x500x8-mm acrylic top plate. Adjustment screws for leveling run through rivet nuts on the four corners of the frame. The platform is leveled using a 0.02-mm/m spirit level.

Gelatin substrates are produced in 434x344x107-mm trays. One panel of the tray has a 20 x 2 grid of 15-mm diameter holes, each 40 mm apart, allowing for needle entry. The tray is set to height with spacers, and oriented such that the panel with holes is positioned against the platform. The distance to the proximity sensor is identical for all trays.

A Micro-Epsilon optoNCDT1302-200 (with a range of 200 mm and a resolution of 0.1 mm) laser proximity sensor is used to measure the traveled distance of the prototype during penetration. The sensor is mounted on a bracket and placed against the platform to ensure a constant distance between laser sensor and gelatin tray. Sensor data is gathered at a sample rate of 50-Hz using LabVIEW 2010 in combination with a

National Instruments NI USB-6210 16-bit data acquisition system (appendix B-B).

2) *Force experiment*: The four needle parts and guide tube are clamped to a force sensor assembly oriented vertically with the tip directed downwards. The needle is linearly translated by means of a linear stage. A 80x160x200-mm gelatin container is positioned underneath the needle. The axial force on the entire needle is measured during the insertion and retraction movement of the four-part needle assembly as a whole (Figure 10, appendix B-C).

The four needle parts are glued together just before the tip using cyanoacrylate (Loctite 401) to prevent separation of the needle parts during the measurements. Using a magnifying glass it is made sure that no glue adheres to the outside surface of the needle.

The force sensor assembly consists of a mechanical decoupler which holds a Futek-LSB200-5Lb force transducer. The left decoupler side is used to set a pretension on the force transducer by a hex screw which compresses a parallel spring on the right decoupler side with the force transducer. The decoupler assembly is statically calibrated with balance weights ranging between 0.25 and 1.0 Kg in steps of 0.25 Kg. (appendix H).

The needle and sensor assembly is mounted to an Aerotech PRO 115-400 5-mm/rev linear stage. The stage is powered by a Maxxon EC40 brushless motor driven by a Maxxon 4-Q-EC servo-amplifier. Position feedback is provided by a Scancon 2RMHF-7500 incremental encoder containing 7500-pulse/s. Data acquisition and position control is performed by a dSPACE DS1104 real time controller board in a PC running MS Windows 7 on an AMD Athlon X2 5200+, 4GB RAM. Analog signals are sampled with 1-KHz.

B. Variables

1) Independent variables:

- *Needle-part offset [mm]*: The amount of protrusion of the protruding needle parts relatively to the stationary needle parts. Offset is varied between 3, 10 and 20 mm.
- *Needle-part velocity [mm/s]*: The protrusion and retraction velocity of the needle parts with respect to the cart. The velocity is varied between 4, 8 and 13.5 mm/s, where 13.5 mm/s is the maximum velocity generated by the linear actuators of the prototype.
- *Gelatin concentration [wt%]*: Gelatin concentration determines the visco-elastic behavior of the substrate and is varied between 2, 8 and 13 wt%.
- *Needle-part sequence [-]*: The sequence of protruding needle parts is varied between circular, diagonal and a two-by-two manner of actuation.

2) Dependent variables (measured):

- *S_a [mm]*: The actual distance traveled by the cart is measured dynamically with the laser proximity sensor.
- *Number of cycles (N) [-]*: The number of cycles performed by the cart to travel a given distance. One cycle starts with a protrusion phase in which all four needle parts are protruded one by one over a distance equal to the offset and ends with a retraction phase in which all

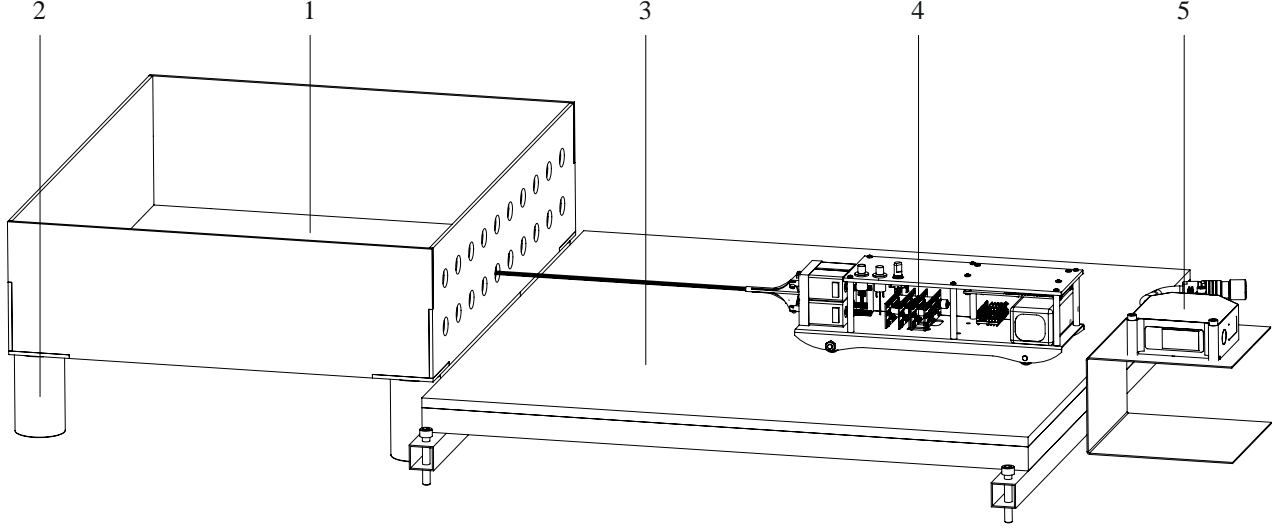


Fig. 9: Setup for position measurements during the penetration of a gelatin substrate. The gelatin tray (1) is supported by spacers (2) and placed against an height adjustable platform (3). The prototype (4) is able to travel back and forth between the tray and a laser proximity sensor. The sensor is mounted on a bracket and placed against the platform.

four needle parts are retracted simultaneously towards the cart.

- F_i [N]: The axial force acting on the needle during the insertion movement is measured with the force transducer shown in Figure 10. F_i represents the sum of needle cutting force and needle-substrate friction force (Hing, 2006).
- F_f [N]: The axial force on the needle during the retraction movement measured with the force transducer (Figure 10). The retraction force represents the needle/-substrate friction force (Hing, 2006).

3) Dependent variables (derived):

- S_t [mm]: The theoretical traveled distance defined as the distance traveled if there is zero slip. S_t is calculated as the number of cycles multiplied by the offset.
- $Slip_{pro}$ [mm]: Slip in the protrusion phase equals the backwards traveled distance of the cart during the protrusion of the four needle parts in one cycle.
- $Slip_{ret}$ [mm]: Slip in the retraction phase equals the difference between the offset and the actual traveled distance in the retraction phase.
- $Slip\ ratio\ (SR_{tot})$ [-]: The slip ratio represents the ratio between S_a and S_t . Slip ratio over the total measurement is determined by Equation 2. A decoupling of slip can be made between slip in the protrusion and retraction phases. The slip ratio in a protrusion phase (SR_{pro} ; Equation 3) is the distance that the cart travels backwards during the protrusion of the needles with respect to the offset. The slip ratio in a retraction phase (SR_{ret} ; Equation 4) is the ratio between the actual traveled distance in the retraction phase and the offset. The slip ratio is considered to be a performance measure of the

system, with less slip meaning less dependence on the net axial push force on the needle. SR_{tot} is decoupled into SR_{pro} and SR_{ret} to gain insight in the origin of slip.

$$SR_{tot}[-] = 1 - \frac{S_a}{S_t} \quad (2)$$

$$SR_{pro}[-] = \frac{Slip_{pro}}{Offset} \quad (3)$$

$$SR_{ret}[-] = 1 - \frac{Slip_{ret}}{Offset} \quad (4)$$

- F_c [N]: Cutting force is the axial force on the needle as a result of the subtraction of the retraction force from the insertion force (Hing, 2006).
- *Depth of equilibrium* [mm]: The depth at which F_c and F_f are in equilibrium according to Equation 1.

4) Control variables:

- *Needle position* [mm]: The needle position is defined by the feedback-controlled relative displacement of the needle in the linear stage setup.
- *Substrate temperature* [C°]: Temperature of the gelatin samples is kept between 4 and 8 C° during all experiments. Ng et al. (2013) shows that insertion force on a needle decreases significantly for a substrate temperature higher than 8 C°.
- *Ambient temperature* [C°]: Temperature of the environment during the experiments. All experiments are performed in an air-conditioned location at room temperature.
- *Needle surface lay, roughness and waviness*: The surface condition of the needle is constant over all measurements. No surface wear is expected due to the large

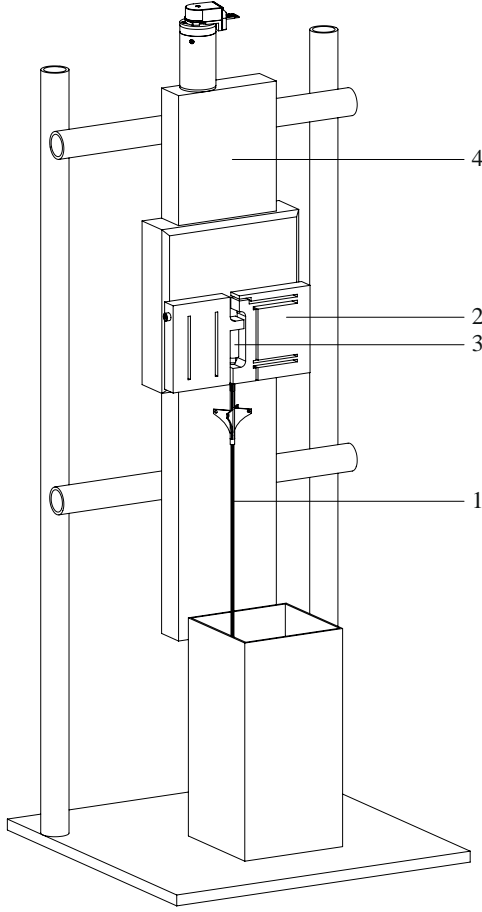


Fig. 10: Setup for the force experiments. The needle assembly (1) containing four needle parts and guide tube are mounted to a mechanical decoupler (2). The force sensor (3) is mounted inside this decoupler and the assembly is mounted to a linear actuator (4). The gelatin substrate (5) is positioned under the linear actuator.

difference in material hardness between gelatin and stainless steel. The surface roughness (R_a) was measured at approximately $0.2 \mu m$ with a needle (Mitutoyo Surftest SJ-301; appendix G).

C. Experimental procedure

1) *Prototype experiment*: Dr. Oetker gelatin is weighted with a balance (KERN & Sohn, EMB 2200-0, accuracy: $d = 1g$) and soaked for approximately 10 minutes in cold water. Hot water from a household water boiler is used to bring the sample to the required weight. The gelatin is stirred until it became a homogenous substance and cooled down to about $4^\circ C$ in the gelatin trays one day in advance of the experiment.

All prototype measurements are performed over a time span of one day. The four parameters are individually varied from

TABLE I: Prototype experiment, parameter variation

| Variable: | Sequence [-] | Offset [mm] | Gel. Con. [wt%] | Velocity [mm/s] |
|-----------|--------------|-------------|-----------------|-----------------|
| | Circular | 3 | 3 | 4 |
| | Diagonal | 10 | 8 | 8 |
| | Two-by-two | 20 | 13 | 13.5 |
| Baseline: | Circular | 10 | 8 | 4 |

TABLE II: Force experiment, parameter variation

| Variable: | Velocity [mm/s] | Gel. Con. [wt%] |
|-----------|-----------------|-----------------|
| | 4 | 3 |
| | 8 | 8 |
| | 13.5 | 13 |

a common baseline, see Table I. Measurements are repeated 5 times per each combination of variables. Allocation of measurements to a hole in the gelatin tray occurred quasi-randomly such that each set of 5 measurements in the 8-wt% gelatin sample is distributed over the upper row and lower row of three trays. All measurements in the 3-wt% gelatin and 13-wt% gelatin substrates are performed in a single tray and distributed between the upper row and the lower row within the tray (see appendix E-A).

The mechanism is positioned in front of the allocated hole and a machinist square is used to align the low friction cart perpendicular to the base of the platform. Before the start of each measurement, the needle is driven 35 mm into the substrate by manually pushing the prototype guided by the machinist square. The proximity sensor is placed against the base of the platform such that it is aligned with the cart. The proximity sensor is switched on and approximately one second later the actuation of needle parts is started. When the needle has traveled approximately 120 mm inside the gel, the actuation is stopped by a light press on the red button on the prototype and the proximity sensor is switched off.

Before each measurement, the needle is cleaned from gelatin residue with a paper tissue dipped in warm water, then dried using dry paper tissue. The platform is dusted with a paper tissue before each measurement. The velocity, offset and sequence are set using the user interface of the prototype and according to the measurement scheme in appendix E-A.

2) *Force experiment*: Gelatin samples are prepared one day in advance of the experiment similar to the prototype experiment. All force measurements are performed over a time span of one day. Needle velocity, and gelatin concentration are varied in a fully crossed manner, see Table II. Each combination of parameters is repeated 5 times (appendix E-B).

A random drilling spot along the edge of the gelatin container at least 30 mm apart from other drillings and the edge of the container is chosen and the needle is positioned within 1 mm above the gelatin sample. Needle velocity is set according to the measurement scheme as displayed in appendix E-B. The wait time between needle insertion and retraction is set to 3 seconds, which showed to be enough for the gelatin to settle (relax) around the needle (see Figure 12a). The needle is cleaned from any gelatin residue after each measurement.

D. Data analysis

Data interpretation and analysis is performed using Matlab R2013a (The MathWorks, Inc., Natick, Massachusetts, United States), m-files for both the prototype and the force experiments can be found in appendix F-A.

1) *Prototype experiment*: An example of a cart position signal for each of the three different offsets is displayed in Figure 11. The raw signal is filtered using a moving average filter over 5 samples. The steep sloped sections correspond to the retraction phase and the longer downward sloped sections correspond to the protrusion phases. The actual traveled distance (S_a) is calculated by subtraction of the mean value of the last 10 data samples and the first 10 data samples. The number of cycles (N) is determined by the number of local maxima in the signal. Slip can be decoupled into the protrusion phase and retraction phase. Slip in the protrusion phase of a single cycle ($Slip_{pro}$) is determined by subtracting the cart position after the protrusion phase of a given cycle from the cart position before the protrusion phase of the same cycle. Slip in the retraction phase ($Slip_{ret}$) is determined by subtracting the difference in cart position before and after the retraction phase of a cycle from the offset, and represents the absolute amount of substrate traversal during the retraction phase (see appendix F-A).

2) *Force experiment*: The raw force signal (Figure 12a) is filtered using a moving average filter over 100 samples and shifted such that the first 1000 data points (i.e., 1 s) of the signal average on zero. The small peak in F_i at approximately 5 mm depth indicates the depth at which the needle starts cutting the substrate, the increase in axial force during the first 5 mm of travel is caused by the increase of elastic deformation of the substrate. Maximum insertion force ($F_{i,max}$) and maximum retraction force ($F_{f,max}$) are found using the standard Matlab functions 'max' and 'min'. The moment of needle exit and the corresponding needle position is found using the needle position data captured by the setup. The first millimeter of needle travel is discarded as this represents air penetration.

The retraction force (F_f) is the part of the curve from maximum retraction to the point of substrate exit. The protrusion force is the part of the curve to the left side of the maximum protrusion part with the same length as the retraction part. The protrusion force is flipped with respect to the time axis so that it is displayed as positive (Figure 12b). The retraction force is flipped with respect to the time axis so that it is displayed as negative and with respect to the force axis such that the needle depth of both the insertion force and the retraction force can be aligned. The two data sets are aligned at their maximum force values. The resultant of the retraction and the protrusion force represents the cutting force (Figure 12b). The depth after which the cutting force and friction force on the needle parts are in equilibrium according to Equation 1 is determined by the intersection between a linear fitted retraction force and the mean value of the cutting force.

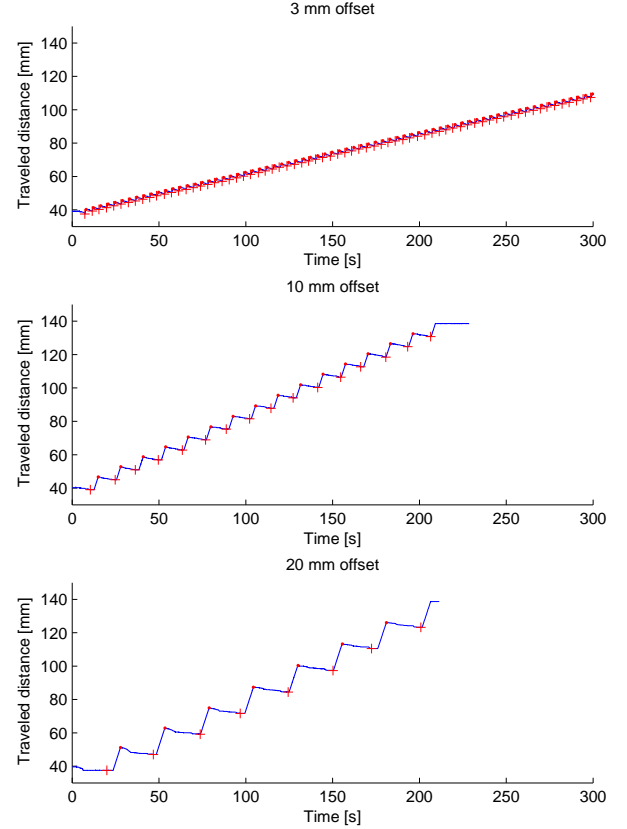


Fig. 11: Example of three measurements with different offsets. The measurements are performed in 8-wt% gelatin at 4 mm/s with circular actuation. The position of the cart is represented by the blue line. The red (+) shows the end position of each protrusion phase and thus also the start of the retraction phase. The red (.) shows the end position of each retraction step phase and thus the start of each protrusion phase.

E. Statistical analysis

A one-way ANOVA is performed to compare the means of the measured SR_{pro} , SR_{ret} and SR_{tot} as a function of the parameters according to Table I. p-values under the null hypothesis that all parameter samples within each independent variable are drawn from the same mean are presented together with the F-statistic. For the force experiments, a one-way ANOVA is performed to compare the means of the maximum friction force and the means of the average cutting force as a function of the needle velocity and gelatin concentration.

V. RESULTS

A. Prototype experiment

SR_{tot} was comparable between circular and diagonal actuation in 8 wt% gelatin at 4 mm/s ($F = 0.56$, $p = 0.48$; Figure 13).

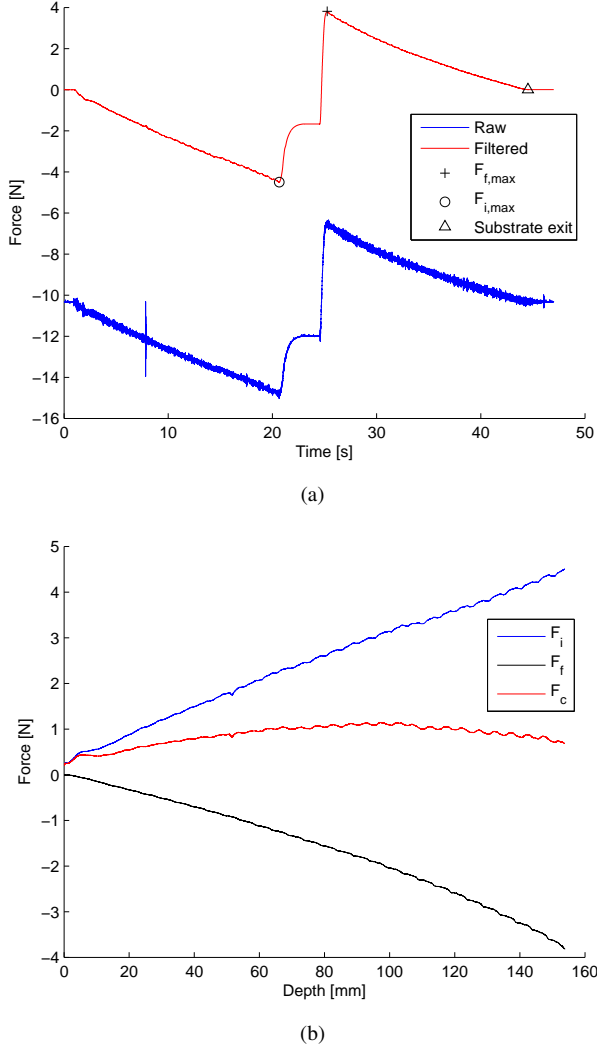


Fig. 12: Example measurement from the force experiment in 8 wt% gelatin at 8 mm/s. (a) Transition from raw signal (dotted line) to filtered signal (solid line). Maxima in insertion and retraction force are indicated by respectively the (o) and (+) mark. The time of substrate exit is indicated by the triangle. We can clearly distinguish the insertion part (0-20-s), the relaxation part where no needle displacement takes place (21-24-s) and the retraction part (24-45-s). (b) The reorganization of the insertion and retraction force. The red line represents the cutting force.

As expected, two-by-two actuation of needle parts resulted in no penetration ($SR_{tot} = 1$). Two-by-two actuation at 13.5 mm/s resulted in penetration with a slip ratio of over 0.9. An offset of 4 mm was associated with a significantly higher SR_{tot} as compared to the corresponding SR_{tot} for 10 and 20 mm ($F = 160.54$, $p = 2.19E^{-9}$; the latter two also being significantly different from each other; post-hoc paired t-test between 10 and 20 mm: $p = 0.0094$). SR_{tot} increased significantly with

TABLE III: Depth [mm] at which F_c and F_f are in equilibrium according to Equation 1

| Gel. con./Velocity | 4 mm/s | 8 mm/s | 13.5 mm/s |
|--------------------|--------|--------|-----------|
| 3 wt% | 29 | 48 | 58 |
| 8 wt% | 23 | 29 | 32 |
| 13 wt% | 19 | 22 | 24 |

gelatin concentration ($F = 154.71$, $p = 2.70E^{-9}$). SR_{tot} was comparable between all three tested velocities ($F = 1.43$, $p = 0.28$).

Decoupling of the slip ratio into the protrusion phase (SR_{prot} ; Figure 13) and the retraction phase (SR_{ret} ; Figure 13) shows whether the trends found within SR_{tot} are caused by an effect in the protrusion and/or the retraction phase. It can be seen that none of the independent variables exhibited a large effect on the slip ratio during the retraction phase as compared to the protrusion phase even though the differences in the retraction phase are significant (offset: $F = 33.2$, $p = 1.98E^{-14}$; gelatin concentration: $F = 129.69$, $p = 2.74E^{-38}$; sequence: $F = 7.04$, $p = 0.0088$; velocity: $F = 2.27$, $p = 0.11$). The slip ratio during the protrusion phase decreased with offset ($F = 669.28$, $p = 6.87E^{-156}$) and increased with gelatin concentration ($F = 1491.26$, $p = 2.68E^{-131}$), in line with the effects observed for SR_{tot} .

B. Force experiment

The friction force ($F_{f,max}$) increases with needle velocity, an effect that shows to be significant for all three gelatin concentrations (3 wt%: $F = 17.6$, $p = 0.0003$; 8 wt%: $F = 10.33$, $p = 0.0025$; 13 wt%: $F = 47.83$, $p = 1.92E^{-6}$; Figure 14). The average cutting force, estimated by subtracting of the friction force from the insertion force, increases significantly with needle velocity for 3 wt% ($F = 40.62$, $p = 4.55E^{-6}$), 8 wt% ($F = 131.3$, $p = 6.96E^{-9}$) and 13 wt% ($F = 50.91$, $p = 1.37E^{-6}$) gelatin samples.

The depth at which the cutting force and the friction force are in equilibrium according to Equation 1 is determined for varying needle velocity and gelatin concentrations (Table III). The equilibrium depth increases with increasing velocity and decreases with increasing gelatin concentration.

VI. DISCUSSION

In this article, we presented a four-part needle prototype that is developed to test the principle of penetration without a net push force using a needle devoid of surface gripping microstructures that could mechanically anchor in the (gelatin) substrate, and to get insight into the effect of gelatin concentration, needle-part offset, needle-part protrusion sequence and needle-part velocity on the needle performance. Experiments showed that a lower slip ratio (SR_{tot}) is accomplished with decreasing gelatin concentration and increasing offset, whereas neither velocity nor protrusion sequence significantly affect the slip ratio (Figure 13).

We have also conducted force measurements during the insertion of the needle as a whole (i.e., all four needle parts bound together) into gelatin to get insight into the relation

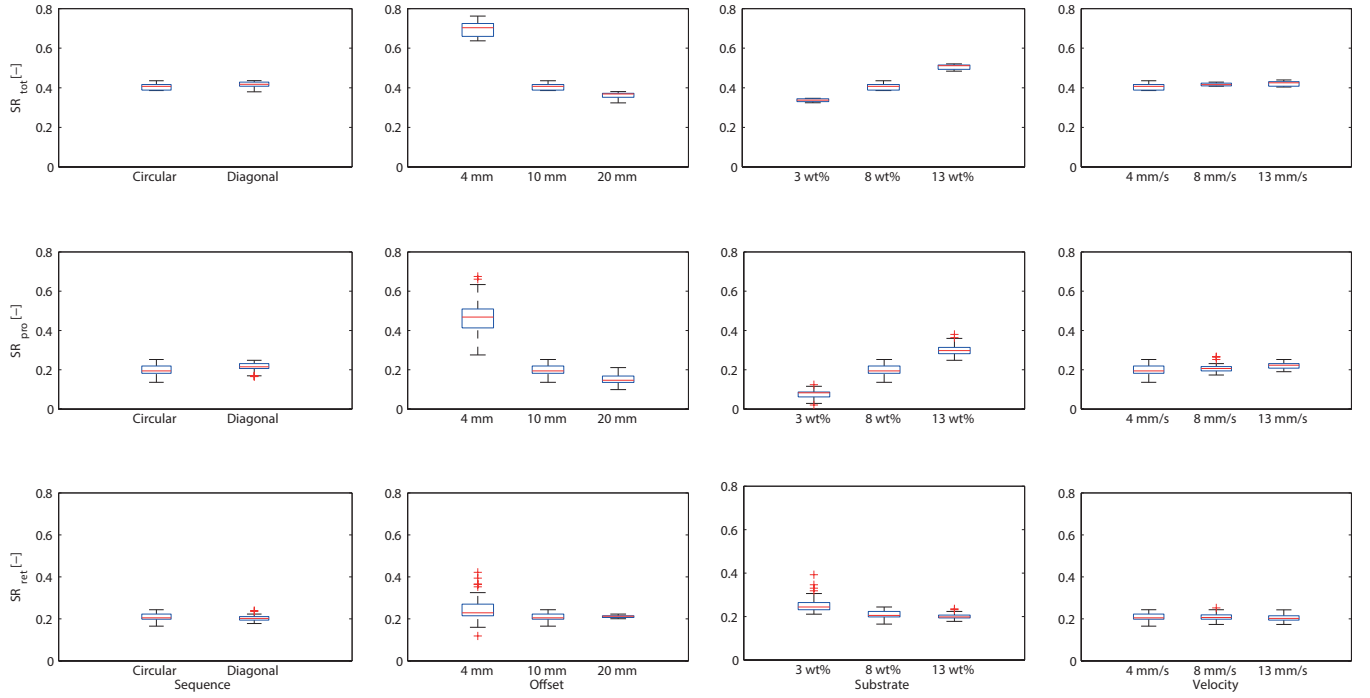


Fig. 13: Prototype experiment. Slip ratio as a function of each of the independent variables (from left to right: sequence, offset, gelatin concentration, and velocity) (top-row) SR_{tot} ; (middle-row) in the protrusion phase (SR_{pro}); and (bottom-row) in the retraction phase (SR_{ret})

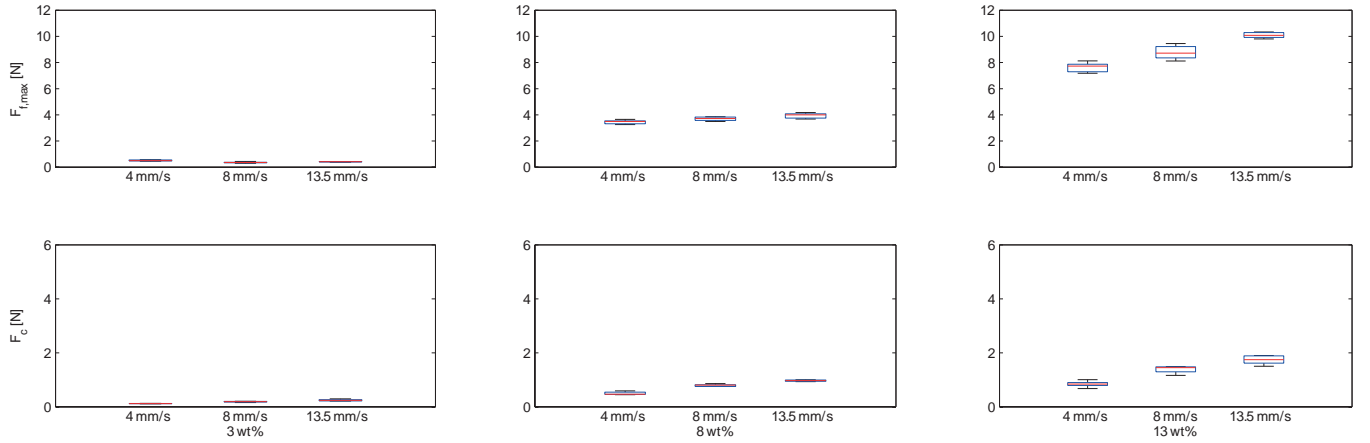


Fig. 14: Force experiment. Axial forces acting on the needle when inserting the needle assembly as a whole. Maximum retraction force (top-row) and the average cutting force (bottom-row) at 4, 8 and 13.5 mm/s in 3, 8 and 13 wt% gelatin concentration.

between friction force and cutting force along the depth of penetration as a function of needle velocity and gelatin concentration. The results show that friction force on the needle increases with velocity, gelatin concentration and penetration depth, whereas the cutting force increases with velocity and gelatin concentration and remains approximately constant along the penetration depth (Figure 14). The relation between friction force and cutting force as described by Equation 1

shows that the friction force becomes dominant over the cutting force at a lower depth of penetration for increasing gelatin concentration and decreasing needle velocity (Table III). As friction force must be higher than cutting force for zero net push force penetration the present findings contradict our hypothesis of a proportional relation between needle velocity and slip, and of an inversely proportional behavior between gelatin concentration and slip.

A. Gelatin concentration

The proportional relation between SR_{tot} and gelatin concentration as depicted in Figure 13 is not in line with our hypothesis and Equation 1. No optimum in gelatin concentration leading to the best performance (lowest SR_{tot}) is found. Furthermore, an inversely proportional relation between gelatin concentration and depth of equilibrium was found in the force experiment, corroborating the absence of an optimum in gelatin concentration (Table III). An optimum below the tested range of 3-13 wt% gelatin concentration cannot be ruled out.

The proportional relation between SR_{tot} and gelatin concentration is in line with Parittotokkaporn et al. (2009) who reported substrate traversal with slip on a 6 wt% gelatin sample and no substrate traversal at all on a 8 wt% gelatin sample¹. Analysis of the slip ratio for the protrusion and retraction phases separately (SR_{pro} and SR_{ret}) revealed that the proportional relation between SR_{tot} and gelatin concentration can be traced back in the protrusion phase only (Figure 13). The amount of slip *per cycle* ($Slip_{pro}$ and $Slip_{ret}$) is approximately constant over the depth of penetration, indicating that $Slip_{pro}$ in the protrusion phase is likely to be caused by a factor which is independent from the depth of penetration (Figure 11).

A parameter that may be contributing to the proportional relation between SR_{tot} and gelatin concentration is the elastic deformation of the gelatine (Figure 15). The proportional relation between friction force and penetration depth as found in the force experiment means that the amount of friction force per unit length is constant over the penetration depth. Figure 12b shows that elastic deformation of the substrate precedes plastic deformation (i.e., substrate traversal) in the protrusion phase, and needle-part protrusion therefore results in partly elastic deformation of the substrate and partly actual substrate traversal. When all four needle parts are protruded, the cart moves slightly backwards due to the (elastically deformed) gelatin springing back. The amount of elastic deformation that prevents actual substrate traversal increases the measured $Slip_{pro}$. It could be that this effect increases with gelatin concentration due to varying elastic properties. Zhang et al. (2011) shows that elasticity increases linearly with gelatin concentration, whereas according to Lorenzo (2012) the slope of the needle friction-depth diagram increases with gelatin concentration, indicating the possibility that friction force increases with gelatin concentration more than elasticity does, therefore contributing to the increasing SR_{tot} for increasing gelatin concentrations. Further research into the relation between friction force and substrate elasticity should give insight into the magnitude of this effect, as this could be incremental after all.

Apart from elasticity, the viscosity of the gelatin may also mediate the proportional relation between gelatin concentration and SR_{tot} . Zhang et al. (2011) shows that viscosity increases with gelatin concentration (also mentioned by Crouch et al.,

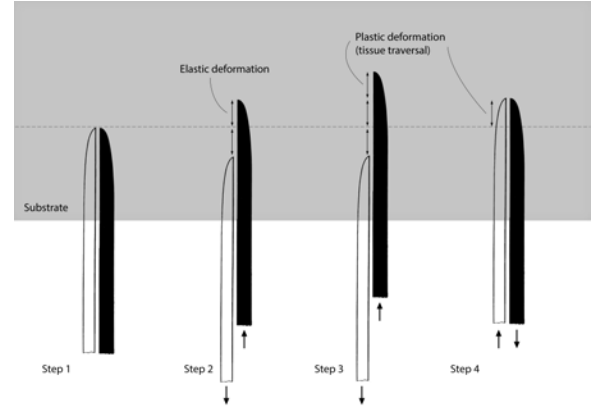


Fig. 15: Possible effect of substrate elasticity on the $Slip_{pro}$. While a needle part protrudes, the amount of protrusion results in partly elastic and partly plastic deformation (tear) of the substrate. When all four needle parts are protruded, the cart moves slightly backwards due to the remaining elastic forces on the protruded needle parts.

2005), suggesting a lower resistance against protrusion in lower concentration gelatin which results in lower $Slip_{pro}$.

It is unlikely that $Slip_{pro}$ is fully defined by elastic deformation and viscosity effects; cart inertia and bearing friction possibly also contribute to the proportional relation between gelatin concentration and SR_{tot} . The resistance against movement of the cart acts as a push force on the protruding needle-part, preventing the cart from moving backwards (i.e., suppressing $Slip_{pro}$). Cutting force increases with gelatin concentration (in line with Wei Ng et al. 2013; Delorenzo 2012; van Gerwen 2012) leaving to believe that cart inertia and bearing friction have less influence on $Slip_{pro}$ in higher gelatin concentrations.

B. Offset

Although the absolute amount of slip *per cycle* (i.e., $Slip_{pro}$ and $Slip_{ret}$) is proportional to the offset and therefore corresponds to our hypothesis (Figure 16), slip decreases with offset meaning that the best *overall* performance is achieved with the largest offset (Figure 13). The elastic deformation as depicted in Figure 15 could contribute to the relatively high SR_{tot} for small offsets. As the absolute effect of elasticity should be equal for the three offsets, the relative contribution to the SR_{pro} is higher for small offsets. This is supported by an exploratory test with an offset of 1 mm, which resulted in no penetration at all, possibly because in that case only elastic deformation was achieved.

The protrusion sections of Figure 11 show that the stationary needle parts slip during the entire protrusion phase. As a possible effect of elasticity is expected to lead to an equal amount of $Slip_{pro}$ and $Slip_{ret}$ for the three offsets, this suggests that another factor induces the proportional behavior between offset and $Slip_{pro}$, $Slip_{ret}$.

¹Parittotokkaporn et al. (2009) mentions gelatin concentrations of 60 and 80 wt%, but these are likely typographic errors meant to be 6 and 8 wt%, respectively (personal communications with Dr. M. Oldfield, Imperial College London).

The proportional relation between needle velocity and friction force, as displayed in Figure 14, indicates that friction force on the protruding needle part is relatively high as compared to the friction force on the stationary needle parts. Since friction force increases with velocity, it is likely that the substrate traversal velocity of the stationary needle parts increases to keep the resistive forces on the protruding needle part and the friction force on the stationary needle parts in equilibrium. Substrate viscosity probably causes the friction force to increase with velocity causing the equilibrium to settle with slipping stationary needle parts (i.e., increasing $Slip_{pro}$). Further investigation into the correlation between material properties of gelatin and needle-substrate interaction is required.

C. Sequence

The size of the surface area subjected to resistive forces during the protrusion phase is the same, independently from the order in which the needle parts are actuated and protruded in the gelatin, resulting in no significant performance difference between one-by-one circular and diagonal actuation. Two-by-two actuation yields no penetration at a velocity of 4 mm/s. This slip ratio of 1 is observed in the protrusion phase as well as in the retraction phase, suggesting that the difference in friction between protruding needle part and stationary needle parts due to difference in the amount of surface area subjected to needle/substrate friction is the dominant factor for successful penetration with this prototype.

Two-by-two actuation at 13.5 mm/s results in penetration with a slip ratio >0.9 . Inertia of the cart must be responsible for the penetration observed in this case. It is likely that the prototype is able to penetrate the substrate when the actuation velocity is high because the protruding needle part accelerates faster forwards than the cart is able to accelerate backwards due to the relatively large mass of the latter. The maximum acceleration in the 13.5-mm/s velocity setting as compared to the 4-mm/s velocity setting is higher by a factor 30. The magnitude of the effect of cart inertia on slip is discussed later in this section.

D. Velocity

No slip reduction has been witnessed for increasing needle-part velocity, contradicting our hypothesis. Force measurements indicate that the cutting force increases more steeply with needle velocity than the friction force does (Table III), contradicting the conclusion of van Gerwen (2007). The difference in maximum acceleration for the different velocity settings in the prototype experiment makes the validation of the performance results difficult. Future experiments with varying velocity require a thought-out trade-off between maximum acceleration and acceleration time to reach a certain needle-part velocity. A reduction of acceleration would result in a longer acceleration time introducing difficulties in comparing results from different velocity settings, whereas a high acceleration difference between velocity settings make comparison of results difficult due to the effect of inertia.

E. Limitations

Cart inertia and bearing friction pose resistance against cart movement, possibly preventing slip from occurring in the protrusion phase when the resultant force on the cart is directed out of the substrate. The direction of the resistive forces on the protruding needle part is opposite to the direction of the friction force on the three stationary needle parts. As a result, the resultant force acting on the needle in the protrusion phase is likely to be lower than the resultant force acting on the needle during the retraction phase. Therefore, the resistance against movement of the cart is of less influence in the retraction phase. In other words, inertia has most influence in the protrusion phase where it decreases the amount of $Slip_{pro}$.

The cart weights 0.73 Kg and accelerates with a maximum of 27 mm/s^2 in the 4-mm/s velocity setting, as can be seen in Figure 17. Acceleration of the cart therefore requires a force of about 0.02 N. To also overcome the bearing friction, an additional force of about 0.015 N is needed (assuming a friction coefficient of 0.002 for lubricated ball bearings; van Beek, 2006). Thus, in the protrusion phase, when resultant axial forces on the needle are likely to be lower than 0.035 N, an effect of inertia and friction cannot be ruled out. The contradiction between the slip results of the prototype experiment and force experiment is possibly caused by the influence of the cart inertia and bearing friction. On the other hand, resistive forces during the successful penetration of the needle at 4 mm/s can reach up to 10 N (Figure 14) whereas the prototype is only able to deliver a net push force of 0.035 N, therefore net axial push force on the multipart needle is significantly reduced as compared to a single part needle and independent from the needle depth.

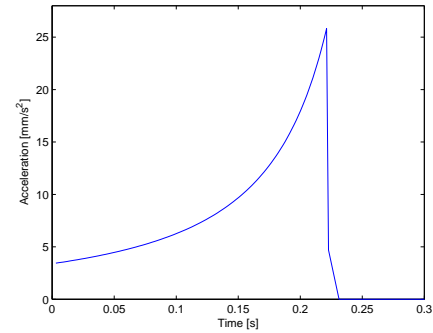


Fig. 17: Graph showing the acceleration profile corresponding to the motion of the needle parts in the protrusion and retraction phase of the 4 mm/s velocity setting . Peak acceleration equals 27-mm/s^2

Validation of the method of friction and cutting force determination (also used by Hing, 2006 and Simone and Okamura, 2002) was done by looking at the decrease of the maximum friction force over a supplementary series of measurements in the same hole. Results show that the estimate of the friction force is too low and therefore the estimate of the cutting force is too high, due to the fact that the retraction force is

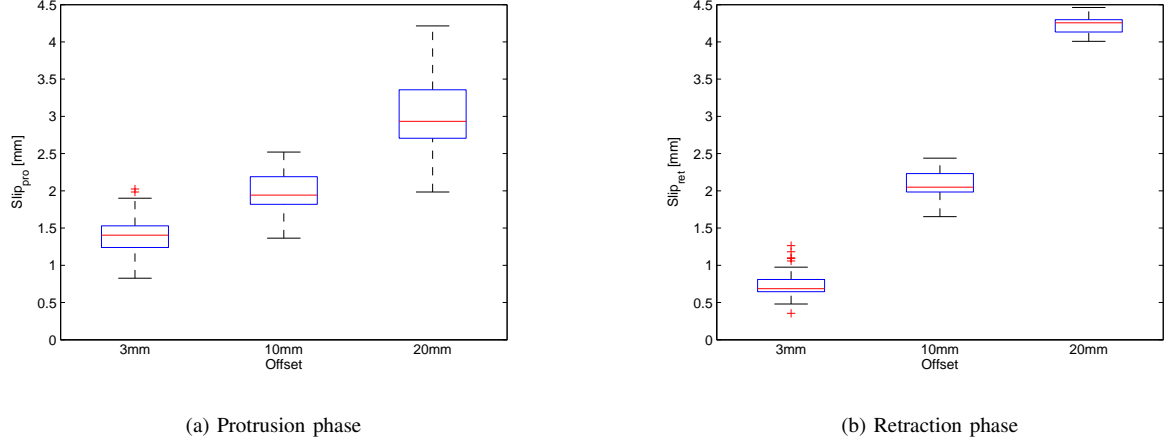


Fig. 16: Absolute amount of slip for varying offsets in the protrusion (a) and the retraction (b) phase.

measured after the hole is already made during the insertion movement of the needle. The supplementary measurements have been conducted in the 3, 8 and 13 wt% gelatin samples. The entire needle was inserted 5 times in the same hole, the retraction force is displayed in Figure 18. All three substrates show a decline in retraction force after the first insertion. The retraction force is taken as an estimate for the friction force. The difference in maximum retraction force between the first insertion creating the hole and the subsequent insertions in this hole is approximately 10% (Table IV). We estimate that the qualitative relations found between cutting/friction force and needle velocity/substrate concentration in the force experiment are not affected by the estimation error of the cutting and friction force.

TABLE IV: Maximum axial force of 6 retraction movements in the same hole, normalized on the maximum friction force of the first retraction movement.

| Insertion number | Retraction force [-] | | |
|------------------|----------------------|--------|--------|
| | 3wt% | 8wt% | 13wt% |
| 1 | 1 | 1 | 1 |
| 2 | 0.8887 | 0.896 | 0.8912 |
| 3 | 0.9081 | 0.8442 | 0.8461 |
| 4 | 0.8804 | 0.8949 | 0.8492 |
| 5 | 0.8743 | 0.8889 | 0.8548 |
| 6 | 0.8221 | 0.893 | 0.8773 |

No interconnection between the needle parts was incorporated in the needle prototype. Despite the inward directed bevel angle on the tip of the needle the needle parts separated during the prototype experiment. Separation became visible at a penetration depth of approximately 8 cm. Since the amount of SR_{pro} and SR_{ret} remain constant over the depth of penetration it is likely that the separation of needle parts does not affect the relation between friction force and cutting force on the needle parts severely. Nevertheless, an interconnection is required for a steerable four-part needle for making use

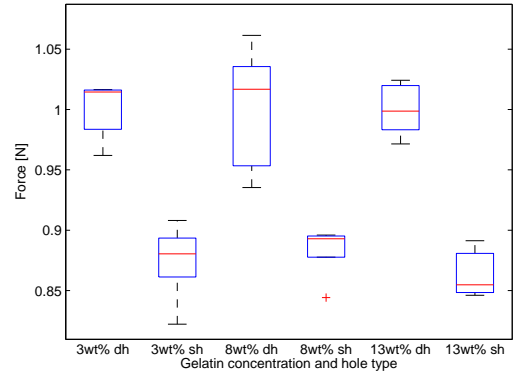


Fig. 18: Maximum axial force in the retraction movement of the needle. For each gelatin concentration the results of 5 insertions in a different hole (dh) are compared with 5 insertions in the same hole (sh). The force is normalized by dividing the measured retraction force with the the mean maximum retraction force of the 5 first time insertions.

of the principle of zero net push force penetration to prevent buckling of needle parts inside the substrate (Figure 2).

F. Future work

In this work, we only focused on straight trajectories. Frasson et al. (2011) shows that steering with a multipart needle can be done by using the multipart needle's ability to change the bevel angle of the tip by controlling the relative offset between needle parts (Figure 1f). Asymmetric forces acting from the substrate on the beveled tip cause the needle to cut a curved trajectory. On the other hand, wasps have shown that they are capable of bending their ovipositors in

several ways described by Quicke (1991), Quicke et al. (1995) and Quicke and Fitton (1995) (Figure 5). Further research is required to find the most suitable way of steering a multipart needle.

Needle buckling causing lateral slicing of the substrate during penetration as described by Kyle et al. (2011; Figure 2) can possibly be solved by using a needle that is able to penetrate without the application of a net push force. A reciprocally moving multipart needle may be a solution, as it makes the push force required for the insertion of a multipart needle independent of the penetration depth. An equivalent to the wasps ovipositor olishteter mechanism is required to keep the needle parts together during penetration when cutting curved trajectories, to prevent buckling of the protruding needle-part inside the substrate. Future research into the behavior of a steerable multipart needle should quantify its capabilities of cutting curved trajectories while preventing needle buckling in soft tissues in comparison to current steerable needles.

The experiment in which the effect of offset, gelatin concentration, sequence and velocity on the performance of the multipart needle is investigated could possibly be improved by reducing the effect of cart inertia and bearing friction either by compensating or modeling the effect of inertia and friction or by reducing the weight and friction of the setup. Insight into how the substrate elasticity may affect $Slip_{pro}$ can possibly be obtained by investigating the needle-substrate interaction in close-up to distinguish elastic deformation from actual substrate traversal during the insertion of the needle.

Integration of the force experiment with the prototype experiment to create the possibility to measure the axial force on the needle parts individually could contribute to a better understanding of the force equilibrium between friction force and cutting force on the needle parts during penetration.

VII. CONCLUSION

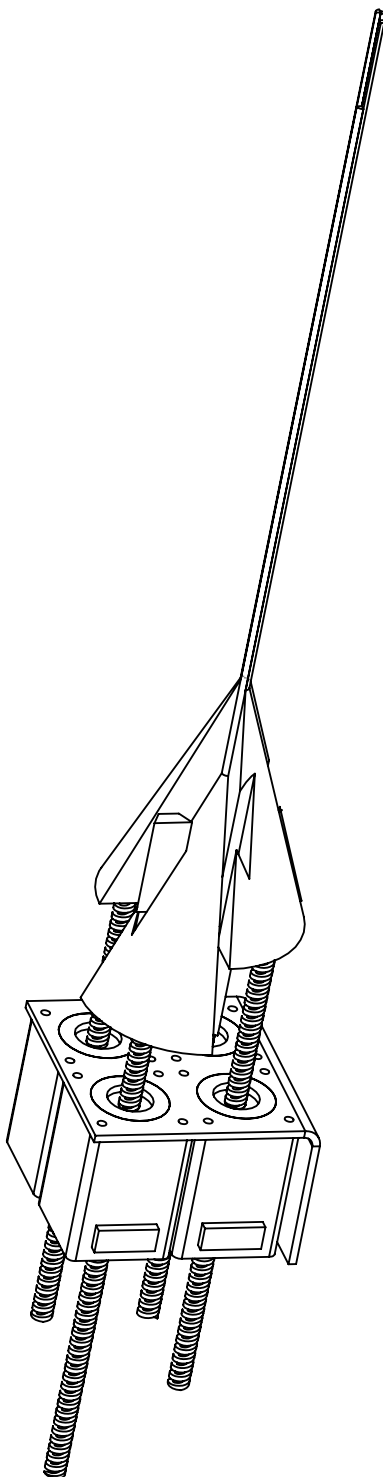
Penetration of 3, 8 and 13 wt% porcine gelatin is achieved with a maximum push force of approximately 0.035 N, independent from the depth of penetration. This is achieved using a friction difference induced between protruding needle parts and stationary needle parts solely based on the difference in surface area subjected to needle-tissue friction. An inversely proportional relation between gelatin concentration and slip ratio and a proportional relation between offset and slip ratio were found. No significant effect of sequence variation and velocity variation is found. Validation of these relations and comparison with force measurements is found difficult due to the effect of cart inertia and bearing friction on the measured slip.

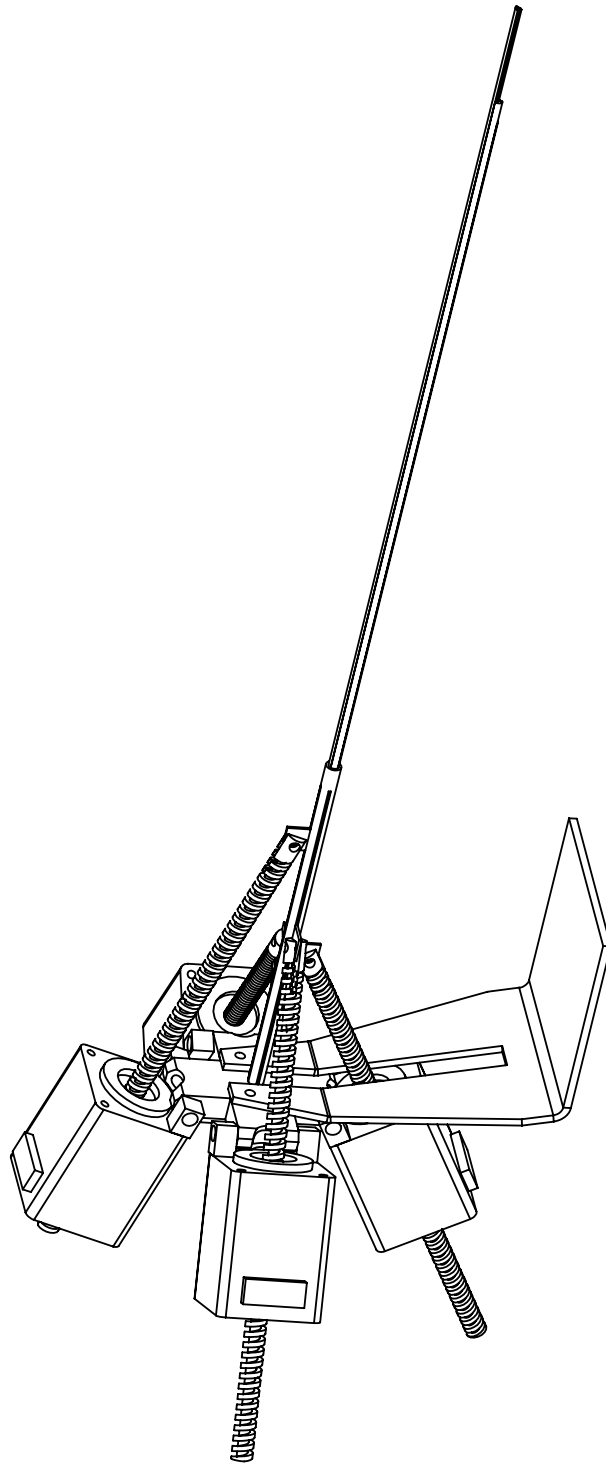
REFERENCES

- [1] Abolhassani, N., Patel, R., & Moallem, M. (2007). Needle insertion into soft tissue: A survey. *Medical Engineering & Physics*, 29(4), 413-431.
- [2] Burrows, C., Secoli, R., & Rodriguez y Baena, F. (2013). Experimental characterisation of a biologically inspired 3D steering needle. *IEEE International Conference on Control, Automation and Systems (ICCAS)*, 2013 13th, pp. 1252-1257.
- [3] Cowan, N. J., Goldberg, K., Chirikjian, G. S., Fichtinger, G., Alterovitz, R., Reed, K. B., ... & Okamura, A. M. (2011). Robotic needle steering: Design, modeling, planning, and image guidance. *In Surgical Robotics*, pp. 557-582.
- [4] Crouch, J. R., Schneider, C. M., Wainer, J., & Okamura, A. M. (2005). A velocity-dependent model for needle insertion in soft tissue. *In Medical Image Computing and Computer-Assisted Intervention (Miccai 2005)*, pp. 624-632.
- [5] De Lorenzo, D. (2012). *Force sensing and display in robotic driven needles for minimally invasive surgery*.
- [6] Elias, L. G., Teixeira, S. P., Kjellberg, F., & Pereira, R. A. S. (2012). Diversification in the use of resources by Idarnes species: bypassing functional constraints in the fig-fig wasp interaction. *Biological Journal of the Linnean Society*, 106(1), 114-122.
- [7] Engh, J. A., Podnar, G., Khoo, S. Y., & Riviere, C. N. (2006). Flexible needle steering system for percutaneous access to deep zones of the brain. *Proceedings of the IEEE 32nd Annual Northeast Conference on Bioengineering*, 2006, pp. 103-104.
- [8] Frasson, L., Parittotokkaporn, T., Schneider, A., Davies, B. L., Vincent, J. F. V., Huq, S. E., ... & y Baena, F. R. (2008). Biologically inspired microtexturing: Investigation into the surface topography of next-generation neurosurgical probes. *IEEE 30th Annual International Conference of the Engineering in Medicine and Biology Society (EMBS 2008)*, 2008, pp. 5611-5614.
- [9] Frasson, L., Ko, S. Y., Turner, A., Parittotokkaporn, T., Vincent, J. F., & y Baena, F. R. (2010). STING: a soft-tissue intervention and neurosurgical guide to access deep brain lesions through curved trajectories. *Proceedings of the Institution of Mechanical Engineers, Part H: Journal of Engineering in Medicine*, 224(6), 775-788.
- [10] Frasson, L., Parittotokkaporn, T., Davies, B. L., & y Baena, F. R. (2010). Early developments of a novel smart actuator inspired by nature. *International Journal of Intelligent Systems Technologies and Applications*, 8(1), 409-422.
- [11] Frasson, L., Ferroni, F., Ko, S. Y., Dogangil, G., & y Baena, F. R. (2012). Experimental evaluation of a novel steerable probe with a programmable bevel tip inspired by nature. *Journal of Robotic Surgery*, 6(3), 189-197.
- [12] Furusho, J., Katsuragi, T., Kikuchi, T., Suzuki, T., Tanaka, H., Chiba, Y., & Horio, H. (2006). Curved multi-tube systems for fetal blood sampling and treatments of organs like brain and breast. *Surgical Robotics and Instrumentation. International Journal of Computer Assisted Radiology and Surgery*, 1, 224-226.
- [13] Glozman, D., & Shoham, M. (2007). Image-guided robotic flexible needle steering. *IEEE Transactions on Robotics*, 23(3), 459-467.
- [14] Grady, R. E., Horlocker, T. T., Brown, R. D., Maxson, P. M., & Schroeder, D. R. (1999). Neurologic complications after placement of cerebrospinal fluid drainage catheters and needles in anesthetized patients: implications for regional anesthesia. *Anesthesia & Analgesia*, 88(2), 388-392.
- [15] Hing, J. T., Brooks, A. D., & Desai, J. P. (2006). Reality-based needle insertion simulation for haptic feedback in prostate brachytherapy. *Proceedings of the IEEE International Conference on Robotics and Automation (ICRA 2006)*, 2006, pp. 619-624.
- [16] Le Lannic, J., & Nenon, J. P. (1999). Functional morphology of the ovipositor in *Megarhyssa atrata* (Hymenoptera, Ichneumonidae) and its penetration into wood. *Zoomorphology*, 119(2), 73-79.
- [17] Leibinger, A., Oldfield, M., & y Baena, F. R. (2014). Multi-objective design optimization for a steerable needle for soft tissue surgery. *In The 15th International Conference on Biomedical Engineering*, pp. 420-423.
- [18] McGill, C. S., Schwartz, J. A., Moore, J. Z., McLaughlin, P. W., & Shih, A. J. (2011). Precision grid and hand motion for accurate needle insertion in brachytherapy. *Medical Physics*, 38(8), 4749-4759.
- [19] Misra, S., Reed, K. B., Schafer, B. W., Ramesh, K. T., & Okamura, A. M. (2009). Observations and models for needle-tissue interactions. *IEEE International Conference on Robotics and Automation (ICRA'09)*, pp. 2687-2692.

- [20] Ng, K. W., Goh, J. Q., Foo, S. L., Ting, P. H., & Lee, T. K. (2013). Needle Insertion Forces Studies for Optimal Surgical Modeling. *International Journal of Bioscience, Biochemistry and Bioinformatics*, Vol. 3 (3).
- [21] Okazawa, S., Ebrahimi, R., Chuang, J., Salcudean, S. E., & Rohling, R. (2005). Hand-held steerable needle device. *IEEE/ASME Transactions on Mechatronics*, 10(3), 285-296.
- [22] Oldfield, M. J., Burrows, C., Kerl, J., Frasson, L., Parittotokkaporn, T., Beyrau, F., & y Baena, F. R. (2014). Highly resolved strain imaging during needle insertion: Results with a novel biologically inspired device. *Journal of the Mechanical Behavior of Biomedical Materials*, 30, 50-60.
- [23] Parittotokkaporn, T., Frasson, L., Schneider, A., Huq, S. E., Davies, B. L., Degenaar, P., ... & y Baena, F. R. (2009). Soft tissue traversal with zero net push force: feasibility study of a biologically inspired design based on reciprocal motion. *IEEE International Conference on Robotics and Biomimetics*, 2008. (ROBIO 2008), pp. 80-85.
- [24] Quicke, D. L., & Fitton, M. G. (1995). Ovipositor steering mechanisms in parasitic wasps of the families Gasteruptiidae and Aulacidae (Hymenoptera). *Proceedings of the Royal Society of London. Series B: Biological Sciences*, 261(1360), 99-103.
- [25] Quicke, D. L. (1991). Ovipositor mechanics of the braconine wasp genus Zaglyptogastra and the ichneumonid genus Pristomerus. *Journal of Natural History*, 25(4), 971-977.
- [26] Quicke, D. L., Fitton, M. G. & Harris, J. (1995). Ovipositor Steering Mechanisms in Braconid Wasps. *Journal of Hymenoptera Research*, Vol. 4, pp. 110-120.
- [27] Rahman, M. H., Fitton, M. G., & Quicke, D. L. (1998). Ovipositor internal microsculpture in the Braconidae (Insecta, Hymenoptera). *Zoologica Scripta*, 27(4), 319-332.
- [28] Reed, K. B., Majewicz, A., Kallem, V., Alterovitz, R., Goldberg, K., Cowan, N. J., & Okamura, A. M. (2011). Robot-assisted needle steering. *IEEE Robotics & Automation Magazine*, 18(4), 35-46.
- [29] Scudder, G. G. E. (1971). Comparative morphology of insect genitalia. *Annual Review of Entomology*, 16(1), 379-406.
- [30] Sears, P., & Dupont, P. (2006). A steerable needle technology using curved concentric tubes. *IEEE/RSJ International Conference on Intelligent Robots and Systems 2006*, pp. 2850-2856.
- [31] Syringe Needle Gauge Chart (2014). Retrieved from <http://www.sigmaaldrich.com/chemistry/stockroom-reagents/learning-center/technical-library/needle-gauge-chart.html>
- [32] Simone, C., & Okamura, A. M. (2002). Modeling of needle insertion forces for robot-assisted percutaneous therapy. *IEEE Proceedings of the International Conference on Robotics and Automation (ICRA'02)*, 2002, Vol. 2, pp. 2085-2091.
- [33] Van Beek, A. (2006). Advanced engineering design: lifetime performance and reliability (Vol. 1).
- [34] van Gerwen, D. J., Dankelman, J., & van den Dobbelsteen, J. J. (2012). Needle-tissue interaction forces-A survey of experimental data. *Medical Engineering & Physics*, 34(6), 665-680.
- [35] Vincent, J. F. V., King, M. J. (1995). The mechanism of drilling by wood wasp ovipositors. *Biomimetics*, Vol. 3(4).
- [36] Walsh, C. J., Franklin, J. C., Slocum, A. & Gupta, R. (2010). Material selection and force requirements for the use of pre curved needles in distal tip manipulation mechanisms. *Proceedings of the Design of Medical Devices Conference (DMD 2010)*, 3913.
- [37] Wan, G., Wei, Z., Gardi, L., Downey, D. B., & Fenster, A. (2005). Brachytherapy needle deflection evaluation and correction. *Medical Physics*, 32(4), 902-909.
- [38] Webster, R. J., Memisevic, J., & Okamura, A. M. (2005). Design considerations for robotic needle steering. *Proceedings of the 2005 IEEE International Conference on Robotics and Automation (ICRA 2005)*, 2005, pp. 3588-3594.
- [39] Webster, R. J., Okamura, A. M., & Cowan, N. J. (2006). Toward active cannulas: Miniature snake-like surgical robots. *IEEE/RSJ International Conference on Intelligent Robots and Systems*, 2006, pp. 2857-2863.
- [40] Webster III, R. J., Swensen, J. P., Romano, J. M., & Cowan, N. J. (2009). Closed-form differential kinematics for concentric-tube continuum robots with application to visual servoing. In *Experimental Robotics*, pp. 485-494.
- [41] Zhang, X., Qiang, B., & Greenleaf, J. (2011). Comparison of the surface wave method and the indentation method for measuring the elasticity of gelatin phantoms of different concentrations. *Ultrasonics*, 51(2), 157-164.

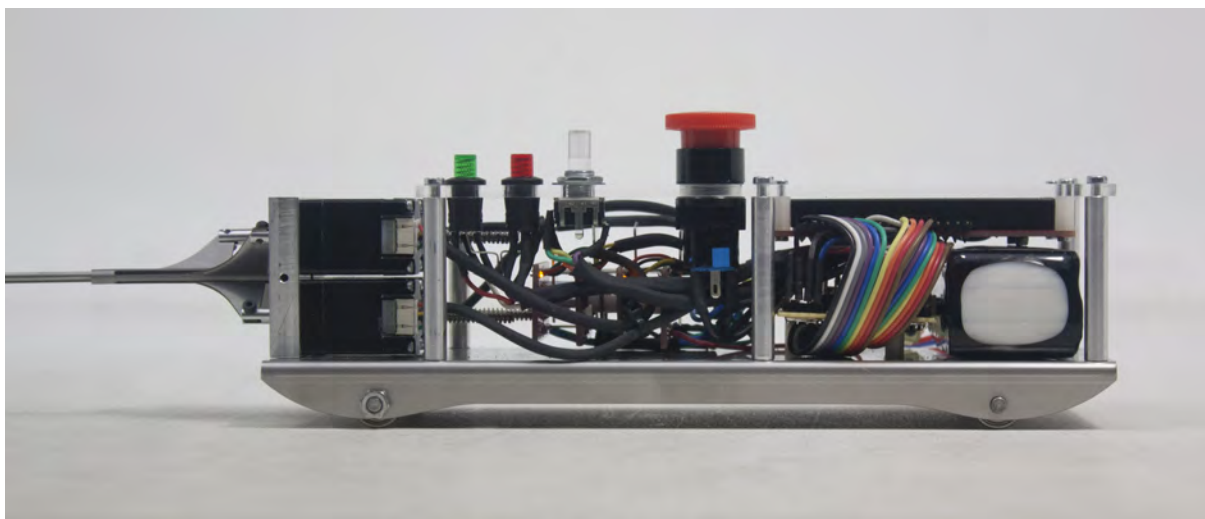
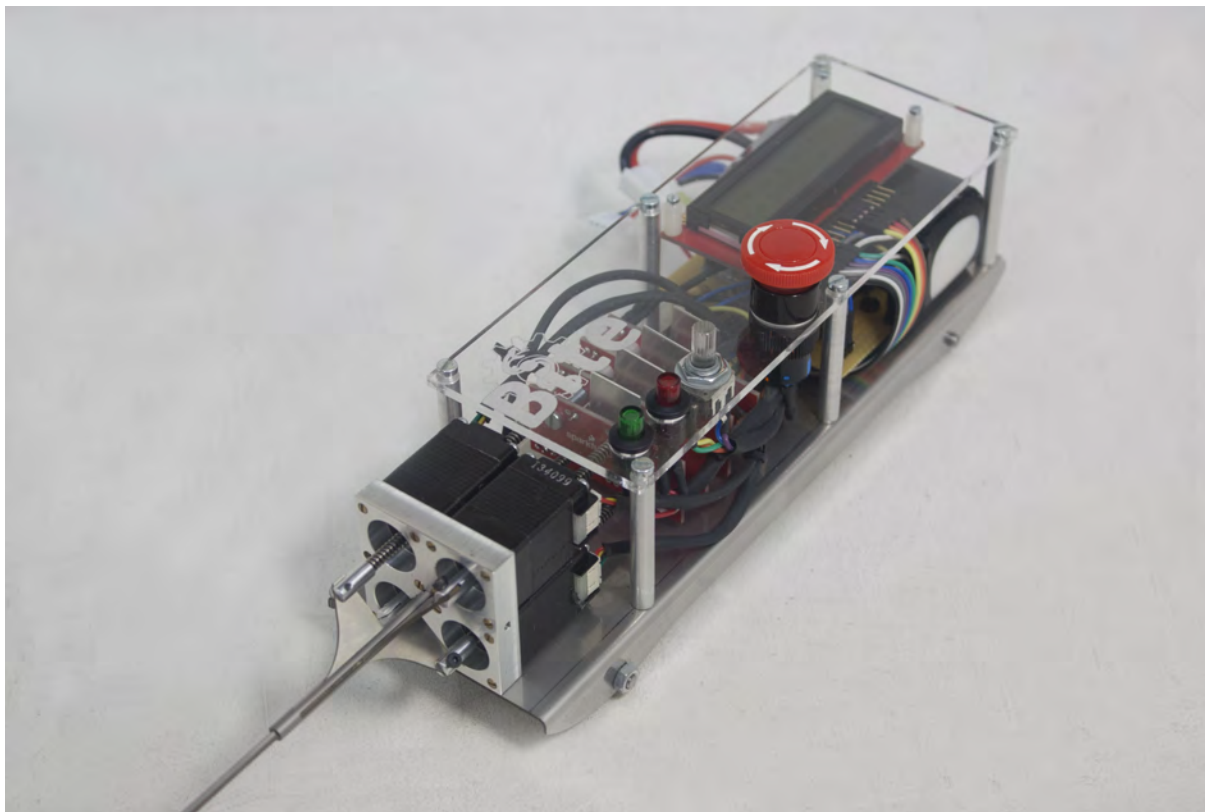
APPENDIX A
ACTUATOR CONFIGURATION CONCEPTS

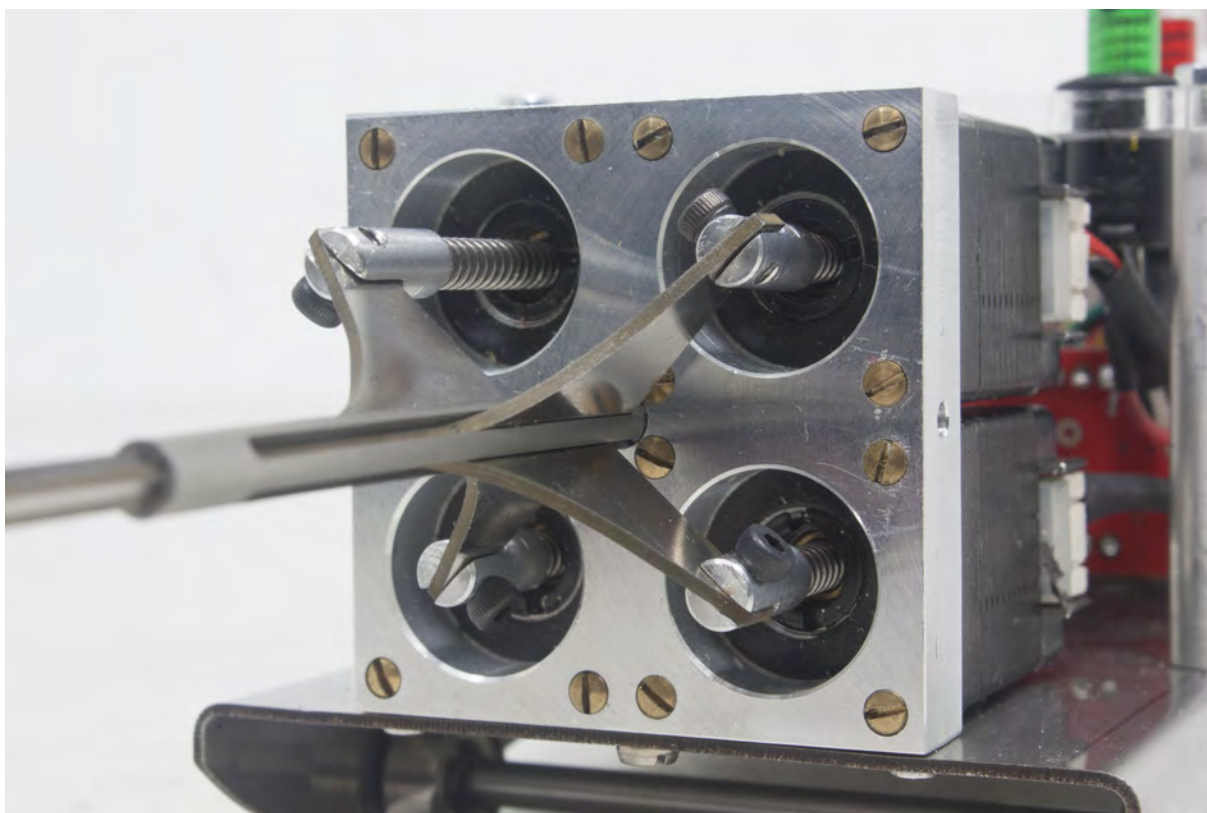
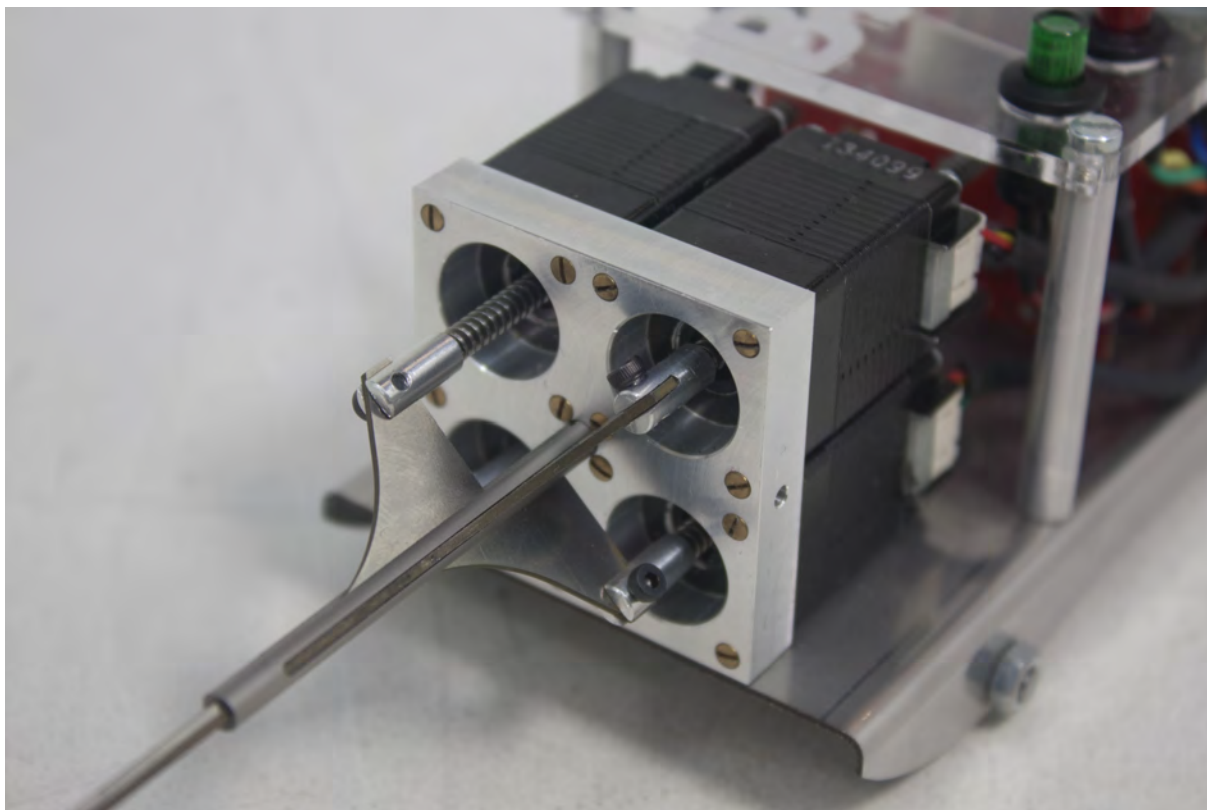




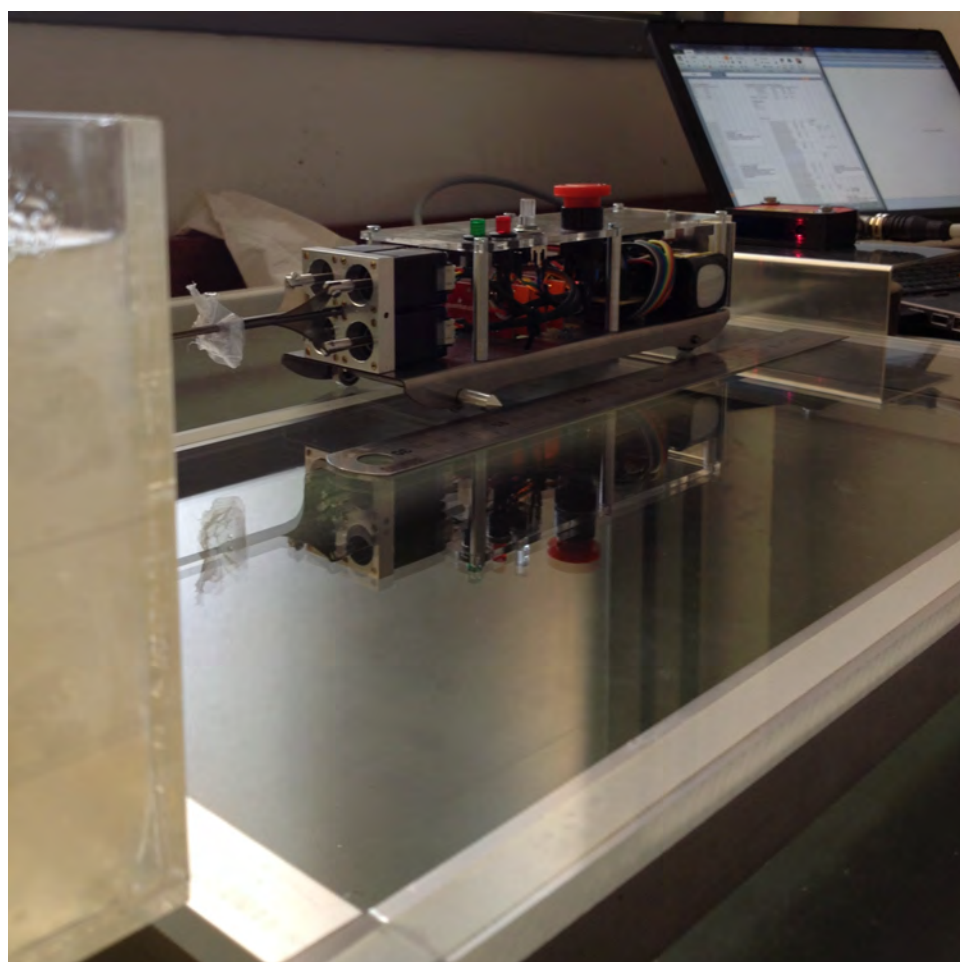
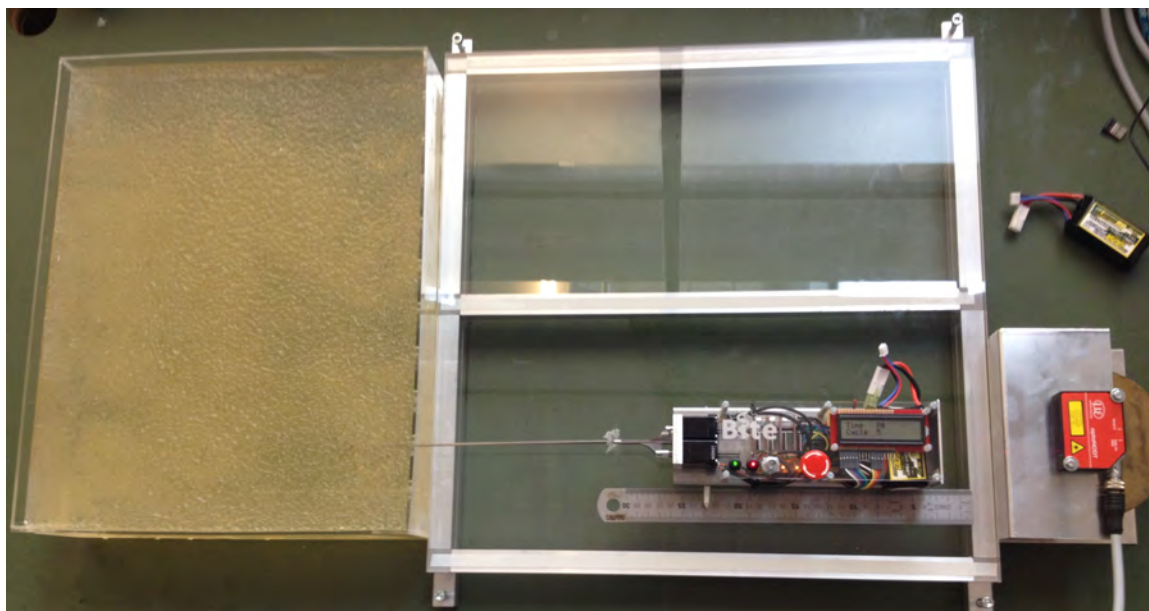
APPENDIX B IMAGES OF THE EXPERIMENTAL SETUP

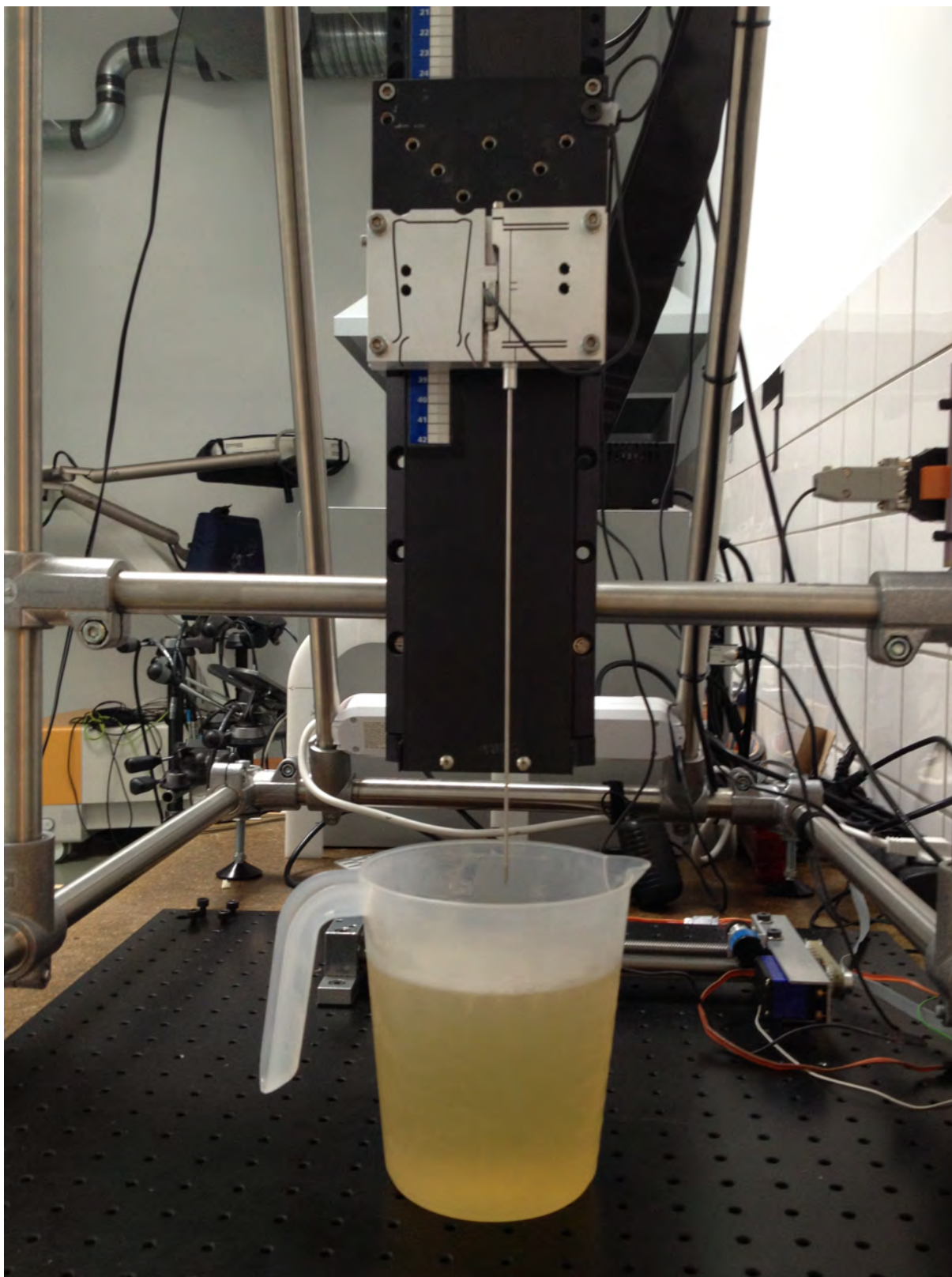
A. *Prototype*



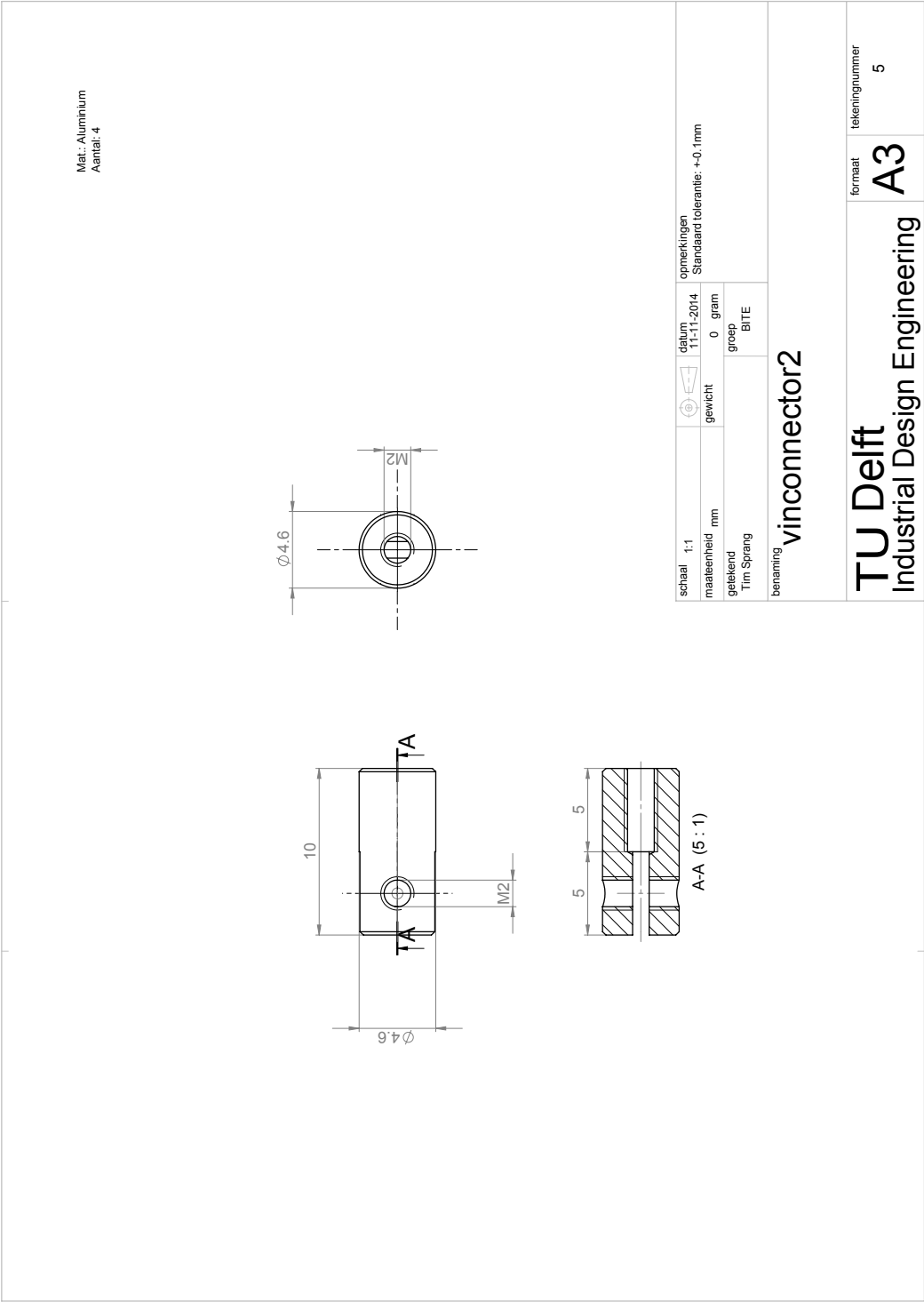


B. Prototype experiment

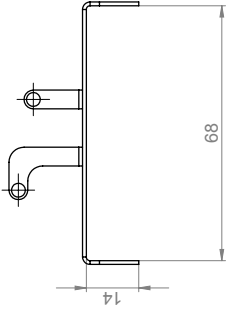
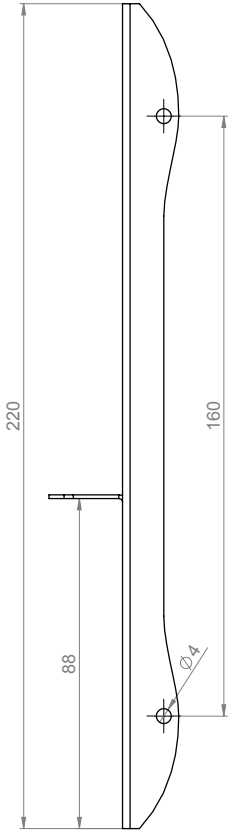



C. Force experiment

APPENDIX C
TECHNICAL DRAWINGS

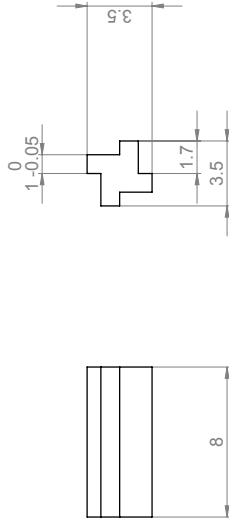



Mat.: RVS
Aantal: 1

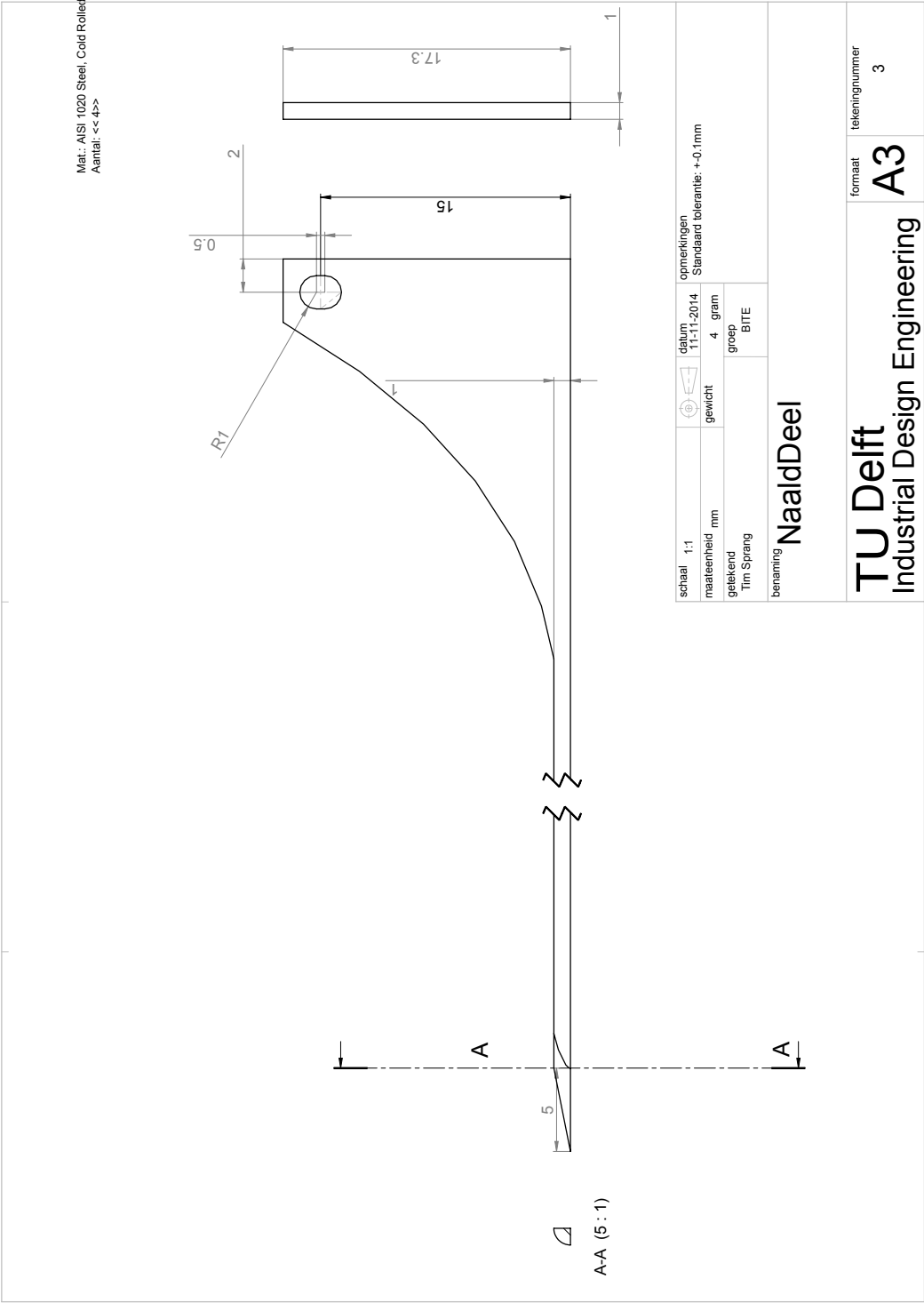


| | | | | |
|-------------------------------|---|------------------|------------------------------|-------------------|
| schaal 1:1 |  | datum 14-11-2014 | opmerkingen | |
| | maat eenheid mm | gewicht 157 gram | Standaard tolerantie: +0.1mm | |
| geleidend | Tim Sprang | groep BITE | | |
| benaming Plateau | | | | |
| TU Delft | | | formaat A3 | tekeningsnummer 6 |
| Industrial Design Engineering | | | | |

Mat.: AISI 304
Aantal: <1 >>



| | | | | |
|---|--|---|---------------------|------------------------------|
| schaal 5:1 | |  | datum 11-11-2014 | opmerkingen |
| maateenheid mm | | gewicht | 0 gram | Standaard tolerantie: +0.1mm |
| getekend Tim Sprang | | groep | BITE | |
| benaming Pin_insert | | | | |
| TU Delft Industrial Design Engineering | | | formaat A3 | tekeningsnummer 4 |



APPENDIX D PROTOTYPE EMBEDDED SOFTWARE

A. Software schematic

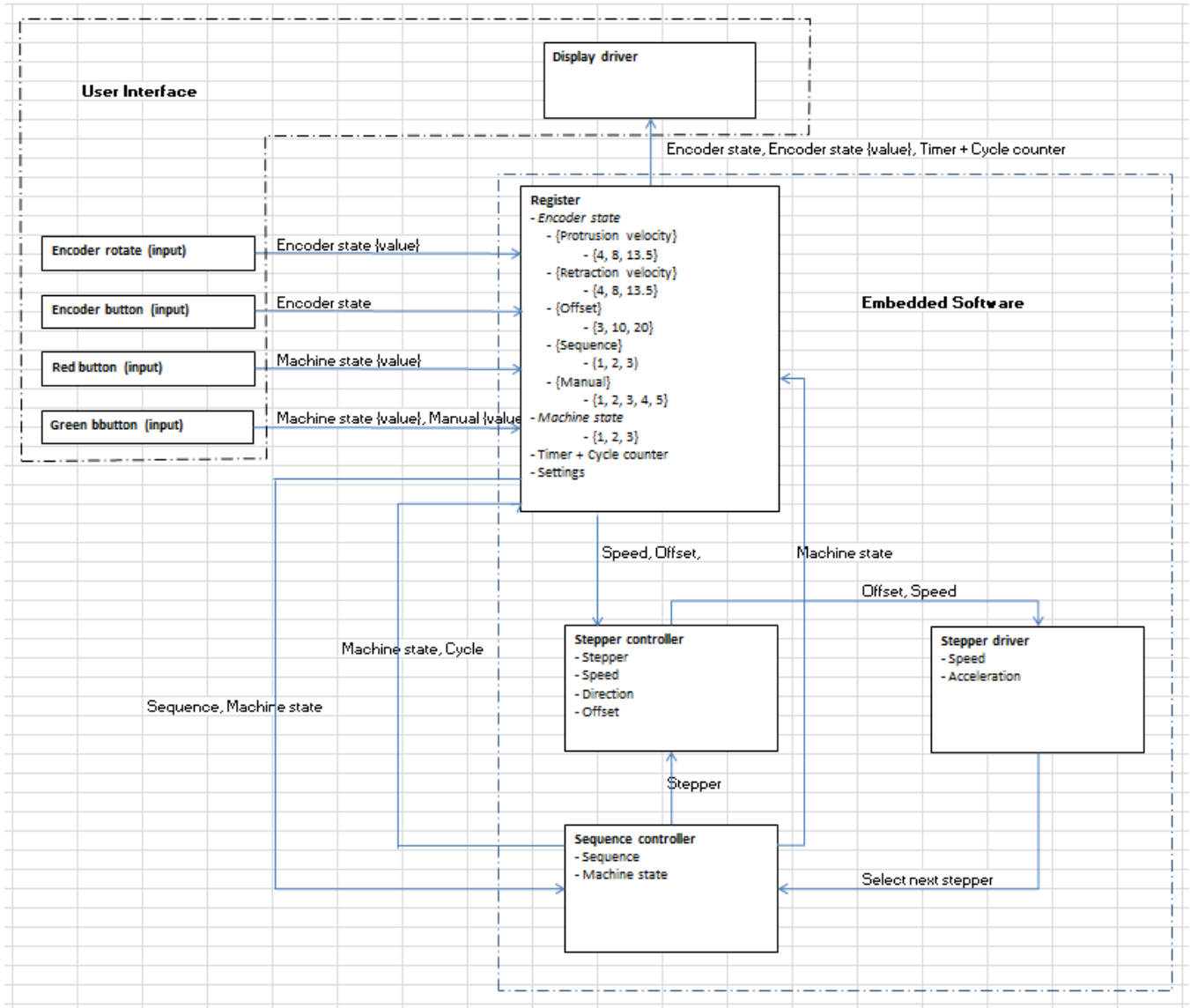


Fig. 19: Software design. The software can be subdivided into an embedded part and a user interface part. The user interface allows for the start and stop of the prototype and the change of offset, velocity and sequence settings. The embedded part regulates the corresponding needle-part actions.

B. Embedded code

```

1 // Bite Needle
2
3 #include <Button.h>
4 #include <LiquidCrystal.h>
5 #include <TimerOne.h>
6
7 #define INIT_TIMER_COUNT 6
8 #define RESET_TIMER2 TCNT2 = INIT_TIMER_COUNT
9
10 /* CONNECTIONS */
11
12 // Stepper connections
13 int stepper1step = 8;
14 int stepper1dir = 4;
15 int stepper2step = 9;
16 int stepper2dir = 5;
17 int stepper3step = 10;
18 int stepper3dir = 6;
19 int stepper4step = 11;
20 int stepper4dir = 7;
21 int stepperEnable = 2;
22
23 // Display connections
24 int RS_pin = A1;
25 int Enable_pin = A0;
26 int D4_pin = A5;
27 int D5_pin = A4;
28 int D6_pin = A3;
29 int D7_pin = A2;
30
31 // Buttons and Encoder connections
32 Button green(12); // Green button signal
33 Button red(13); // Red button signal
34 Button select(3); // Encoder button
35 int encoderPinA = A7; // Encoder right pin
36 int encoderPinB = A6; // Encoder left pin
37
38
39 /* SETTINGS */
40
41 // Time & interrupt settings
42 int timerInterval=15; // interrupt timing in microseconds
43 int stepVelocity;
44 int noStep;
45 int stepDelay = 200;
46 int min_stepDelay;
47 int min_stepDelay_forward[] = {100,45,30};
48 int min_stepDelay_backward[] = {100,45,30};
49 int naaldPos = 0;
50 int motorSelect = 1;
51 int time = 0;
52 int Timer = 0;
53 int cycle = 0;
54 /* INITIATE */
55
56 // Initiate encoder
57 int selected = 0;
58 int encoderPos = 0;
59 int encoderPinALast = LOW;
60 int n = LOW;
61 int selStepStep;
62 long naaldOffset[]={500,1660,3320};
63 int motorSelected = 0;
64 long steps=0;
65 long totSteps;
66 int stepperSequence[][4] = {{1,2,4,3},{1,4,2,3},{6,7,0,0}};
67 boolean stepperDone = true;
68 int stepperSelector = 0;
69 int seqSelect = 1;
70 int offSelect = 2;
71 int delSelect = 1;
72 int selectedStepper;
73 boolean stepperStop = true;
74 int machineState = 2;
75
76
77 LiquidCrystal lcd(RS_pin, Enable_pin, D4_pin, D5_pin, D6_pin, D7_pin);

```

```

78 String memline1;
79 String memline2;
80
81 /* FUNCTIONS */
82 // Update the display
83 void lcdPrint(String line1, String line2) {
84
85     lcd.clear();
86     if (line1 != "") {
87         lcd.setCursor(0,0);
88         lcd.print(line1);
89         memline1 = line1;
90     } else lcd.print(memline1);
91     lcd.setCursor(0,1);
92     if (line2 != "") {
93         lcd.print(line2);
94         memline2 = line2;
95     } else lcd.print(memline2);
96 }
97
98 void selectNextStepper () {
99     if (machineState < 2) {
100         int sequenceLength = 4; //determine length of the sequence of motor actions
101         if (stepperSelector < sequenceLength) {
102             stepper(stepperSequence[seqSelect-1][stepperSelector], naaldOffset[offSelect-1],min_stepDelay_forward[delSelect-1]);
103             stepperSelector++;
104         } else {
105             stepper(5,-naaldOffset[offSelect-1],min_stepDelay_backward[delSelect-1]);
106             stepperSelector = 0;
107             cycle++;
108             if(machineState == 1) machineState = 2;
109         }
110     } else if (machineState == 2) {
111         digitalWrite(stepperEnable, HIGH);
112         machineState = 3;
113     }
114     stepDelay = 200;
115 }
116
117 void stepper(int steppersel, long stepperdis, int stepperVelocity) {
118     totSteps = abs (stepperdis);
119     motorSelected = steppersel;
120     min_stepDelay = stepperVelocity;
121
122     switch (steppersel) {
123     case 0:
124         selStepStep = B00000000;
125         totSteps = 0;
126     case 1:
127         digitalWrite(stepper1dir,(stepperdis > 0) ? HIGH : LOW); // Change motor direction to the desired travel direction
128         // By comparting to this string, the only pin that changes high:low in the interrupt is the one which has a 1 in this string.
129         selStepStep = B00000001;
130         break;
131     case 2:
132         digitalWrite(stepper2dir,(stepperdis > 0) ? HIGH : LOW);
133         selStepStep = B00000010;
134         break;
135     case 3:
136         digitalWrite(stepper3dir,(stepperdis > 0) ? HIGH : LOW);
137         selStepStep = B00000100;
138         break;
139     case 4:
140         digitalWrite(stepper4dir,(stepperdis > 0) ? HIGH : LOW);
141         selStepStep = B00001000;
142         break;
143     case 5:
144         if (stepperdis > 0) PORTD = PORTD | B11110000; //Make sure that all direction pins are high.
145         else PORTD = PORTD & B00001111; //If no distance need to be traveled all direction pins are low.
146         selStepStep = B00001111;
147         break;
148     case 6:
149         if (stepperdis > 0) PORTD = PORTD | B00110000;
150         else PORTD = PORTD & B11001111;
151         selStepStep = B00000011;
152         break;
153     case 7:
154         if (stepperdis > 0) PORTD = PORTD | B11000000;
155         else PORTD = PORTD & B00111111;
156         selStepStep = B00001100;

```

```

157     break;
158 }
159 steps=0;
160 }
161
162
163 //interrupt function
164 void interrupt() {
165     time++;
166     if (steps == totSteps) selectNextStepper();
167     else {
168         if (noStep == stepDelay) {
169             // 8 pulses to make 1 step
170             PORTB = PORTB ^ selStepStep; // set HIGH
171             delayMicroseconds(1); // pulse time
172             PORTB = PORTB ^ selStepStep; // set LOW
173             PORTB = PORTB ^ selStepStep; // set HIGH
174             delayMicroseconds(1); // pulse time
175             PORTB = PORTB ^ selStepStep; // set LOW
176             PORTB = PORTB ^ selStepStep; // set HIGH
177             delayMicroseconds(1); // pulse time
178             PORTB = PORTB ^ selStepStep; // set LOW
179             PORTB = PORTB ^ selStepStep; // set HIGH
180             delayMicroseconds(1); // pulse time
181             PORTB = PORTB ^ selStepStep; // set LOW
182             PORTB = PORTB ^ selStepStep; // set HIGH
183             delayMicroseconds(1); // pulse time
184             PORTB = PORTB ^ selStepStep; // set LOW
185             PORTB = PORTB ^ selStepStep; // set HIGH
186             delayMicroseconds(1); // pulse time
187             PORTB = PORTB ^ selStepStep; // set LOW
188             PORTB = PORTB ^ selStepStep; // set HIGH
189             delayMicroseconds(1); // pulse time
190             PORTB = PORTB ^ selStepStep; // set LOW
191             PORTB = PORTB ^ selStepStep; // set HIGH
192             delayMicroseconds(1); // pulse time
193             PORTB = PORTB ^ selStepStep; // set LOW
194             // one step made
195             steps++;
196             noStep = 0;
197             stepDelay = max(stepDelay--,min_stepDelay); //Acceleration: every 15ms the velocity increases with 1 step/
198         } else noStep++;
199     }
200 }
201
202 void setup() {
203     // Set up the LCD's number of columns and rows:
204     lcd.begin(16, 2);
205
206     // Print a message to the LCD.
207     lcdPrint("WASP_Needle", "");
208
209     // set motor pulse low
210     DDRB = B00001111; // pins 8-13 B-0-0-13-12-11-10-9-8
211
212     // set motor dir high
213     DDRD = B11110000; // pins 1-7 B-7-6-5 -4 -3 -2 -1-0
214
215
216     // Initiate rotary pins of the encoder
217     pinMode (encoderPinA,INPUT);
218     pinMode (encoderPinB,INPUT);
219
220     // Disable steppers on startup
221     pinMode (stepperEnable,OUTPUT);
222     digitalWrite(stepperEnable, HIGH);
223
224     // Initiate interrupt
225     Timer1.initialize(timerInterval); // set a timer with specified interval
226     Timer1.attachInterrupt( interrupt ); // attach the service routine here
227
228
229     delay(1000);
230     lcdPrint("Press_a_button", "to_continue");
231
232     machineState = 2;
233
234 }
235

```

```

236 int Timer2=0;
237 void loop() {
238   if (machineState < 2){
239     if (time >= 6667){
240       time = 0;
241       Timer++;
242       if (Timer >=10){
243         Timer2++;
244         Timer = 0;
245         lcdPrint("Time" + String(Timer2), "Cycle" + String(cycle));
246       }
247     }
248     // Red button
249     if (red.uniquePress()) {
250       if (machineState == 0) machineState = 1;
251       cycle++;
252     }
253
254     // Green button
255     if (green.uniquePress()) {
256       if (machineState == 3) {
257         if (selected == 5) {
258           motorSelect = (motorSelect < 5) ? motorSelect+1 : 1;
259           naaldPos = 0;
260           lcdPrint("Manual_step" + String(motorSelect), String(naaldPos));
261         } else {
262           time = 0;
263           Timer = 0;
264           Timer2 = 0;
265           cycle = 0;
266           machineState = 0;
267           digitalWrite(stepperEnable, LOW);
268         }
269       }
270     }
271
272     // Encoder press
273     if (select.uniquePress()) {
274       // Switch between menu items
275       selected = (selected < 5) ? selected+1:1;
276       if (selected >=4 && machineState < 3) selected = 1;
277       switch (selected) {
278         case 1:
279           lcdPrint("Delay_forward", String(delSelect));
280           break;
281         case 2:
282           lcdPrint("Delay_backward", String(delSelect));
283           break;
284         case 3:
285           lcdPrint("Needle_Offset", String(offSelect));
286           break;
287         case 4:
288           lcdPrint("Sequence", String(seqSelect));
289           break;
290         case 5:
291           naaldPos = 0;
292           lcdPrint("Manual_step" + String(motorSelect), String(naaldPos));
293           break;
294       }
295       delay(200);
296     }
297
298     // Encoder rotate
299     n = (analogRead(encoderPinA) > 1000) ? HIGH : LOW;
300     if ((encoderPinALast == LOW) && (n == HIGH)) {
301       if (analogRead(encoderPinB) < 200) {
302         switch (selected) {
303           case 1:
304             delSelect = max(1, delSelect - 1);
305             lcdPrint("", String(delSelect));
306             break;
307           case 2:
308             delSelect = max(1, delSelect - 1);
309             lcdPrint("", String(delSelect));
310             break;
311           case 3:
312             offSelect = max(1, offSelect - 1);

```

```

315         lcdPrint("",String(offSelect));
316         break;
317     case 4:
318         seqSelect = max(1,seqSelect-1);
319         lcdPrint("",String(seqSelect));
320         break;
321     case 5:
322         digitalWrite(stepperEnable, LOW);
323         stepper(motorSelect, 20,200);
324         machineState = 2;
325         naaldPos=naaldPos-20;
326         lcdPrint("",String(naaldPos));
327         break;
328
329     }
330 } else {
331     switch (selected) {
332     case 1:
333         delSelect = min(3, delSelect+1);
334         lcdPrint("",String(delSelect));
335         break;
336     case 2:
337         delSelect = min(3, delSelect+1);
338         lcdPrint("",String(delSelect));
339         break;
340     case 3:
341         offSelect = min(3, offSelect+1);
342         lcdPrint("",String(offSelect));
343         break;
344     case 4:
345         seqSelect = min(3,seqSelect+1);
346         lcdPrint("",String(seqSelect));
347         break;
348     case 5:
349         digitalWrite(stepperEnable, LOW);
350         stepper(motorSelect, -20,200);
351         machineState = 2;
352         naaldPos=naaldPos+20;
353         lcdPrint("",String(naaldPos));
354         break;
355
356     }
357 }
358 }
359 encoderPinALast = n;
360 }

```


APPENDIX E

MEASUREMENT DETAILS

A. Prototype experiments

TABLE V: Parameter variation

| Parameter: | Sequence (sec) | Offset (off) mm | Substrate (sub) wt% | Velocity (vel) mm/s |
|----------------|----------------|-----------------|---------------------|---------------------|
| | Circular (1) | 3 (1) | 3 (1) | 4 (1) |
| | Diagonal (2) | 10 (2) | 8 (2) | 8 (2) |
| | two by two (3) | 20 (3) | 13 (3) | 13.5 (3) |
| hline Baseline | Circular (1) | 10 (2) | 8 (2) | 4 (1) |

TABLE VI: List of measurements performed.

| Measurement number | Parameter | Measurement number | Parameter |
|--------------------|------------------------|--------------------|------------------------|
| 1 | seq1_OFF1_sub2_vel1_m1 | 26 | seq1_off2_SUB1_vel1_m1 |
| 2 | seq1_OFF1_sub2_vel1_m2 | 27 | seq1_off2_SUB1_vel1_m2 |
| 3 | seq1_OFF1_sub2_vel1_m3 | 28 | seq1_off2_SUB1_vel1_m3 |
| 4 | seq1_OFF1_sub2_vel1_m4 | 29 | seq1_off2_SUB1_vel1_m4 |
| 5 | seq1_OFF1_sub2_vel1_m5 | 30 | seq1_off2_SUB1_vel1_m5 |
| 6 | seq1_OFF2_sub2_vel1_m1 | 31 | seq1_off2_SUB3_vel1_m1 |
| 7 | seq1_OFF2_sub2_vel1_m2 | 32 | seq1_off2_SUB3_vel1_m2 |
| 8 | seq1_OFF2_sub2_vel1_m3 | 33 | seq1_off2_SUB3_vel1_m3 |
| 9 | seq1_OFF2_sub2_vel1_m4 | 34 | seq1_off2_SUB3_vel1_m4 |
| 10 | seq1_OFF2_sub2_vel1_m5 | 35 | seq1_off2_SUB3_vel1_m5 |
| 11 | seq1_OFF3_sub2_vel1_m1 | 36 | seq1_off2_sub2_VEL2_m1 |
| 12 | seq1_OFF3_sub2_vel1_m2 | 37 | seq1_off2_sub2_VEL2_m2 |
| 13 | seq1_OFF3_sub2_vel1_m3 | 38 | seq1_off2_sub2_VEL2_m3 |
| 14 | seq1_OFF3_sub2_vel1_m4 | 39 | seq1_off2_sub2_VEL2_m4 |
| 15 | seq1_OFF3_sub2_vel1_m5 | 40 | seq1_off2_sub2_VEL2_m5 |
| 16 | SEQ2_off2_sub2_vel1_m1 | 41 | seq1_off2_sub2_VEL3_m1 |
| 17 | SEQ2_off2_sub2_vel1_m2 | 42 | seq1_off2_sub2_VEL3_m2 |
| 18 | SEQ2_off2_sub2_vel1_m3 | 43 | seq1_off2_sub2_VEL3_m3 |
| 19 | SEQ2_off2_sub2_vel1_m4 | 44 | seq1_off2_sub2_VEL3_m4 |
| 20 | SEQ2_off2_sub2_vel1_m5 | 45 | seq1_off2_sub2_VEL3_m5 |
| 21 | SEQ3_off2_sub2_vel1_m1 | | |
| 22 | SEQ3_off2_sub2_vel1_m2 | | |
| 23 | SEQ3_off2_sub2_vel1_m3 | | |
| 24 | SEQ3_off2_sub2_vel1_m4 | | |
| 25 | SEQ3_off2_sub2_vel1_m5 | | |

Measurement configuration

3wt% gelatin, tray 1

| | | | | | | | | | |
|--|--|----|----|--|----|--|----|----|--|
| | | 26 | | | 28 | | | 30 | |
| | | | 27 | | | | 29 | | |

8wt% gelatin tray 1

| | | | | | | | | | |
|---|----|----|----|----|----|----|----|--|--|
| 1 | 11 | 16 | 21 | 36 | 41 | 47 | 56 | | |
| 6 | 2 | 17 | 22 | 37 | 46 | 51 | 57 | | |

8wt% gelatin tray 2

| | | | | | | | | | |
|---|---|----|----|----|----|----|----|----|--|
| 3 | 8 | 12 | 18 | 23 | 42 | 48 | 52 | 58 | |
| 7 | 4 | 13 | 19 | 38 | 43 | 49 | 53 | | |

8wt% gelatin tray 3

| | | | | | | | | | |
|---|----|----|----|----|----|----|----|----|--|
| 5 | 10 | 15 | 24 | 39 | 44 | 50 | 55 | 60 | |
| 9 | 14 | 20 | 25 | 40 | 45 | 54 | 59 | | |

13wt% gelatin tray 1

| | | | | | | | | | |
|--|--|----|----|--|----|--|----|----|--|
| | | 31 | | | 33 | | | 35 | |
| | | | 32 | | | | 34 | | |

Fig. 20: Allocation of measurements within the trays Each color represent a type of tray containing a 20 by 2 grid of measurement locations. Measurements are performed tray by tray starting with the 3-wt% tray. Within each tray the measurements are performed in random order.

B. Force measurements

TABLE VII: Measurements performed during the force experiment. Measurements are performed subsequently starting with number one and ending with number 45.

| Measurement number | Parameter |
|--------------------|--------------|
| 1 | sub1_vel1_m1 |
| 4 | sub1_vel1_m2 |
| 7 | sub1_vel1_m3 |
| 10 | sub1_vel1_m4 |
| 13 | sub1_vel1_m5 |
| 2 | sub1_vel2_m1 |
| 5 | sub1_vel2_m2 |
| 8 | sub1_vel2_m3 |
| 11 | sub1_vel2_m4 |
| 14 | sub1_vel2_m5 |
| 3 | sub1_vel3_m1 |
| 6 | sub1_vel3_m2 |
| 9 | sub1_vel3_m3 |
| 12 | sub1_vel3_m4 |
| 15 | sub1_vel3_m5 |
| 16 | sub2_vel1_m1 |
| 19 | sub2_vel1_m2 |
| 22 | sub2_vel1_m3 |
| 25 | sub2_vel1_m4 |
| 28 | sub2_vel1_m5 |
| 17 | sub2_vel2_m1 |
| 20 | sub2_vel2_m2 |
| 23 | sub2_vel2_m3 |
| 26 | sub2_vel2_m4 |
| 29 | sub2_vel2_m5 |
| 18 | sub2_vel3_m1 |
| 21 | sub2_vel3_m2 |
| 24 | sub2_vel3_m3 |
| 27 | sub2_vel3_m4 |
| 30 | sub2_vel3_m5 |
| 31 | sub3_vel1_m1 |
| 34 | sub3_vel1_m2 |
| 37 | sub3_vel1_m3 |
| 40 | sub3_vel1_m4 |
| 43 | sub3_vel1_m5 |
| 32 | sub3_vel2_m1 |
| 35 | sub3_vel2_m2 |
| 38 | sub3_vel2_m3 |
| 41 | sub3_vel2_m4 |
| 44 | sub3_vel2_m5 |
| 33 | sub3_vel3_m1 |
| 36 | sub3_vel3_m2 |
| 39 | sub3_vel3_m3 |
| 42 | sub3_vel3_m4 |
| 45 | sub3_vel3_m5 |

APPENDIX F

M-FILES

A. Prototype experiment

```

1
2 %% load data produced with prototype experiment
3
4 clc,clear,close all
5 % sampletime 20ms,
6 freq = 1/0.02;
7
8 % calibration
9 % 4.84v = 200mm
10 C = 200/4.84; % mm/V
11 u = 1;
12 % Load data and fill datastruct
13 for i = 1:3
14     for j = 1:3
15         for k = 1:3
16             for l = 1:3
17                 for m = 1:5
18                     try
19 seq(i).off(j).sub(k).vel(1).m(m).t = ...
20 xlsread(['seq',num2str(i),'_off',num2str(j),'_sub',num2str(k),'_vel',num2str(l),'_m',num2str(m)'],'A:A');
21 seq(i).off(j).sub(k).vel(1).m(m).s = ...
22 C*xlsread(['seq',num2str(i),'_off',num2str(j),'_sub',num2str(k),'_vel',num2str(l),'_m',num2str(m)'],'B:B');
23 seq(i).off(j).sub(k).vel(1).m(m).filt = smooth(seq(i).off(j).sub(k).vel(1).m(m).s,5);
24 [filt] = seq(i).off(j).sub(k).vel(1).m(m).filt;
25 seq(i).off(j).sub(k).vel(1).m(m).t=seq(i).off(j).sub(k).vel(1).m(m).t/1000;
26 [time] = seq(i).off(j).sub(k).vel(1).m(m).t;
27 n = 1;
28 % first step towards the local minima
29 for o = 30:30:length(filt)-30
30     if filt(o+30)-filt(o) > C*0.01 && filt(o)-filt(o-30)< C*0.01
31         seq(i).off(j).sub(k).vel(1).m(m).low(n,:) = [time(o),filt(o)];
32         seq(i).off(j).sub(k).vel(1).m(m).lowIndex(n) = o;
33         n = n+1;
34     end
35 end
36 [low] = seq(i).off(j).sub(k).vel(1).m(m).low;
37 [index] =seq(i).off(j).sub(k).vel(1).m(m).lowIndex;
38 n = 1;
39 % second step towards the local minima
40 for o = 1:length(low)
41     a = index(o)-round(0.15*mean(gradient(index)));
42     b = index(o)+round(0.15*mean(gradient(index)));
43     [x,y] = min(filt(a:b));
44     c = time(a:b);
45     seq(i).off(j).sub(k).vel(1).m(m).lown(n,:) = [c(y),x];
46
47     n = n+1;
48 end
49 [lown] = seq(i).off(j).sub(k).vel(1).m(m).lown;
50 n = 1;
51 %local maxima
52 for o = 1:length(index)-1
53     c = time(index(o):index(o+1));
54     [x,y] = max(filt(index(o):index(o+1)));
55     seq(i).off(j).sub(k).vel(1).m(m).maxn(n,:) = [c(y),x];
56     n = n + 1;
57 end
58 [maxn] = seq(i).off(j).sub(k).vel(1).m(m).maxn;
59 seq(i).off(j).sub(k).vel(1).m(m).dmaxn = gradient(maxn(:,2));
60 [dmaxn] = seq(i).off(j).sub(k).vel(1).m(m).dmaxn;
61
62
63
64 q = seq(i).off(j).sub(k).vel(1).m(m).low(:,2);
65 seq(i).off(j).sub(k).vel(1).m(m).dlow = gradient(q);
66 [time] = seq(i).off(j).sub(k).vel(1).m(m).t;
67 [diff] = seq(i).off(j).sub(k).vel(1).m(m).dlow;
68 [low] = seq(i).off(j).sub(k).vel(1).m(m).low;
69 [filt] =seq(i).off(j).sub(k).vel(1).m(m).filt;
70 [s] = seq(i).off(j).sub(k).vel(1).m(m).s;
71 [lown] = seq(i).off(j).sub(k).vel(1).m(m).lown;
72 [dlown] = gradient(lown(:,2)); %change of slip over time
73 seq(i).off(j).sub(k).vel(1).m(m).dlown = dlown;
74 % traveled distance

```

```

75 seq(i).off(j).sub(k).vel(1).m(m).distA = mean(filt(length(filt)-10:length(filt)))-mean(filt(1:10));
76 [distA] = seq(i).off(j).sub(k).vel(1).m(m).distA;
77 % Theoretical distance
78 if j == 1;
79 [distT] = length(low)*3;
80
81 else if j == 2;
82 [distT] = length(low)*10;
83     else
84         [distT] = length(low)*20;
85     end
86 end
87 seq(i).off(j).sub(k).vel(1).m(m).distT = distT;
88
89 % Ratio between actual and theoretical
90 eff = distA/distT;
91 seq(i).off(j).sub(k).vel(1).m(m).eff = eff;
92
93 % distance retraction phase
94 n = 1;
95 for o = 2:length(lown)-1
96     seq(i).off(j).sub(k).vel(1).m(m).dret(n) = maxn(o,2)-lown(o,2);
97     n = n + 1;
98 end
99
100
101 % distance protrusion phase
102 n = 1;
103 for o = 2:length(lown)-1
104     seq(i).off(j).sub(k).vel(1).m(m).dprot(n) = maxn(o-1,2)-lown(o,2);
105     n = n + 1;
106 end
107
108 % average Velocity
109 if j == 1 && l == 1
110     vavg = distA/(length(low)*(5*3/4));
111     seq(i).off(j).sub(k).vel(1).m(m).vavg = vavg;
112     else if j == 1 && l == 1
113         vavg = distA/(length(low)*(5*3/10));
114         seq(i).off(j).sub(k).vel(1).m(m).vavg = vavg;
115         else if j == 1 && l == 1
116             vavg = distA/(length(low)*(5*3/13.5));
117             seq(i).off(j).sub(k).vel(1).m(m).vavg = vavg;
118     else if j == 2 && l == 1
119         vavg = distA/(length(low)*(5*10/4));
120         seq(i).off(j).sub(k).vel(1).m(m).vavg = vavg;
121         else if j == 2 && l == 2
122             vavg = distA/(length(low)*(5*10/10));
123             seq(i).off(j).sub(k).vel(1).m(m).vavg = vavg;
124             else if j == 2 && l == 3
125                 vavg = distA/(length(low)*(5*10/13.5));
126                 seq(i).off(j).sub(k).vel(1).m(m).vavg = vavg;
127
128     else if j == 3 && l == 1
129         vavg = distA/(length(low)*(5*20/4));
130         seq(i).off(j).sub(k).vel(1).m(m).vavg = vavg;
131         else if j == 3 && l == 2
132             vavg = distA/(length(low)*(5*20/10));
133             seq(i).off(j).sub(k).vel(1).m(m).vavg = vavg;
134             else if j == 3 && l == 3
135                 vavg = distA/(length(low)*(5*20/13.5));
136                 seq(i).off(j).sub(k).vel(1).m(m).vavg = vavg;
137             end
138         end
139     end
140     end
141     end
142     end
143     end
144     end
145 end
146
147
148 figure('units','normalized','outerposition',[0 0 1 1])
149 hold on
150 plot(time,filt);
151 plot(low(:,1), low(:,2),'+');
152 plot(lown(:,1), lown(:,2),'r');
153 title(['seq',num2str(i),'_off',num2str(j),'_sub',num2str(k),'_vel',num2str(l),'_m',num2str(m)']);

```

```

154 u = u+1;
155                                     end
156                                 end
157                            end
158                        end
159                    end
160                end

1 %% plot data produced with the prototype experiment
2 clc,close all
3 n = 20;
4
5 %% Example signal
6 i = 1; j = 1; k = 2; l = 1; m = 5;
7
8 a1 = seq(i).off(j).sub(k).vel(l).m(m).t;
9 b1 = seq(i).off(j).sub(k).vel(l).m(m).filt;
10 c1 = seq(i).off(j).sub(k).vel(l).m(m).low(:,1);
11 d1 = seq(i).off(j).sub(k).vel(l).m(m).low(:,2);
12 e1 = seq(i).off(j).sub(k).vel(l).m(m).lown(:,1);
13 f1 = seq(i).off(j).sub(k).vel(l).m(m).lown(:,2);
14 g1 = seq(i).off(j).sub(k).vel(l).m(m).maxn(:,1);
15 h1 = seq(i).off(j).sub(k).vel(l).m(m).maxn(:,2);
16
17 i2 = 1; j2 = 2; k2 = 2; l2 = 1; m2 = 5;
18 a2 = seq(i2).off(j2).sub(k2).vel(l2).m(m2).t;
19 b2 = seq(i2).off(j2).sub(k2).vel(l2).m(m2).filt;
20 c2 = seq(i2).off(j2).sub(k2).vel(l2).m(m2).low(:,1);
21 d2 = seq(i2).off(j2).sub(k2).vel(l2).m(m2).low(:,2);
22 e2 = seq(i2).off(j2).sub(k2).vel(l2).m(m2).lown(:,1);
23 f2 = seq(i2).off(j2).sub(k2).vel(l2).m(m2).lown(:,2);
24 g2 = seq(i2).off(j2).sub(k2).vel(l2).m(m2).maxn(:,1);
25 h2 = seq(i2).off(j2).sub(k2).vel(l2).m(m2).maxn(:,2);
26
27 i3 = 1; j3 = 3; k3 = 2; l3 = 1; m3 = 5;
28 a3 = seq(i3).off(j3).sub(k3).vel(l3).m(m3).t;
29 b3 = seq(i3).off(j3).sub(k3).vel(l3).m(m3).filt;
30 c3 = seq(i3).off(j3).sub(k3).vel(l3).m(m3).low(:,1);
31 d3 = seq(i3).off(j3).sub(k3).vel(l3).m(m3).low(:,2);
32 e3 = seq(i3).off(j3).sub(k3).vel(l3).m(m3).lown(:,1);
33 f3 = seq(i3).off(j3).sub(k3).vel(l3).m(m3).lown(:,2);
34 g3 = seq(i3).off(j3).sub(k3).vel(l3).m(m3).maxn(:,1);
35 h3 = seq(i3).off(j3).sub(k3).vel(l3).m(m3).maxn(:,2);
36
37
38 figure(n)
39 n = n + 1;
40 subplot(3,1,1);
41 hold on
42 plot(a1,b1);
43 plot(e1,f1,'r+');
44 plot(g1,h1,'r. ');
45 title(['seq',num2str(i),'_off',num2str(j),'_sub',num2str(k),'_vel',num2str(l),'_m',num2str(m)']);
46 axis([0,300,30,150]);
47 xlabel('Time[s]');
48 ylabel('Traveled distance [mm]');
49 hold off
50
51 subplot(3,1,2);
52 hold on
53 plot(a2,b2);
54 plot(e2,f2,'r+');
55 plot(g2,h2,'r. ');
56 title(['seq',num2str(i2),'_off',num2str(j2),'_sub',num2str(k2),'_vel',num2str(l2),'_m',num2str(m2)']);
57 axis([0,300,30,150]);
58 xlabel('Time[s]');
59 ylabel('Traveled distance [mm]');
60
61 subplot(3,1,3);
62 hold on
63 plot(a3,b3);
64 plot(e3,f3,'r+');
65 plot(g3,h3,'r. ');
66 title(['seq',num2str(i3),'_off',num2str(j3),'_sub',num2str(k3),'_vel',num2str(l3),'_m',num2str(m3)']);
67 xlabel('Time[s]');
68 ylabel('Traveled distance [mm]');
69 axis([0,300,30,150]);
70
71 %% Sequence

```

```

72
73 sequence = ...
74 [(1-seq(1).off(2).sub(2).vel(1).m(1).eff),(1-seq(2).off(2).sub(2).vel(1).m(1).eff);...
75 (1-seq(1).off(2).sub(2).vel(1).m(2).eff),(1-seq(2).off(2).sub(2).vel(1).m(2).eff);...
76 (1-seq(1).off(2).sub(2).vel(1).m(3).eff),(1-seq(2).off(2).sub(2).vel(1).m(3).eff);...
77 (1-seq(1).off(2).sub(2).vel(1).m(4).eff),(1-seq(2).off(2).sub(2).vel(1).m(4).eff);...
78 (1-seq(1).off(2).sub(2).vel(1).m(5).eff),(1-seq(2).off(2).sub(2).vel(1).m(5).eff) ]
79
80 pseq = anova(sequence)
81
82 i = 1; j = 2; k = 2; l = 1; m = 2;
83 i2 = 2; j2 = 2; k2 = 2; l2 = 1; m2 = 2;
84
85 sq1 = [];
86 sq2 = [];
87 sq3 = [];
88 sq4 = [];
89 for m = 1:5
90     m2=m;m3=m;
91
92     sq1 = [sq1,(10-seq(i).off(j).sub(k).vel(1).m(m).dret)/10];
93     sq2 = [sq2,(10-seq(i2).off(j2).sub(k2).vel(l2).m(m2).dret)/10];
94
95     sq3 = [sq3,(seq(i).off(j).sub(k).vel(1).m(m).dprot)/10];
96     sq4 = [sq4,(seq(i2).off(j2).sub(k2).vel(l2).m(m2).dprot)/10];
97
98
99 end
100
101 %% Offset
102
103 offset = ...
104 [(1-seq(1).off(1).sub(2).vel(1).m(1).eff),(1-seq(1).off(2).sub(2).vel(1).m(1).eff),(1-seq(1).off(3).sub(2).vel(1).m(1).eff);...
105 (1-seq(1).off(1).sub(2).vel(1).m(2).eff),(1-seq(1).off(2).sub(2).vel(1).m(2).eff),(1-seq(1).off(3).sub(2).vel(1).m(2).eff);...
106 (1-seq(1).off(1).sub(2).vel(1).m(3).eff),(1-seq(1).off(2).sub(2).vel(1).m(3).eff),(1-seq(1).off(3).sub(2).vel(1).m(3).eff);...
107 (1-seq(1).off(1).sub(2).vel(1).m(4).eff),(1-seq(1).off(2).sub(2).vel(1).m(4).eff),(1-seq(1).off(3).sub(2).vel(1).m(4).eff);...
108 (1-seq(1).off(1).sub(2).vel(1).m(5).eff),(1-seq(1).off(2).sub(2).vel(1).m(5).eff),(1-seq(1).off(3).sub(2).vel(1).m(5).eff) ]
109
110 poffset = anova(offset)
111 [H,P,CI] = ttest2(offset(:,2),offset(:,3))
112
113 i = 1; j = 1; k = 2; l = 1; m = 2;
114 i2 = 1; j2 = 2; k2 = 2; l2 = 1; m2 = 2;
115 i3 = 1; j3 = 3; k3 = 2; l3 = 1; m3 = 2;
116 O1 = [];
117 O2 = [];
118 O3 = [];
119 O4 = [];
120 O5 = [];
121 O6 = [];
122 for m = 1:5
123     m2=m;m3=m;
124
125     O1 = [O1,(3-seq(i).off(j).sub(k).vel(1).m(m).dret)/3];
126     O2 = [O2,(10-seq(i2).off(j2).sub(k2).vel(l2).m(m2).dret)/10];
127     O3 = [O3,(20-seq(i3).off(j3).sub(k3).vel(l3).m(m3).dret)/20];
128
129     O4 = [O4,(seq(i).off(j).sub(k).vel(1).m(m).dprot)/3];
130     O5 = [O5,(seq(i2).off(j2).sub(k2).vel(l2).m(m2).dprot)/10];
131     O6 = [O6,(seq(i3).off(j3).sub(k3).vel(l3).m(m3).dprot)/20];
132
133 end
134 figure(n)
135 n = n + 1;
136 group = [repmat({'3mm'}, length(O1), 1); repmat({'10mm'}, length(O2), 1); repmat({'20mm'}, length(O3), 1)];
137 boxplot ([O1'*3;O2'*10;O3'*20],group)
138 title ('Slip_in_the_retraction_phase')
139 xlabel('Offset')
140 ylabel('Slip_{ret}_{mm}')
141 axis([0.5 3.5 0 4.5])
142
143
144 figure(n)
145 n = n + 1;
146 group = [repmat({'3mm'}, length(O4), 1); repmat({'10mm'}, length(O5), 1); repmat({'20mm'}, length(O6), 1)];
147 boxplot ([O4'*3;O5'*10;O6'*20],group)
148 title ('Slip_in_the_protrusion_phase')
149 xlabel('Offset')
150 ylabel('Slip_{pro}_{mm}')

```

```

151 axis([0.5 3.5 0 4.5])
152
153
154 %% substrate
155
156 substrate = ...
157 [(1-seq(1).off(2).sub(1).vel(1).m(1).eff),(1-seq(1).off(2).sub(2).vel(1).m(1).eff),(1-seq(1).off(2).sub(3).vel(1).m(1).eff);...
158 (1-seq(1).off(2).sub(1).vel(1).m(2).eff),(1-seq(1).off(2).sub(2).vel(1).m(2).eff),(1-seq(1).off(2).sub(3).vel(1).m(2).eff);...
159 (1-seq(1).off(2).sub(1).vel(1).m(3).eff),(1-seq(1).off(2).sub(2).vel(1).m(3).eff),(1-seq(1).off(2).sub(3).vel(1).m(3).eff);...
160 (1-seq(1).off(2).sub(1).vel(1).m(4).eff),(1-seq(1).off(2).sub(2).vel(1).m(4).eff),(1-seq(1).off(2).sub(3).vel(1).m(4).eff);...
161 (1-seq(1).off(2).sub(1).vel(1).m(5).eff),(1-seq(1).off(2).sub(2).vel(1).m(5).eff),(1-seq(1).off(2).sub(3).vel(1).m(5).eff) ]
162
163 psubstrate = anova1(substrate)
164
165 i = 1; j = 2; k = 1; l = 1; m = 2;
166 i2 = 1; j2 = 2; k2 = 2; l2 = 1; m2 = 2;
167 i3 = 1; j3 = 2; k3 = 3; l3 = 1; m3 = 2;
168 ss1 = [];
169 ss2 = [];
170 ss3 = [];
171 ss4 = [];
172 ss5 = [];
173 ss6 = [];
174 for m = 1:5
175     m2=m;m3=m;
176
177     ss1 = [ss1,(10-seq(i).off(j).sub(k).vel(1).m(m).dret)/10];
178     ss2 = [ss2,(10-seq(i2).off(j2).sub(k2).vel(l2).m(m2).dret)/10];
179     ss3 = [ss3, (10-seq(i3).off(j3).sub(k3).vel(l3).m(m3).dret)/10];
180
181     ss4 = [ss4,(seq(i).off(j).sub(k).vel(1).m(m).dprot)/10];
182     ss5 = [ss5,(seq(i2).off(j2).sub(k2).vel(l2).m(m2).dprot)/10];
183     ss6 = [ss6,(seq(i3).off(j3).sub(k3).vel(l3).m(m3).dprot)/10];
184
185
186 end
187
188 %% velocity
189
190 velocity1 = ...
191 [(1-seq(1).off(2).sub(2).vel(1).m(1).eff),(1-seq(1).off(2).sub(2).vel(2).m(1).eff),(1-seq(1).off(2).sub(2).vel(3).m(1).eff);...
192 (1-seq(1).off(2).sub(2).vel(1).m(2).eff),(1-seq(1).off(2).sub(2).vel(2).m(2).eff),(1-seq(1).off(2).sub(2).vel(3).m(2).eff);...
193 (1-seq(1).off(2).sub(2).vel(1).m(3).eff),(1-seq(1).off(2).sub(2).vel(2).m(3).eff),(1-seq(1).off(2).sub(2).vel(3).m(3).eff);...
194 (1-seq(1).off(2).sub(2).vel(1).m(4).eff),(1-seq(1).off(2).sub(2).vel(2).m(4).eff),(1-seq(1).off(2).sub(2).vel(3).m(4).eff);...
195 (1-seq(1).off(2).sub(2).vel(1).m(5).eff),(1-seq(1).off(2).sub(2).vel(2).m(5).eff),(1-seq(1).off(2).sub(2).vel(3).m(5).eff) ]
196
197 velocity2 = ...
198 [seq(1).off(2).sub(2).vel(1).m(1).vavg,seq(1).off(2).sub(2).vel(2).m(1).vavg,seq(1).off(2).sub(2).vel(3).m(1).vavg;...
199 seq(1).off(2).sub(2).vel(1).m(2).vavg,seq(1).off(2).sub(2).vel(2).m(2).vavg,seq(1).off(2).sub(2).vel(3).m(2).vavg;...
200 seq(1).off(2).sub(2).vel(1).m(3).vavg,seq(1).off(2).sub(2).vel(2).m(3).vavg,seq(1).off(2).sub(2).vel(3).m(3).vavg;...
201 seq(1).off(2).sub(2).vel(1).m(4).vavg,seq(1).off(2).sub(2).vel(2).m(4).vavg,seq(1).off(2).sub(2).vel(3).m(4).vavg;...
202 seq(1).off(2).sub(2).vel(1).m(5).vavg,seq(1).off(2).sub(2).vel(2).m(5).vavg,seq(1).off(2).sub(2).vel(3).m(5).vavg ]
203
204 Pvel = anova1(velocity1)
205
206 i = 1; j = 2; k = 2; l = 1; m = 2;
207 i2 = 1; j2 = 2; k2 = 2; l2 = 2; m2 = 2;
208 i3 = 1; j3 = 2; k3 = 2; l3 = 3; m3 = 2;
209 v1 = [];
210 v2 = [];
211 v3 = [];
212 v4 = [];
213 v5 = [];
214 v6 = [];
215 for m = 1:5
216     m2=m;m3=m;
217
218     v1 = [v1,(10-seq(i).off(j).sub(k).vel(1).m(m).dret)/10];
219     v2 = [v2,(10-seq(i2).off(j2).sub(k2).vel(l2).m(m2).dret)/10];
220     v3 = [v3, (10-seq(i3).off(j3).sub(k3).vel(l3).m(m3).dret)/10];
221
222     v4 = [v4,(seq(i).off(j).sub(k).vel(1).m(m).dprot)/10];
223     v5 = [v5,(seq(i2).off(j2).sub(k2).vel(l2).m(m2).dprot)/10];
224     v6 = [v6,(seq(i3).off(j3).sub(k3).vel(l3).m(m3).dprot)/10];
225
226
227 end
228
229 %% group plot

```



```

230 % subplots
231
232 figure(n)
233 n = n + 1;
234 % title('Total slip ratio')
235 group = [repmat({'Circular'}, 5, 1); repmat({'Diagonal'}, 5, 1)];
236 subplot(3,4,1), boxplot(sequence,group)
237 % xlabel('Sequence')
238 ylabel('SR_{tot}-[-]')
239 axis([0,3,0,0.8]);
240 group = [repmat({'4_μm'}, 5, 1); repmat({'10_μm'}, 5, 1); repmat({'20_μm'}, 5, 1)];
241 subplot(3,4,2), boxplot(offset,group);
242 % xlabel('Offset')
243 axis([0,4,0,0.8]);
244 group = [repmat({'3_wt%'}, 5, 1); repmat({'8_wt%'}, 5, 1); repmat({'13_wt%'}, 5, 1)];
245 subplot(3,4,3), boxplot(substrate,group);
246 % xlabel('Substrate')
247 axis([0,4,0,0.8]);
248 group = [repmat({'4_μm/s'}, 5, 1); repmat({'8_μm/s'}, 5, 1); repmat({'13_μm/s'}, 5, 1)];
249 subplot(3,4,4), boxplot(velocity1,group);
250 % xlabel('Velocity')
251 axis([0,4,0,0.8]);
252
253 group = [repmat({'Circular'}, length(sq3), 1); repmat({'Diagonal'}, length(sq4),1)];
254 subplot(3,4,5), boxplot([sq3'; sq4'],group);
255 % xlabel('Sequence')
256 ylabel('SR_{pro}-[-]')
257 % title('Slip ratio in the protrusion phase')
258 axis([0,3,0,0.8]);
259 group = [repmat({'4_μm'}, length(O4), 1); repmat({'10_μm'}, length(O5), 1); ...
260         repmat({'20_μm'}, length(O6), 1)];
261 subplot(3,4,6), boxplot([O4'; O5'; O6'],group);
262 % xlabel('Offset')
263 axis([0,4,0,0.8]);
264 group = [repmat({'3_wt%'}, length(ss4), 1); repmat({'8_wt%'}, length(ss5), 1); ...
265         repmat({'13_wt%'}, length(ss6), 1)];
266 subplot(3,4,7), boxplot([ss4'; ss5'; ss6'],group);
267 % xlabel('Substrate')
268 axis([0,4,0,0.8]);
269 group = [repmat({'4_μm/s'}, length(v4), 1); repmat({'8_μm/s'}, length(v5), 1); ...
270         repmat({'13_μm/s'}, length(v6), 1)];
271 subplot(3,4,8), boxplot([v4'; v5'; v6'],group);
272 % xlabel('Velocity')
273 axis([0,4,0,0.8]);
274
275 group = [repmat({'Circular'}, length(sq1), 1); repmat({'Diagonal'}, length(sq2),1)];
276 subplot(3,4,9), boxplot([sq1'; sq2'],group);
277 xlabel('Sequence')
278 ylabel('SR_{ret}-[-]')
279 % title('Slip ratio in the retraction phase')
280 axis([0,3,0,0.8]);
281 group = [repmat({'4_μm'}, length(O1), 1); repmat({'10_μm'}, length(O2), 1); ...
282         repmat({'20_μm'}, length(O3), 1)];
283 subplot(3,4,10), boxplot([O1'; O2'; O3'],group);
284 xlabel('Offset')
285 axis([0,4,0,0.8]);
286 group = [repmat({'3_wt%'}, length(ss1), 1); repmat({'8_wt%'}, length(ss2), 1); ...
287         repmat({'13_wt%'}, length(ss3), 1)];
288 subplot(3,4,11), boxplot([ss1'; ss2'; ss3'],group);
289 xlabel('Substrate')
290 axis([0,4,0,0.8]);
291 group = [repmat({'4_μm/s'}, length(v1), 1); repmat({'8_μm/s'}, length(v2), 1); ...
292         repmat({'13_μm/s'}, length(v3), 1)];
293 subplot(3,4,12), boxplot([v1'; v2'; v3'],group);
294 xlabel('Velocity')
295 axis([0,4,0,0.8]);
296
297 %% Individual anova's (decoupling into protrusion and retraction phase)
298 group1 = ss4; % or ss1, ss4, sq1, sq4, O1, O4, v1, v4
299 group2 = ss5; % or ss2, ss5, sq2, sq5, O2, O5, v2, v5
300 group3 = ss6; % or ss3, ss6, sq3, sq6, O3, O6, v3, v6
301 name = [repmat({'1'}, length(group1'), 1); repmat({'2'}, length(group2'), 1); repmat({'3'}, ...
302         length(group3'), 1)];
303
304 groups = [group1, group2, group3];
305
306 [p,anovatab,stats] = anoval(groups,name);

```

B. Force experiment

```

1 %% Load data produced with force experiment
2 clc,clear,close all
3
4 %% Calibrate force sensor
5 c = [];
6 d = [0;0.250;0.500;0.750;1];
7 g = 9.81;
8 F = g*d;
9 for i = 1:5
10 a = load(['calib00',num2str(i)]);
11 b = ['calib00',num2str(i)];
12 c(i) = mean(a.(b).Y(4).Data);
13 end
14 plot(F,c,'+')
15 title('Force_sensor_assembly_calibration')
16 xlabel('Balance_weight_[Kg]')
17 ylabel('Read_out_[V]')
18 [calib,S] = polyfit(c',F,1);
19 calib = calib(1) %N/V
20 y = 1;
21
22 %% load data
23 for i = 1:3
24     for j = 1:3
25         for k = 1:12
26
27             try
28                 if k <=9
29 a = load(['sub',num2str(i),'_vel',num2str(j),'_m00',num2str(k)]);
30 b = ['sub',num2str(i),'_vel',num2str(j),'_m00',num2str(k)];
31 else
32 a = load(['sub',num2str(i),'_vel',num2str(j),'_m0',num2str(k)]);
33 b = ['sub',num2str(i),'_vel',num2str(j),'_m0',num2str(k)];
34 end
35 sub(i).vel(j).m(y).t = a.(b).X.Data;
36 sub(i).vel(j).m(y).F = calib*a.(b).Y(4).Data;
37 sub(i).vel(j).m(y).p = a.(b).Y(8).Data;
38
39 %data manipulation
40 % Filter force data and correct filtered data for force bias
41 sub(i).vel(j).m(y).Ff = smooth(sub(i).vel(j).m(y).F,100);
42 sub(i).vel(j).m(y).Ff = sub(i).vel(j).m(y).Ff-mean(sub(i).vel(j).m(y).Ff(1:500));
43 % Retrieve maximum insertion force and index
44 [temp1,temp2] = min(sub(i).vel(j).m(y).Ff);
45 sub(i).vel(j).m(y).Fmin = [temp1,temp2];
46 % Retrieve maximum retraction force and index
47 [temp1,temp2] = max(sub(i).vel(j).m(y).Ff);
48 sub(i).vel(j).m(y).Fmax = [temp1,temp2];
49 % Retrieve point of needle exit
50 for m = temp2:length(sub(i).vel(j).m(y).p)-1
51     if sub(i).vel(j).m(y).p(m) - 1 <= sub(i).vel(j).m(y).p(1)
52         sub(i).vel(j).m(y).matOut = m;
53         break;
54     end
55 end
56 smin = sub(i).vel(j).m(y).Fmin(2);
57 smax = sub(i).vel(j).m(y).Fmax(2);
58 temp = sub(i).vel(j).m(y).matOut;
59 t = sub(i).vel(j).m(y).t(1:temp-smax+1);
60 sub(i).vel(j).m(y).tf = t;
61 sub(i).vel(j).m(y).Fins = sub(i).vel(j).m(y).Ff(smin-(temp-smax):smin)*(-1);
62 sub(i).vel(j).m(y).Fwit = flipud(sub(i).vel(j).m(y).Ff(smax:temp)*(-1));
63 sub(i).vel(j).m(y).depth = flipud((sub(i).vel(j).m(y).p(smax:temp)-sub(i).vel(j).m(y).p(1))'));
64 sub(i).vel(j).m(y).Fcut = sub(i).vel(j).m(y).Fins+sub(i).vel(j).m(y).Fwit;
65 sub(i).vel(j).m(y).FcutAvg = mean(sub(i).vel(j).m(y).Fcut);
66
67 % Plot all measurements
68 figure(1)
69 hold on
70 plot(sub(i).vel(j).m(y).t, sub(i).vel(j).m(y).Ff, 'k')
71 title(['Force_signal_of_all_measurements'])
72 xlabel('Time_[s]')
73 ylabel('Force_[N]')
74 y = y + 1;
75 end
76
77 end

```

```

78         y = 1;
79     end
80 end

1  %% Plot data produced with force experiment
2  close all, clc
3  V = [3;8;13.5];
4  S = [3;8;13];
5  n = 1;
6  %% Used for Methods part. (example signal etc.)
7  for i = 2
8      for j = 2
9          for k = 2
10             t = sub(i).vel(j).m(k).t;
11             tf = sub(i).vel(j).m(k).tf;
12             Fins = sub(i).vel(j).m(k).Fins;
13             Fwit = sub(i).vel(j).m(k).Fwit;
14             Fcut = sub(i).vel(j).m(k).Fcut;
15             Ff = sub(i).vel(j).m(k).Ff;
16             F = sub(i).vel(j).m(k).F;
17             Fmax = sub(i).vel(j).m(k).Fmax;
18             Fmin = sub(i).vel(j).m(k).Fmin;
19             Matout = sub(i).vel(j).m(k).matOut;
20             Depth = flipud(sub(i).vel(j).m(k).p(Fmax(2):Matout))-sub(i).vel(j).m(k).p(Matout));
21             FcFw = Fcut./((-1)*Fwit);
22
23 % plot example signal and resulting force plot
24 figure(n)
25 n = n + 1;
26 hold on
27 plot(sub(i).vel(j).m(k).t,F,'b')
28 plot(sub(i).vel(j).m(k).t,Ff,'r')
29 plot(Fmax(2)/1000,Fmax(1),'+k')
30 plot(Fmin(2)/1000,Fmin(1),'ok')
31 plot(Matout/1000,(Ff(Matout)),'^k')
32
33 title(['Force-signal-of-sub',num2str(i),'_vel',num2str(j),'_m',num2str(k)])
34 xlabel('Time[s]')
35 ylabel('Force[N]')
36 legend('Raw','Filtered','F_{f,max}','F_{i,max}','Substrate_exit')
37
38 figure(n)
39 n = n + 1;
40 hold on
41 plot(Depth,Fins,'b')
42 plot(Depth,Fwit,'k')
43 plot(Depth,Fcut,'r')
44
45 title(['Insertion-and-retraction-aligning-of-sub',num2str(i),'_vel',num2str(j),'_m',num2str(k)])
46 xlabel('Depth[mm]')
47 ylabel('Force[N]')
48 legend('F_{i}','F_{f}','F_{c}')
49
50     end
51 end
52 end
53
54 %% Results
55
56 Mret1 = [];
57 Mins1 = [];
58 cut1 = [];
59 for j = 1:3
60     for k = 1:5
61
62 [Mret1]= [Mret1; sub(1).vel(j).m(k).Fmax(1)];
63 [Mins1] = [Mins1; (-1)*sub(1).vel(j).m(k).Fmin(1)];
64 [cut1] = [cut1; sub(1).vel(j).m(k).FcutAvg];
65     end
66 end
67
68 Mret2 = [];
69 Mins2 = [];
70 cut2 = [];
71 for j = 1:3
72     for k = 1:5
73
74 [Mret2]= [Mret2; sub(2).vel(j).m(k).Fmax(1)];
75 [Mins2] = [Mins2; (-1)*sub(2).vel(j).m(k).Fmin(1)];

```

```

76 [cut2] = [cut2; sub(2).vel(j).m(k).FcutAvg];
77     end
78 end
79
80 Mret3 = [];
81 Mins3 = [];
82 cut3 = [];
83 for j = 1:3
84     for k = 1:5
85
86 [Mret3]= [Mret3; sub(3).vel(j).m(k).Fmax(1)];
87 [Mins3] = [Mins3; (-1)*sub(3).vel(j).m(k).Fmin(1)];
88 [cut3] = [cut3; sub(3).vel(j).m(k).FcutAvg];
89     end
90 end
91
92
93 figure(n)
94 n = n + 1;
95
96 group = [repmat({'4_mm/s_'}, 5, 1); repmat({'8_mm/s_'}, 5, 1); repmat({'13.5_mm/s_'}, 5, 1)];
97 subplot(2,3,1), boxplot([Mret1(1:5), Mret1(6:10), Mret1(11:15)], group);
98 ylabel('F_{f,max}-[N]')
99 axis([0,4,0,12]);
100
101 group = [repmat({'4_mm/s_'}, 5, 1); repmat({'8_mm/s_'}, 5, 1); repmat({'13.5_mm/s_'}, 5, 1)];
102 subplot(2,3,2), boxplot([Mret2(1:5), Mret2(6:10), Mret2(11:15)], group);
103 axis([0,4,0,12]);
104
105 group = [repmat({'4_mm/s_'}, 5, 1); repmat({'8_mm/s_'}, 5, 1); repmat({'13.5_mm/s_'}, 5, 1)];
106 subplot(2,3,3), boxplot([Mret3(1:5), Mret3(6:10), Mret3(11:15)], group);
107 axis([0,4,0,12]);
108
109 group = [repmat({'4_mm/s_'}, 5, 1); repmat({'8_mm/s_'}, 5, 1); repmat({'13.5_mm/s_'}, 5, 1)];
110 subplot(2,3,4), boxplot([cut1(1:5), cut1(6:10), cut1(11:15)], group);
111 ylabel('F_{c}-[N]')
112 axis([0,4,0,6]);
113 xlabel('3_wt%')
114
115 group = [repmat({'4_mm/s_'}, 5, 1); repmat({'8_mm/s_'}, 5, 1); repmat({'13.5_mm/s_'}, 5, 1)];
116 subplot(2,3,5), boxplot([cut2(1:5), cut2(6:10), cut2(11:15)], group);
117 axis([0,4,0,6]);
118 xlabel('8_wt%')
119
120 group = [repmat({'4_mm/s_'}, 5, 1); repmat({'8_mm/s_'}, 5, 1); repmat({'13.5_mm/s_'}, 5, 1)];
121 subplot(2,3,6), boxplot([cut3(1:5), cut3(6:10), cut3(11:15)], group);
122 axis([0,4,0,6]);
123 xlabel('13_wt%')
124
125 %% Anova for friction and cutting force
126 %{
127 anova1([Mret1(1:5), Mret1(6:10), Mret1(11:15)])
128 anova1([Mret2(1:5), Mret2(6:10), Mret2(11:15)])
129 anova1([Mret3(1:5), Mret3(6:10), Mret3(11:15)])
130
131 anova1([cut1(1:5), cut1(6:10), cut1(11:15)])
132 anova1([cut2(1:5), cut2(6:10), cut2(11:15)])
133 anova1([cut3(1:5), cut3(6:10), cut3(11:15)])
134 %}
135
136 %% Depth at which fc and ff are in equilibrium.
137 for i = 1:3
138     for j = 1:3
139         if j == 1
140             u = 48000;
141         else if j == 2
142             u = 18000;
143         else
144             u = 10000;
145         end
146     end
147
148 Fc1 = sub(i).vel(j).m(1).Fcut; Fc2 = sub(i).vel(j).m(2).Fcut; Fc3 = sub(i).vel(j).m(3).Fcut; ...
149     Fc4 = sub(i).vel(j).m(4).Fcut; Fc5 = sub(i).vel(j).m(5).Fcut;
150 Ff1 = sub(i).vel(j).m(1).Fwit; Ff2 = sub(i).vel(j).m(2).Fwit; Ff3 = sub(i).vel(j).m(3).Fwit; ...
151     Ff4 = sub(i).vel(j).m(4).Fwit; Ff5 = sub(i).vel(j).m(5).Fwit;
152 de1 = sub(i).vel(j).m(1).depth; de2 = sub(i).vel(j).m(2).depth; de3 = sub(i).vel(j).m(3).depth; ...
153     de4 = sub(i).vel(j).m(4).depth; de5 = sub(i).vel(j).m(5).depth;
154
155 subs(i).velo(j).cut = (Fc1(length(Fc1)-u:length(Fc1)) +Fc2(length(Fc2)-u:length(Fc2)) ...

```

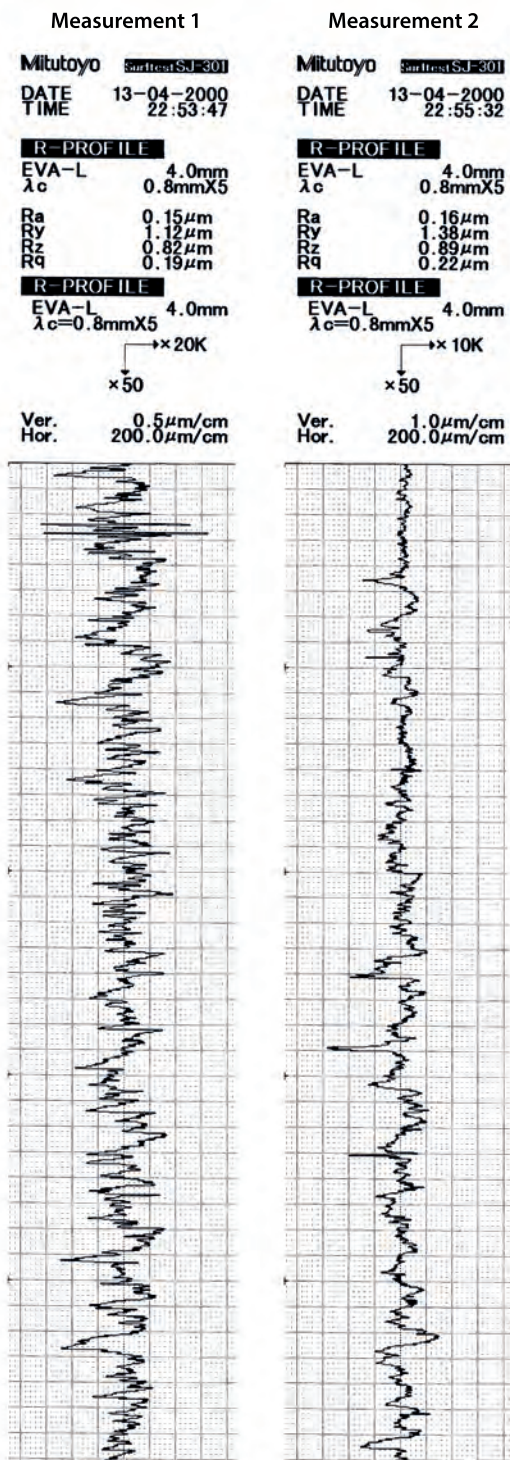
```

155 +Fc3(length(Fc3)-u:length(Fc3)) +Fc4(length(Fc4)-u:length(Fc4)) +Fc5(length(Fc5)-u:length(Fc5))/5;
156 % right side of equation 1
157 subs(i).velo(j).wit = -0.5*((Ff1(length(Ff1)-u:length(Ff1)) +Ff2(length(Ff2)-u:length(Ff2)) ...
158 +Ff3(length(Ff3)-u:length(Ff3)) +Ff4(length(Ff4)-u:length(Ff4)) +Ff5(length(Ff5)-u:length(Ff5))/5);
159 % corresponding needle depth
160 subs(i).velo(j).depth = (de1(length(de1)-u:length(de1)) +de2(length(de2)-u:length(de2)) ...
161 +de3(length(de3)-u:length(de3)) +de4(length(de4)-u:length(de4)) +de5(length(de5)-u:length(de5))/5;
162 % left side of equation 1
163 subs(i).velo(j).cutmean = 0.25*mean(subs(i).velo(j).cut);
164
165 % depth of equilibrium according to equation 1
166 subs(i).velo(j).p = polyfit(subs(i).velo(j).depth,subs(i).velo(j).wit,1);
167 testx = [1:160];
168 testy = testx*subs(i).velo(j).p(1)+subs(i).velo(j).p(2);
169 doEq = (subs(i).velo(j).cutmean - subs(i).velo(j).p(2))/subs(i).velo(j).p(1)
170 subs(i).velo(j).doEq = doEq;
171 figure(n)
172 hold on
173 plot(testx,testy,'r')
174 plot(subs(i).velo(j).depth,subs(i).velo(j).cut)
175 plot(subs(i).velo(j).depth,subs(i).velo(j).wit)
176 n = n + 1;
177 end
178 end
179
180
181 %% model verification
182
183 lowcon1 = sub(1).vel(3).m(6).Fwit;
184 lowcon2 = sub(1).vel(3).m(10).Fwit;
185 midcon1 = sub(2).vel(3).m(6).Fwit;
186 midcon2 = sub(2).vel(3).m(10).Fwit;
187 hicon1 = sub(3).vel(3).m(6).Fwit;
188 hicon2 = sub(3).vel(3).m(10).Fwit;
189 diffflow = (lowcon2(2000:10000)-lowcon1(2000:10000))./lowcon1(2000:10000)*100;
190 diffmid = (midcon2(2000:10000)-midcon1(2000:10000))./midcon1(2000:10000)*100;
191 diffhi = (hicon2(2000:10000)-hicon1(2000:10000))./hicon1(2000:10000)*100;
192
193 Mret1 = [];
194 Mret2 = [];
195 Mret3 = [];
196 for i = 1:3
197     for k = 1:10
198         if i == 1
199             [Mret1]= [Mret1; sub(i).vel(3).m(k).Fmax(1)];
200         else if i ==2
201             [Mret2]= [Mret2; sub(i).vel(3).m(k).Fmax(1)];
202         else [Mret3]= [Mret3; sub(i).vel(3).m(k).Fmax(1)];
203         end
204     end
205 end
206
207 end
208 Mret1 = Mret1/mean(Mret1(1:5));
209 Mret2 = Mret2/mean(Mret2(1:5));
210 Mret3 = Mret3/mean(Mret3(1:5));
211
212 figure(n)
213 n = n + 1;
214 group = [repmat({'3wt%_dh'}, 5, 1); repmat({'3wt%_sh'}, 5, 1); repmat({'8wt%_dh'}, 5, 1); ...
215 repmat({'8wt%_sh'}, 5, 1); repmat({'13wt%_dh'}, 5, 1); repmat({'13wt%_sh'}, 5, 1)];
216 boxplot ([Mret1(1:5),Mret1(6:10),Mret2(1:5),Mret2(6:10),Mret3(1:5),Mret3(6:10)],group)
217 title ('Effect of multiple drillings in the same hole')
218 xlabel('Gelatin concentration and hole type')
219 ylabel('Force [N]')

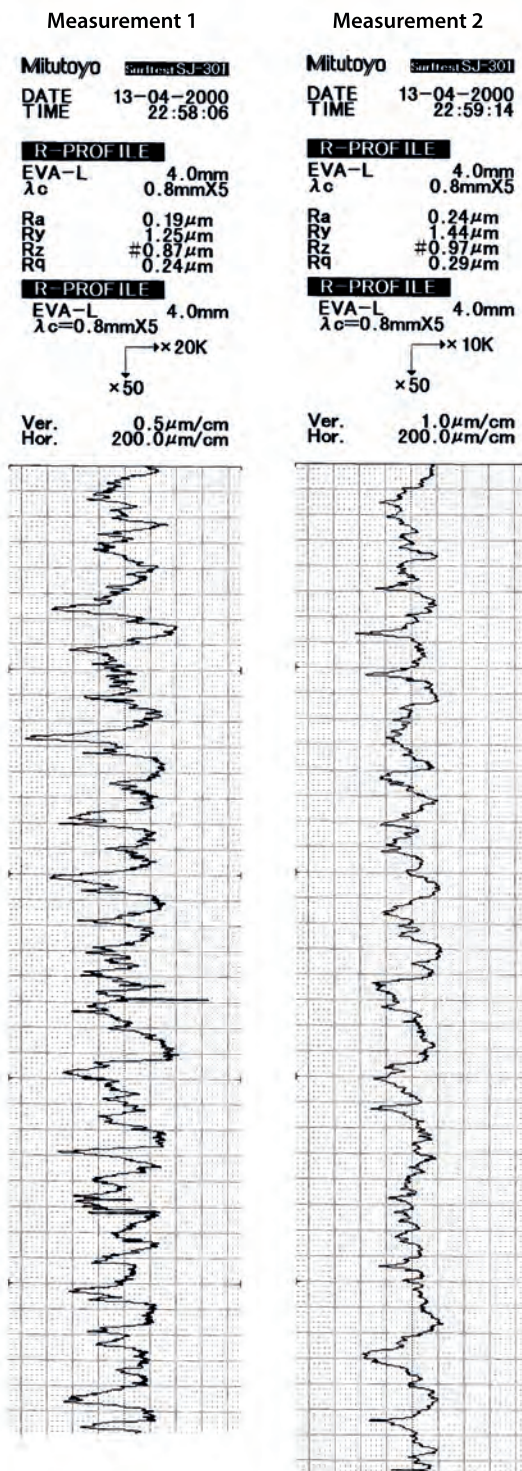
```


APPENDIX G NEEDLE SURFACE ROUGHNESS

Wire EDM surface



Rolled surface



APPENDIX H

FORCE MEASUREMENT CALIBRATION

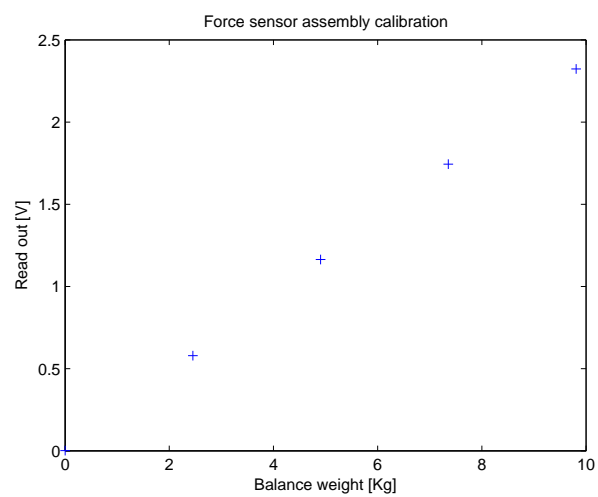


Fig. 21: Calibration of the decoupler assembly containing the Futek-LSB200-5Lb force transducer